UNIVERSITÀ
DEGLI STUDI
DI PADOVA

Sede Amministrativa: Università degli Studi di Padova
Dipartimento di Scienze Chimiche

SCUOLA DI DOTTORATO DI RICERCA IN SCIENZE MOLECOLARI
INDIRIZZO: SCIENZE CHIMICHE
CICLO XXVIII

TUNABLE NANOSYSTEMS FOR SENSING AND CATALYSIS

Direttore della Scuola: Ch.mo Prof. Antonino Polimeno
Coordinatore d’indirizzo: Ch.mo Prof. Antonino Polimeno
Supervisore: Ch.mo Prof. Leonard Prins

Dottorando: Simona Neri

Table of contents

CHAPTER 1: GENERAL INTRODUCTION 1

1.1. HYBRID ORGANIC INORGANIC NANOSYSTEMS 1

1.2. MONOLAYER PROTECTED GOLD NANOPARTICLES 9

1.2.1. Sensing 10

1.2.2. Catalysis 14

1.2.3. Systems Modulation 17

1.3. CONCEPT OF THE THESIS 22

1.4. BIBLIOGRAPHY 23

CHAPTER 2: SELF-ASSEMBLED NANOSYSTEMS FOR ENANTIOSELECTIVE CATALYSIS 29

2.1. INTRODUCTION 29

2.2. CONCEPT 34

2.3. RESULTS AND DISCUSSION 36

2.3.1. Ligand design 36

2.3.2. Synthesis of the catalytic systems 37

2.3.3. Quantification of 4-methyl-2,2’bipyridine-alkylthiols in mixed monolayers 41

2.3.4. Reaction under investigation 44

2.3.5. Catalysis 45

2.3.5.1. Influence of the monolayer on the activity and selectivity of the catalyst 45

2.3.5.2. Enantioselective catalysis 48

2.4. CONCLUSION 53

2.5. EXPERIMENTAL SECTION 54

2.5.1. Instrumentation 54

2.5.2. Materials 55

2.5.3. Synthesis of compounds 5a, 5b and 5c 56

2.5.4. Synthesis of 8-trimethylammonium octanethiol (Thiol 1) 58

2.5.5. Synthesis of Au NP I 59

2.5.6. Determination of the AuNPs I concentration 61

2.5.7. Synthesis of Au NP III and Au NP IV 62

2.5.8. Determination of the concentration of bipyridine head groups on Au NP III and Au NP IV 66

2.5.9. Synthesis of compound 10 68

2.5.10. 2-acetyl-1-methylimidazole 68

2.5.11. 2-Cinnamoyl-1-methyl-1H-imidazole 10 69

2.5.12. General procedure for the Cu^{2+}-catalyzed Diels Alder cycloaddition 69

2.5.13. Synthesis of BP1 70

2.6. BIBLIOGRAPHY 72

CHAPTER 3: ORTHOGONAL SENSING OF SMALL MOLECULES USING A MODULAR NANOPARTICLES-BASED ASSAY 75

3.1. INTRODUCTION 75

3.2. RESULTS AND DISCUSSION 82

3.2.1. Determination of the surface saturation concentration 82

3.2.2. Displacement experiments 83

3.2.3. Selectivity studies 85

3.2.4. Screening in biological medium 90

3.2.5. Modularity 92

3.2.6. Signal amplification 97

3.3. CONCLUSIONS 102

3.4. EXPERIMENTAL SECTION 103

3.4.1. Materials and methods 103

3.4.2. Surface saturation concentration (SSC) 104

3.4.3. Displacement experiments 104

3.4.4. Selectivity studies in buffered solution 105

3.4.5. Selectivity studies in Surine ® 106

3.4.6. Response curves 106

3.4.7. Assay with multiple receptors 107

3.4.8. Catalytic signal amplification 108

3.4.8.1. Inhibition studies 108

3.4.8.2. Sensing trough signal amplification 108

3.5. BIBLIOGRAPHY 109

CHAPTER 4: LIGHT INDUCED MODULATION OF THE CHEMICAL FUNCTIONS OF Au NP 111

4.1. INTRODUCTION 111

4.1.1. Azobenzenes as modules to regulate catalysis by light 114

4.1.2. Azobenzenes as switchable surface ligands 116

4.2. RESULTS AND DISCUSSION 118

4.2.1. Modulation of surface binding induced by light 118

4.2.2. Identification of a fluorescent probe for light-induced displacement.. 119

4.2.3. Displacement experiments 121

4.2.4. Isomerization properties of 1 on AuNP surface 124

.... 127

4.2.5. Cycles 127

4.2.6. Catalysis 131

4.3. CONCLUSIONS 135

4.4. EXPERIMENTAL SECTION 136

4.4.1. Materials and methods 136

4.4.2. Screening of the fluorescent probe 137

4.4.3. Surface saturation concentration 137

4.4.4. Displacement experiments 137

4.4.5. Quantification of the amount of displace probe........................... 138

4.4.6. Cycles monitored by fluorescence 139

4.4.6.1. Cyclization in the same cuvette... 139

4.4.6.2. Cyclization in different cuvettes... 141

4.4.7. UV titrations 142

4.4.8. Catalysis 142

4.4.9. ON/OFF catalysis induced by light.. 143

4.5. BIBLIOGRAPHY 145

ABSTRACT 147

RIASSUNTO 149

CHAPTER 1: GENERAL INTRODUCTION

1.1. HYBRID ORGANIC INORGANIC NANOSYSTEMS

Over the course of evolution Nature has produced materials with remarkable properties and features. Nature is, indeed, a school for many areas of science such as chemistry, biology, physics or engineering. One of Nature's remarkable features is its ability to combine at the nanoscale hybrid (bio)organic and inorganic components for the construction of smart natural materials with a wide variety of functional properties (mechanics, density, permeability, colour, hydrophobia, etc). A high degree of sophistication is the rule and the various components of a structure are assembled following a clearly defined pattern. Such a high level of integration associates several aspects: miniaturisation in order to accommodate a maximum of elementary functions in a small volume, a hybridisation between inorganic and organic components in order to optimize complementary functions and hierarchy.[1]

From the chemical point of view, these hybrids can be either homogeneous systems derived from monomers of miscible organic and inorganic components, or heterogeneous systems (nanocomposites) where at least one of the components' domains has a dimension in the range of nanometers. The so-called hybrid organic–inorganic materials are not simply physical mixtures.[2] Indeed, the properties of these materials are not only the sum of the individual contributions of their phases, but both the inner interfaces and the organic functionalities create additive functions not available in the single phases. Recently two mayor research areas have transformed our vision of chemistry as well as material science: supramolecular chemistry[3,4] and nanotechnology.[5,6]

Supramolecular chemistry is concerned with the study of the non-covalent interactions between molecules, such as hydrogen bonding and metal-ligand coordination, as well as Π-Π stacking, hydrophobic, ionic, and van der Waals forces. Originally it regarded the interaction between a host and a guest molecule, but now, modern supramolecular chemistry has gone beyond such simple systems and encompasses also molecular devices and machines, so called self-processes such as self-assembly and self-organization and includes also complex matter and nanochemistry.[4] The key feature of supramolecular chemistry regards the implementation of molecular information and recognition as a means of controlling the evolution of supramolecular species from their components. It involves the design of systems capable of spontaneously generating well-defined supramolecular entities by self-assembly from their components in a given set of conditions. In particular, the process of self-assembly is defined as a process in which components, either separate or linked, spontaneously form ordered aggregates.[7] In molecular self-assembly, the molecular structure of the components determines the structure of the assembly and the generated "supramolecules" generated are usually in equilibrium states (or at least in kinetically metastable states).[4] A key prerequisite of these starting molecules is the possibility to form multiple non-covalent interactions in a given solvent. Probably, one of the most widespread class of building blocks used are amphiphilic molecules that can assemble into a variety of nanosized structures such as micelles, liposomes, bilayer, and gels.[8,9] An alternative route to generate organized systems is to use pre-organized inorganic nanostructures as template and attach, arrange, or assemble functional molecules of different complexity on the inner or outer surface of the inorganic scaffold.

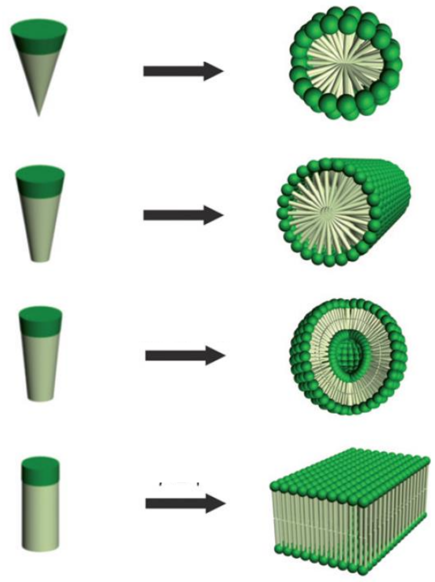

Figure 1.1. Nanostructure morphologies formed by amphiphilic molecules. The shapes depend on the relative volume fraction of hydrophobic and hydrophilic blocks.

Self-assembly plays a key role in nanoscience and nanotechnology.[5,6] Indeed, it has emerged as *the* strategy in chemical synthesis to generate non-biological structures with dimensions between 1 and 100 nanometer.[10,11] By operating in the nanoscale realm, at the very scale of biomolecules, nanotechnology offers a wide range of tools and applications thanks to their unique characteristics.

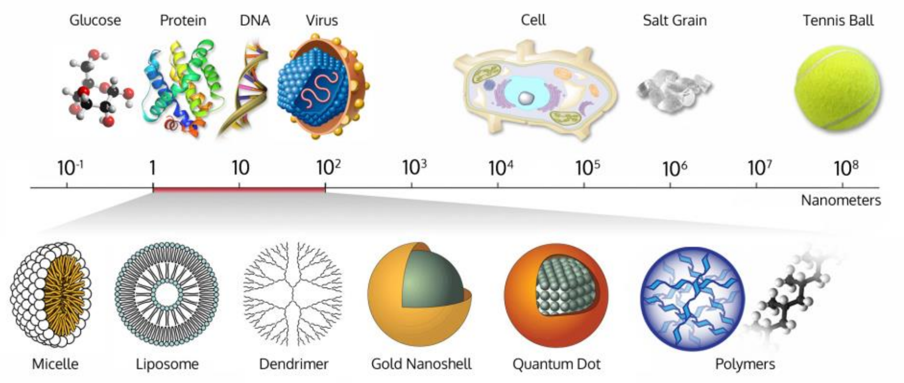

Figure 1.2. Objects of different dimensions in nanometre scale.[12]

Nanoscale objects are at the focus of much attention not only as critical components in the emergence of cellular life, but also as small-scale materials with advanced functions and properties that can be isolated or assimilated into numerous applications, such as in bioelectronics, sensing, drug delivery, catalysis and nanocomposites.[13,14,15]

From a supramolecular chemistry view point, however, the functionalization of nanostructured solids with specific groups to enhance active functions, such as the recognition of guests or to switch surface properties, is particularly interesting. The prospect of building increasingly complex (super)structures using noncovalent chemistry depends, amongst others, on our fundamental understanding of the concept of multivalency.

Multivalency is defined as the operation of multiple molecular recognition events of the same kind occurring simultaneously between two entities (molecules, molecular aggregates, viruses, cells, surfaces).[16] Functional two-dimensional hybrid inorganic-organic systems are based on the attachment of a larger number of a single or several different chemical units on the surface of nanoparticles or nanostructured solids. Traditionally, the functionalization of surfaces was used to modulate adhesion characteristics or to improve the dispersion of particles in liquids but has now turned out to provide also access to multivalent accessible surfaces that can amplify certain functional chemical processes. The amplification processes can be principally divided into two classes. One class commonly shows an enhancement of classical recognition features as a consequence of entropic factors associated with the restriction of movement and the proximity of molecular entities on the surface. The second class, often more advanced, does not necessarily recognize a guest much better, but usually provides an amplified output signal that arises from collective phenomena between the pre-organized functional units. The step from a one-dimensional molecule to a two-dimensional arrangement leads to unique properties which are not simply an extrapolation of the solution conduct to the surface and that can be related to multivalency.[17] In particular multi- and polyvalent interactions play a decisive role in biological systems for recognition adhesion, signal processes and catalysis.[18]

Nature has, through billions of years of evolution, assembled a multitude of polymeric macromolecules capable of exquisite molecular recognition. This functionality arises from the precise control exerted over their biosynthesis that results in key residues being anchored in the appropriate positions to interact with target substrates. Multivalency can drastically increase the significance of 'weak' intermolecular forces, such as hydrogen bonding, π-π interactions and electrostatic interactions, in a manner analogous to how Velcro works. The onset of cooperative or collective processes is one of the most intriguing and peculiar aspects related to self-assembled systems and, in particular, nanoparticles as template for the creation of self-assembled recognition modules. These features arise from the relatively high degree of organization of the surface components in an extended and not dynamic network. An example that underlies the principle of recognition enhancement through preorganization by a self-assembled monolayer (SAM) is reported by Zhu *et al.*[19] Dicarboxylates are known to bind metal cations stronger than can monocarboxylates because the second chelating site operates initially in a unimolecular reaction. A dense, two-dimensional array of ligands on the surface leads to an even higher statistical probability of the complexation of Cu^{2+} ions.

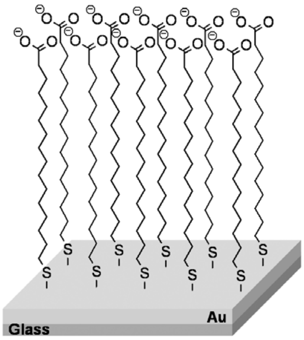

Figure 1.3. SAM of 15-mercaptohexadecanoate on gold.

This effect is manifested in binding constants that are more than two orders of magnitude higher for the hybrid material than the corresponding free carboxylate ligands. The authors interpret the results in terms of a statistical advantage of the multidentate coordination environment that arises from the preorganized ligands on the surface (surface chelate effect).

The second characteristic amplified by self-assembled systems is related to signal generating mechanisms after the molecular recognition which also finds its origin in the multivalent nature of supramolecular entities due to the preorganization of the reporter units. Signaling of the presence of targets can be accomplished in a number of ways, but is commonly based on a change in color, fluorescence, or a redox potential. In general the signaling process usually comprises two steps: 1) selective coordination of the guest by a binding site and 2) transduction of that event by modulation of a photophysical or electro-chemical process within the probe. One of the key tasks in this field is to seek out new and effective systems able to recognize selectively and with high sensitivity, for example, thanks to signal amplification. For a hybrid system consisting of an inorganic nanoparticle and one or more organic functional groups at the surface, this signal amplification can principally contain a contribution from the support material (for example, the plasmon band of Au NP) as well as a contribution from the attached units (for example a cromophore). Figure 4 reports on an example of control on the nature and the efficiency of collective photophysical processes in a network composed of two different fluorescent units organized on the surface of silica nanoparticles.[20] Such a structure is obtained by covering nanoparticles with a layer of dansyl moieties (Dns) and by partially protonating them in solution. The two fluorophores Dns and DnsH$^+$ have very different photophysical properties and can be selectively excited and detected. Photophysical studies indicated that protonation has a dramatic effect on the fluorescence of the nanoparticles, leading to the quenching of both the protonated units and the surrounding non-protonated ones. This amplified response to protonation originates from charge-transfer interactions. This example proves the large signal amplification that can be achieved even upon small chemical inputs.

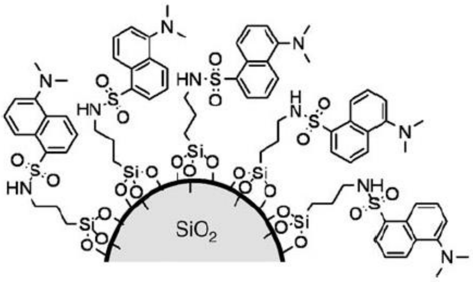

Figure 1.4. Silica nanoparticles functionalized with dansyl groups.

Moreover, the possibility to create mixed self-assembled systems by combining different organic units can be also exploited in terms of cooperativity. Tecilla and co-workers proposed a fluorescent sensor for Cu^{2+} ions based on silica nanoparticles functionalized on the surface with trialkoxysilane derivatives of picolinamide as the ligand and dansylamide as the fluorescent dye. The picolinamide ligand complexed the Cu^{2+} ions with high affinity causing a substantial quenching of the dansyl emission in DMSO. Grafting of the ligand and the dye subunits to the nanoparticles surface not only ensured the intercomponent communication in the sensor, but also induces cooperative processes in the binding of the substrate.[21]

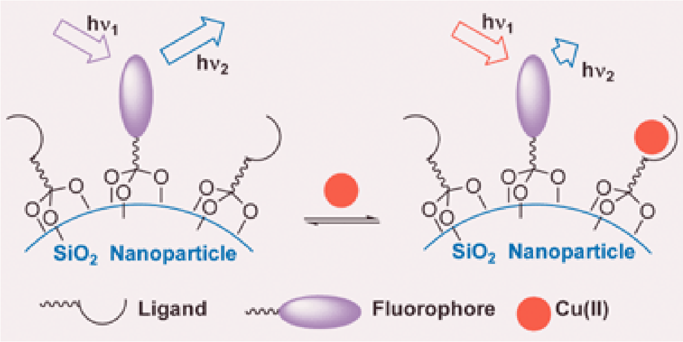

Figure 1.5. Self-organized fluorescent chemosensors on silica nanoparticles

Multivalency plays also a crucial role in tuning the catalytic activity of a catalyst especially when it is, for example, assembled on the surface of a nanoparticle. The reason is that the surface not only brings the substrate and catalyst in close proximity but also can generate a favourable microenvironment. The multivalent scaffolds mentioned before, such as dendrimers, micelles, and nanoparticles, can act as “artificial enzymes” thanks to their increased structural complexity compared to traditional molecular systems.

The term “artificial enzyme” was coined originally by Breslow and can be defined as a synthetic, organic molecule prepared to recreate the active site of an enzyme.[22] Substrate binding can be achieved by metal coordination, ion paring, hydrogen bonding and its approach to functional groups in the enzyme causes catalysis by so called proximity effects. Functionalization of multivalent structures with catalytically active groups promotes the same proximity effect and it can result in very potent catalysts. This catalytic amplification depends on parameters related to the use of nanoscale objects including size, shape, surface chemistry, flexibility/rigidity, architecture and elemental composition and it is named dendritic effect. [23]

Furthermore, the multivalency of the catalytic system may be exploited to induce substrate selectivity, considering the improved ability for molecular recognition mentioned above. This is in particular the case when the substrate itself contains multiple reactive sites. In an example reported by Reymond[24] strong positive dendritic effect in the ester hydrolysis reactions catalyzed by dendrimers displaying multiple histidine residues at their surface was observed. Hydrolysis seems to occur by nucleophilic catalysis by the histidine side-chain.

They investigated a systematic peptide dendrimer series of increasing generation number containing a catalytic sequence His-Ser in all branches in order to determine the contribution of the dendrimer structure in catalysis.

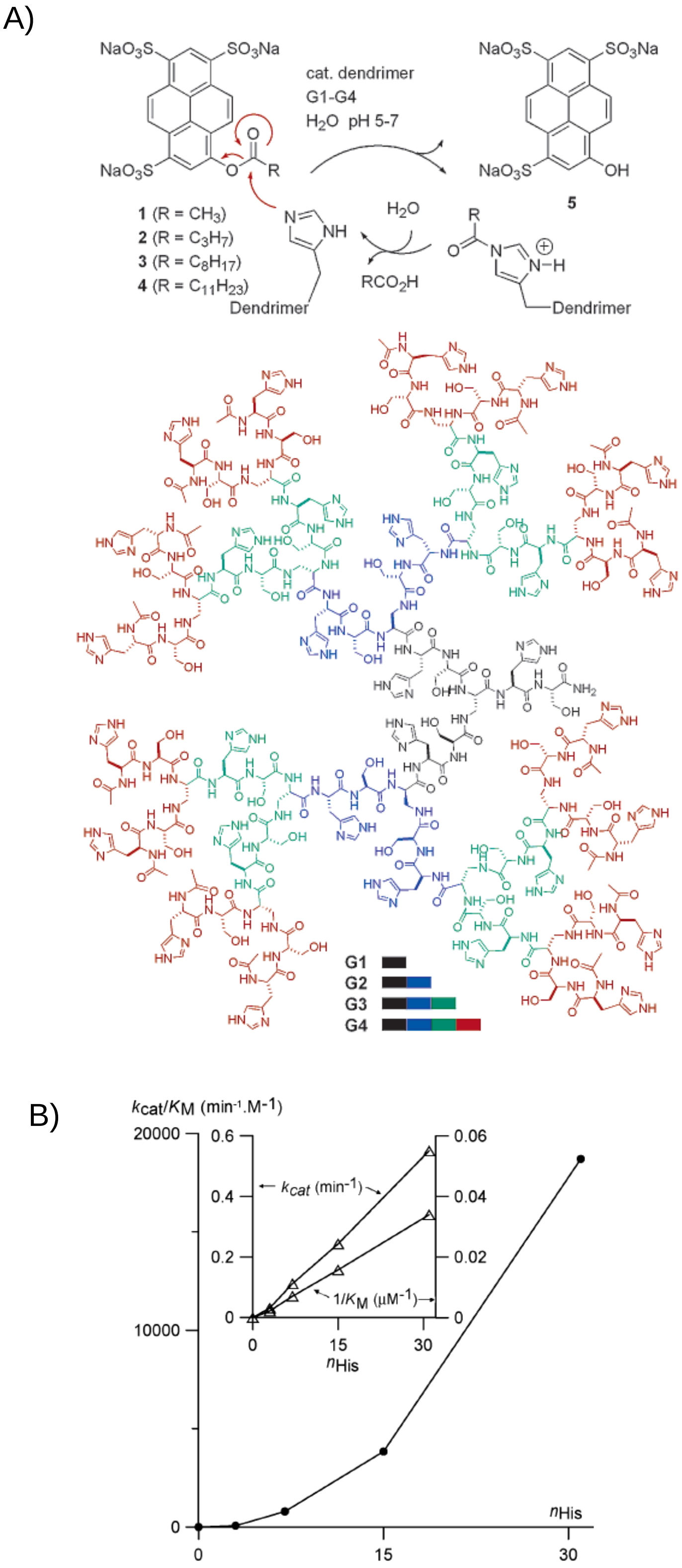

Figure 1.6. A) Peptide dendrimer for ester hydrolysis reaction B) K_{cat}/K_M as a function of histidines' number

They found a strong positive dendritic effect due to 50-fold increase of K_M from G1 to G4 (Figure 1.6 A and B) This effect can be ascribed to catalytically productive interactions such as modulation of the histidine side-chain's pK_a and creation of a hydrophobic microenvironment allowing substrate binding by the acyl chains.

1.2. MONOLAYER PROTECTED GOLD NANOPARTICLES

Gold nanoparticles (Au NP) have a rich history in chemistry, dating back to ancient Roman times where they were used to stain glasses for decorative purposes. The modern era of Au NP synthesis began over 150 years ago with the work of Michael Faraday, who was possibly the first to realize that colloidal gold solutions have properties that differ from bulk gold. Reliable and high-yielding methods for the synthesis of Au NP, including those with spherical and nonspherical shapes, have been developed over the last half century.[25,26] The resulting AuNPs have unique properties, such as size- and shape-dependent optical and electronic features, a high surface area to volume ratio, and surfaces that can be readily modified with ligands containing functional groups[27] such as thiols, phosphines, and amines, which exhibit affinity for gold surfaces.[28] As the size or shape of the nanoparticle changes, the observed colour also changes. This colour is due to the collective oscillation of the electrons in the conduction band, known as the surface plasmon oscillation. The plasmon resonance absorption has an absorption coefficient orders of magnitude larger than strongly absorbing dyes. This characteristic can contribute to the signal amplification arises from this collective phenomena between the pre-organized gold core.[29] Fluorescence quenching is another commonly observed consequence when fluorophores are appended onto AuNPs. [30] This quenching can occur when the emission spectrum overlaps with the gold surface plasmon band.[31] Pronounced fluorescence quenching is also observed for the smallest nanoparticles of 1 nm radius that do not present plasmonic band. Both radiative and nonradiative processes are particle dependent, with higher efficiencies of quenching occurring with small nanoparticles.[32,33] This quenching is caused not only by an increased nonradiative rate but, equally important, by a drastic decrease in the dye's radiative rate.[34] From this point of view Au NP can serve as excellent fluorescence quenchers for FRET-based assays due to their extraordinary high molar extinction coefficients and broad energy bandwidth.

The core nanomaterial only partly determines NP properties; the surface-bound molecular species are equally important in determining overall behaviour. The monolayer acts as a barrier between the nanoparticle core and the environment, and effectively protects and stabilizes the core integrity. Furthermore, the reactivity and solubility of the nanoparticles are dictated by the chemical nature of the monolayer periphery. Beyond this, the surface molecular monolayer is also crucial for adding function and defining properties. The cooperative and collective effects achieved by the organization of the organic components on the particle provide a multivalent suitable surface.

As above-mentioned multivalent binding involves the simultaneous interactions of multiple complementary functionalities and this multivalency can drastically increase the significance of weak intermolecular forces and the selectivity of the recognition. Multivalent interactions can, hence, be applied universally for a targeted strengthening of an interaction between different interfaces or small molecules. Thanks of this ability, Au NP have been exploited in various fields i.e, sensing, catalysis, and to create modular systems. Some key examples will be discussed in the next sections.

1.2.1. Sensing

As a result of their interesting properties mentioned before, in particular the surface plasmon resonance that essentially depends on the size, shape, and distance between the NPs, Au NP have been widely used in various research and industrial fields.[15] For instance, based on the colour change of Au NP caused by the controllable change in their dispersion/aggregation states, Au NP have been used for colorimetric visualization of trinitrotoluene (TNT) down to the picomolar level (Figure 1.7 B). By using Au NP and by taking advantage of the donor-acceptor (D–A) interaction between TNT and cysteamine at the AuNP/solution interface, the group of Mao[35] developed a very sensitive assay able to detect TNT also in real matrix exploiting both the optical properties of the nanoparticles and the multivalent D-A interactions. In this example the multivalent surface promotes, in the presence of TNT, the stabilization of the interaction between interfaces of different Au NP, provoking a change in the colloidal dispersion and, as a consequence a change in the color of the solution.

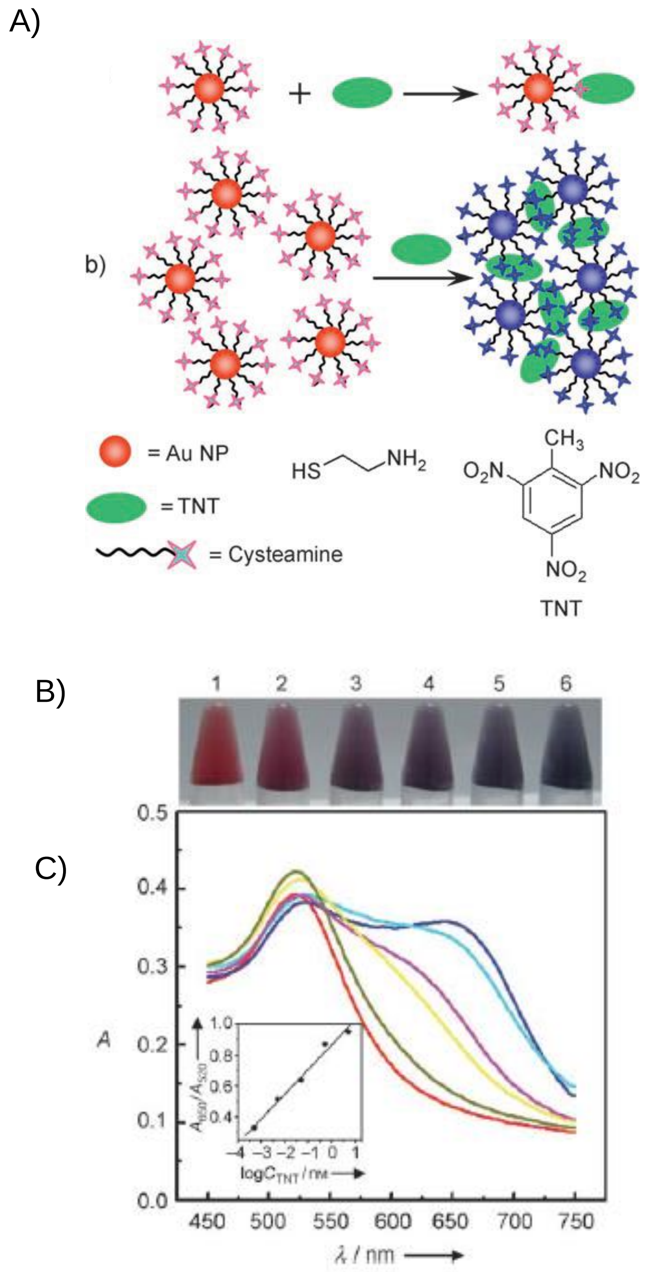

Figure 1.7. A) Schematic representation of colorimetric assay for the detection of TNT B) Colorimetric visualization of TNT by using Au NP (containing 500 nm cysteamine). TNT concentrations varied from $5{\cdot}10^{-13}$ (2) to $5{\cdot}10^{-9}$ M(6). C) UV/Vis spectra of the Au NP suspensión (10 nm) containing 500 nm cysteamine in the presence of different concentrations of TNT: red, 0 M; dark yellow, $5{\cdot}10^{-13}$ M; yellow, $5{\cdot}10^{-12}$M; magenta, $5{\cdot}10^{-11}$M; cyan, $5{\cdot}10^{-10}$M; blue, $5{\cdot}10^{-9}$M.

In the same way Au NP, have been widely used for FRET-based assays[31] due to their extraordinary high molar extinction coefficients and broad energy bandwidth yielding them excellent fluorescence quenchers.[36] Various examples of FRET-based assays for the detection of metal ions have been reported in which the selectivity of the assay depended on the chemical nature of the surrounding monolayer.[37,38,39,40]

Besides detecting metal ions, FRET based Au NP assays have also been utilized for sensing small organic molecules. Tang et al. proposed in 2008 an example of indicator displacement assay[41] (IDA) for the detection of cholesterol that included the use of βcyclodextrin (β-CD). Inclusion of fluorescein (FL) into β-cyclodextrin makes fluorescence resonance energy transfer (FRET) occur through the donor and nearby quencher, resulting in fluorescence quenching. In the presence of cholesterol, FL inside β-CD is replaced by the cholesterol because of their higher binding affinity to β-CD, restoring FL fluorescence for detection of cholesterol at nanomolar concentrations.

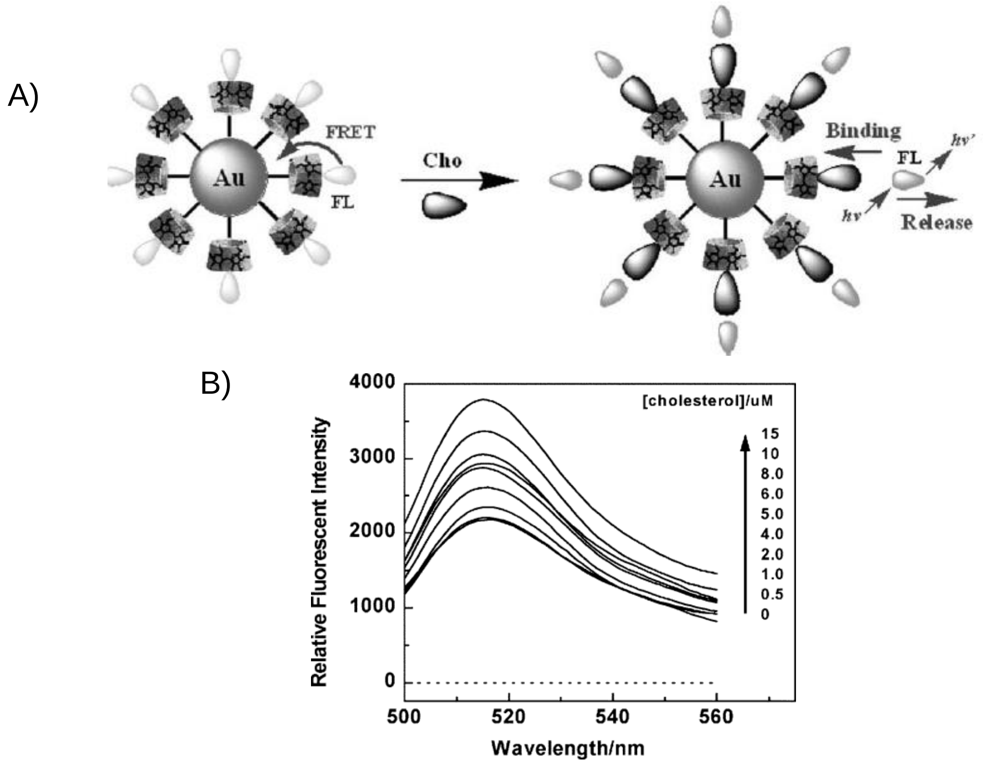

Figure 1.8. A) schematic illustration of its FRET-based operating principles B) Fluorescence spectra of 0.2x Au NP-βCD solutions after adding varying amounts of cholesterol. FL, 10 nM; Tris-HCl buffer, pH 7.6, 20 mM. All spectra were obtained after incubation at 37 °C for an equilibration period of 30 min

Au NP feature excellent conductivity, high surface area and catalytic properties[14] that make them excellent materials for the electrochemical detection of a wide range of analytes.[42,43,44,45] Willner et al.[46] exploited the presence of Au-nanoparticles to yield a three-dimensional conductive superstructure that allows the electrochemical sensing of p–hydroquinone and ferrocene derivatives.

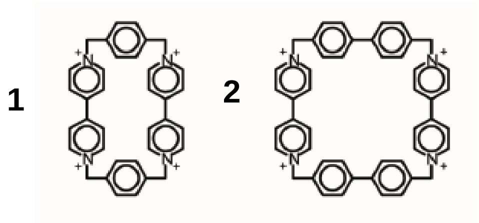

Chart 1

The superstructure was constructed via electrostatic cross-linking of citrate-stabilized Au NP (12 ± 1 nm) and oligocationic cyclophanes (blue squares in Figure 1.9). The assembly was built in a stepwise manner to attain layer by layer assembly of anionic Au NP and oligocationic cyclophanes. The bipyridinium cyclophane (Chart 1 compound **2**) acts as a host for p-donor compounds such as ferrocene and its derivatives.[47]

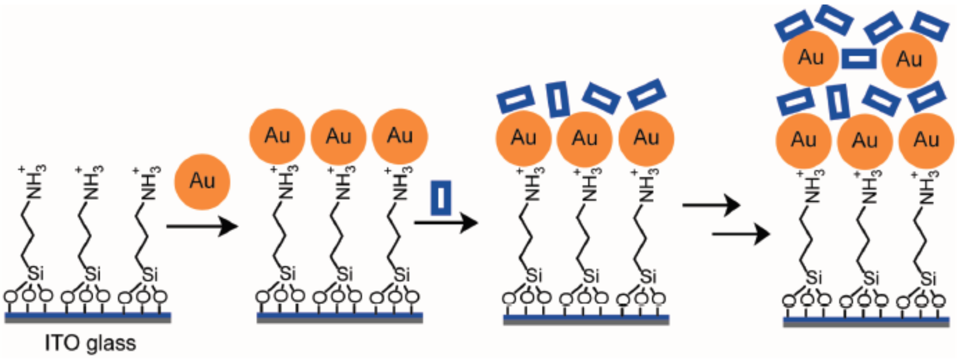

Figure 1.9. Three dimensional array of the bis-bipyridinium cyclophane crosslinked Au-nanoparticle superstructure on a conductive ITO support.

Accordingly, the **2**-crosslinked Au-array was used as a sensing matrix for dihydroxymethyl ferrocene. At a bare ITO electrode, no electrical response for this analyte was observed at concentrations below 10^{-4}M. Upon increasing the number of Au nanoparticle layers, the electrical response of the molecular glue component (E= -0.48 V) was enhanced, and the amperometric responses were proportionally higher (Figure 1.10 A (a-f)). These results further indicate that the analyte was concentrated at the receptor cyclophane:Au colloid functionalized electrode, and that the inner layers are accessible to the solution.

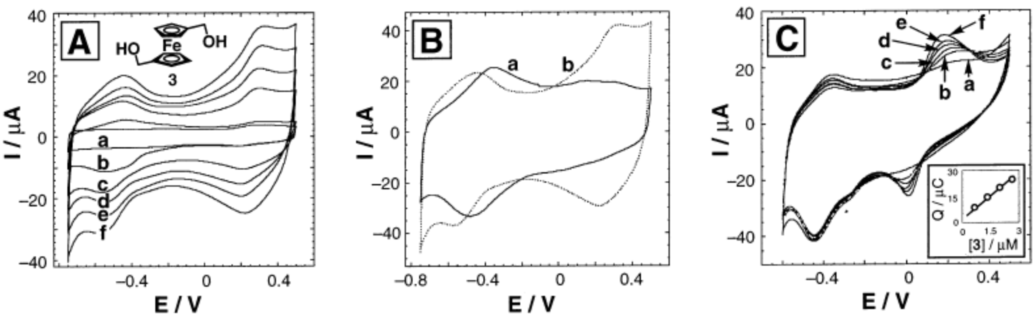

Figure 1.10. A) Cyclic voltammograms of the layered **2**-Au-colloid arrays in the presence of 1×10^{-6} M of ferrocene derivative. (A) Unmodified ITO electrode. (b–f) One to five Au-nanoparticle layers. (B) Cyclic voltammograms of five layer electrodes constructed using cyclophanes **1** (curve a) and **2** (curve b) as crosslinkers in the presence of dihydroxymethyl ferrocene (1×10^{-6} M). (C) Cyclic voltammograms of a layered 2-Au-nanoparticle array (five layers) in the absence of dihydroxymethyl ferrocene (curve a) and at various concentrations ; (b) 0.7×10^{-6} M; (c) 1.3×10^{-6} M; (d) 2.0×10^{-6} M; (e) 2.6×10^{-6} M; (f) 5.2×10^{-5} M.

The five-layer bipyridinium cyclophane functionalized electrode (Figure 1.10 A (f)) was used as a sensing electrode for dihydroxymethyl ferrocene. Figure 1.10 C (a-f) shows the cyclic voltammograms of the functionalized electrode at different concentrations of the ferrocene derivative. In addition analogous architectures have been constructed using cyclobis (paraquat-p-phenylene) (Chart 1 compound **1**) as a crosslinker[48] and were shown to exhibit sensitivity for hydroquinone and its derivatives, but not for ferrocene derivatives.

1.2.2. Catalysis

Several reasons exist why Au NP are of particular interest for application in catalysis. The monolayer obtained through a self-assembly process driven by the formation of (most frequently) a stable Au–S bond results in the straightforward formation of a multivalent system similar to micelles, but with a significant higher stability. Furthermore the use of self-assembly marks a difference compared to, for example, catalytic dendrimers which are typically obtained through covalent synthesis.[49] Anchoring of thiols on the gold surface induces a unidirectional orientation of these molecules, which means that the self-assembly process contains an element of topological control. This self-assembled monolayer can play a crucial role in determining the catalytic properties of the system. The multivalency of the catalytic system may be exploited to induce substrate selectivity, in particular in the case when the substrate itself contains multiple reactive sites, or an improvement of the catalytic properties promoting cooperativity.[50] A first example of a transition-metal complex immobilized on gold nanoparticles was reported in 1998 by Tremel et al.[51] Catalytic AuNPs functionalized with 4-methylhexa-3,5-diene-1-thiol in the presence of $RuCl_3$ were used as such for the ring-opening metathesis polymerization (ROMP) of norbornene. Although not soluble in the reaction medium (dichloromethane), the obtained system showed an impressive increase in the TOF compared to the molecular catalyst (16 000 h^{-1} against 3000 h^{-1}). The authors tentatively ascribed this effect to the orientation of the catalyst on the surface, which favours its interaction with the monomer and the growing polymer chain.

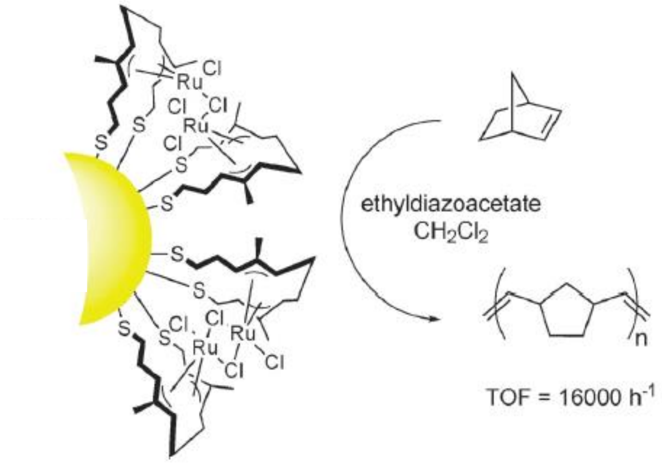

Figure 1.11. Catalytic system used for ring-opening metathesis polymerization

An example in which cooperativity is a key element for catalysis is reported by Scrimin and coworkers.[52] Most of RNase enzymes require the cooperative action of at least two metal ions in the active site. This is why the precise preorganization of the functional groups participating in the reaction is a crucial point. Based on this principle, Scrimin *et al.* developed a catalytic system composed of 2 nm-sized Au nanoparticles covered with 1,4,9-triazacyclonanone(TACN)-Zn(II)-terminating thiols. The system proposed promotes the cleavage of the phosphate bond of phosphodiesters as a model and displays a rate acceleration of over 40000 (k_{cat}/k_{uncat}) compared to the background reaction.

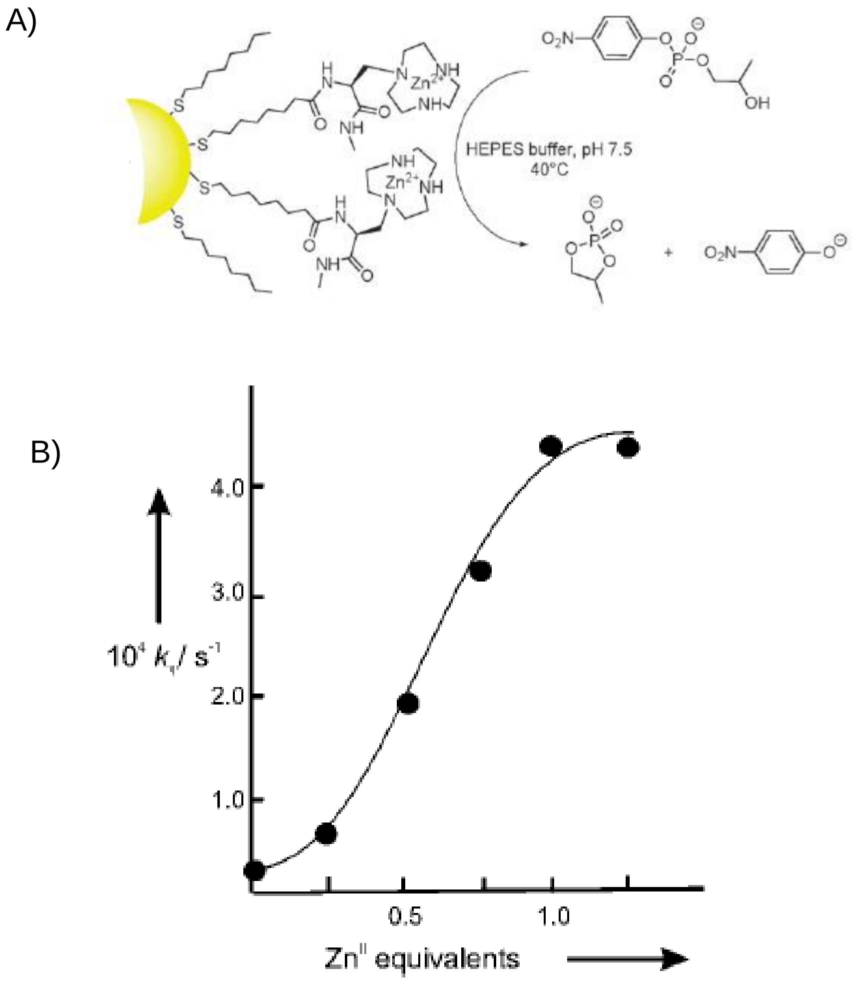

Figure 1.12. A) Catalytic system used for transphosphorylation reaction. B) Dependence of the rate of cleavage of HPNP by AuNPs·Zn^{2+} as a function of pH value.

The reactivity profile obtained by progressively adding Zn^{2+} ions to a solution of catalyst up to the saturation of the metal-ion binding subunits is reported in Figure 12 B. This kinetic analysis reveals that the most active system is the one fully loaded with Zn^{2+} ions. The sigmoidal profile of the curve supports cooperativity between the metal centers because the catalytic efficiency becomes much higher after the first 30% of Zn^{2+} ions is added.

1.2.3. Systems Modulation

As shown before, on the base of multivalency a large number of synthetic systems can be designed and studied not just for the recognition of simple molecules or more challenging biological targets and catalysis but also for the creation of tunable materials.[53] One way, is to combine the ability to change the physico-chemical characteristics upon an external stimulus (pH, light ..) of molecular or supramolecular switches and the unique characteristics of AuNPs.

A molecular switch is a molecule that can be reversibly shifted between two or more stable states using an external stimulus such as light[54,55] redox potential [56,57,58] or pH gradient[59,60]. Once embedded on the surface of nanoparticles, the switches can endow these with a rich variety of behavior and affect optical, electrical, magnetic, fluorescent, controlled release, and aggregation properties of the NPs.

Liu et al.[61] proposed a modular system based on Au NP in which the pH dependant switch is “i-motif’’ DNA, a four-stranded DNA secondary structure which can form in cytosine-rich sequences. They synthesized two different batches of nanoparticles. The first one (NP **1**) consisted of Au NP conjugated with a cytosine rich DNA strand (30-mer), containing 4 stretches of CCC known as the ‘‘i motif’’, and the second one (NP **2**) consisting of Au NP conjugated with a DNA strand (27-mer) complementary to the ‘‘i motif’’ but with 3 C–T mismatches. In acidic pH (~5), the C residues are partially protonated. The ‘‘i motif’’ on NP **1** forms a DNA quadruplex trough systematic intercalation of the semi-protonated C-C$^+$ bases, while the other strand on NP **2** adopts a random-coil conformation. When the pH of the solution is increased to ~8, the C residues are all deprotonated, and the ‘‘i motif’’ unfolds. Hybridization between the strands on NP **1** and NP **2** takes place, leading to aggregation of the AuNPs that causes a colour change from purple to red (Figure 1.13). This conversion between states of intra-molecular quadruplex and inter-molecular duplex of DNA can be achieved by alternate additions of H^+ and OH^-.

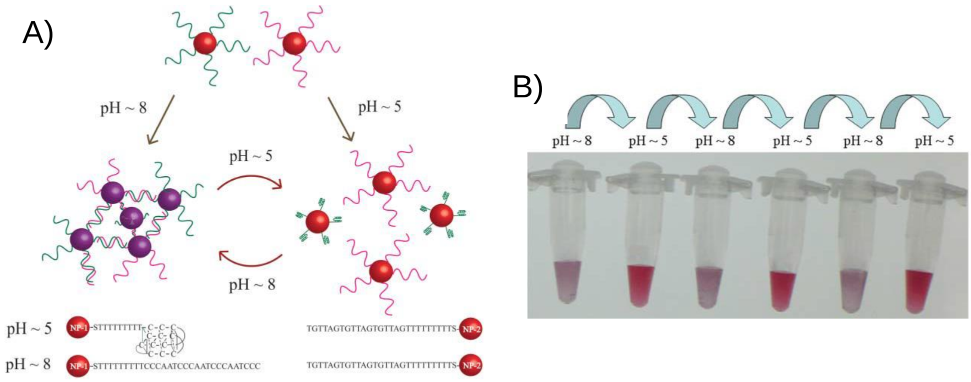

Figure 1.13. A) A Schematic illustration of the working cycle and color change of gold nanoparticle-DNAassembly at different pH of the solution and DNA sequences used herein. B) A picture showing the reversibility and color change of the DNA–gold conjugates at different pH. The pictures are takeny 30 min aftereach pH change.

Another possibility to modulate the properties of the gold nanoparticles thanks to the presence of an organic switching molecule is to exploit their redox abilities.

An interesting example by Nichols *et al.* reports on the use of scanning tunnelling microscopy measurements which shows that organic molecules containing redox centres can be used to attach metal nanoparticles to electrode surfaces and, in that way, control the electron transport between them.[62]

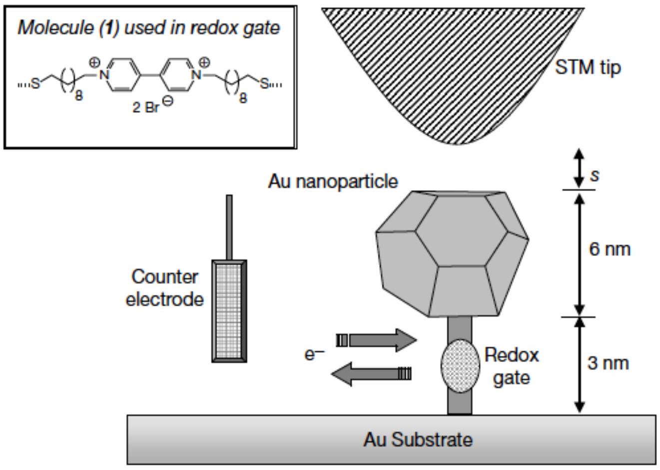

Figure 1.14. Schematic representation of the nanoscopic device. STM was used to examine the electrical characteristics of this device. Electrons can be injected into the redox gate by applying a suitable potential between the substrate and the counter electrode. The potential between the tip and the substrate (V bias) is controlled independently, and s represents the tip–nanoparticle distance. The redox gate consists of up to 60 of the molecules shown in the inset. The counter electrode is immersed in the surrounding electrolyte.

The redox switchable group used was a bipyridinium (viologen) moiety located at the centre of a chain of 20 methylene units in an α,γ-polymethylenedithiol compound. The two-thiolated ending chains were used to connect Au NP and the Au surface creating sandwiched molecular layers. The potential dependence of the current, plotted as (dI/dV_{bias}, Figure 1.15), was measured in order to highlight the potential dependence of the tunnelling conductivity. The solid line shows the tunnelling conductance of the nanoparticle assembly containing the viologen moieties. A very sharp resonance peak can be seen for tunnelling through the structure. The dashed line corresponds to the control experiment, in which gold nanoparticles were placed over a hexanedithiol monolayer. No peak is seen in the control experiment, showing that the resonance is related to the presence of the redox ligand within the nanoparticle–metal junction.

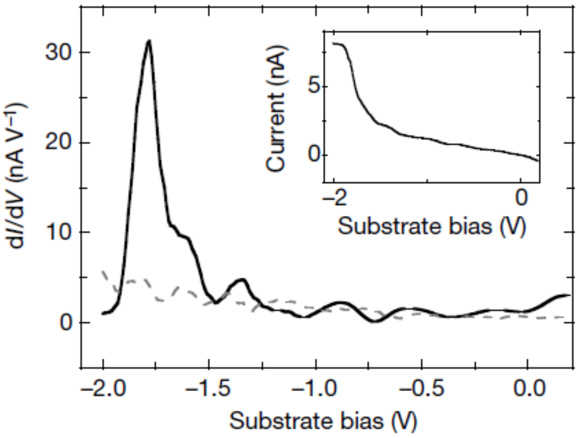

Figure 1.15. A current–voltage curve (inset) and its derivative (dI/dVbias) The STM tip was positioned above an isolated gold nanoparticle for these measurements. The dotted line corresponds to the control experiment, in which gold nanoparticles were deposited on a hexanedithiolmonolayer.

In this paper the authors demonstrated that redox switching caused the changes in the electronic properties of the junction. Indeed, when the redox group in the junction is reduced, the electronic wavefunction of the gold surface, the bipy$^{\bullet+}$ moiety and the nanoparticle extensively couple, leading to conductivity in the junction.

Finally, the combination of molecular switches and gold nanoparticles can be applied also to control the release of small molecules from the surface.
Thomas and co-authors[63] designed a photoswitchable double-shell structure on Au nanoparticle core, consisting of photochromic spiropyran (SP) as the first shell which conformational change upon irradiation can be used to regulate the assembly and disassembly of an outer shell of an amino acid derivative . Photochromic, thermochromic, solvatochromic and electrochromic characteristics of spiropyrans make them especially important.[64] In particular spiropyran undergoes photochemical ring opening as well as the thermal/photochemical ring closure of its zwitterionic merocyanine form (MC). This ability is, also, maintained when it is constrained on the surface through an alkyl-thiolated chain. In this experiments they wanted to take in advantage the possibility to form a stable complex between the zwitterionic merocyanine form on Au nanoparticles and amino acid derivatives.

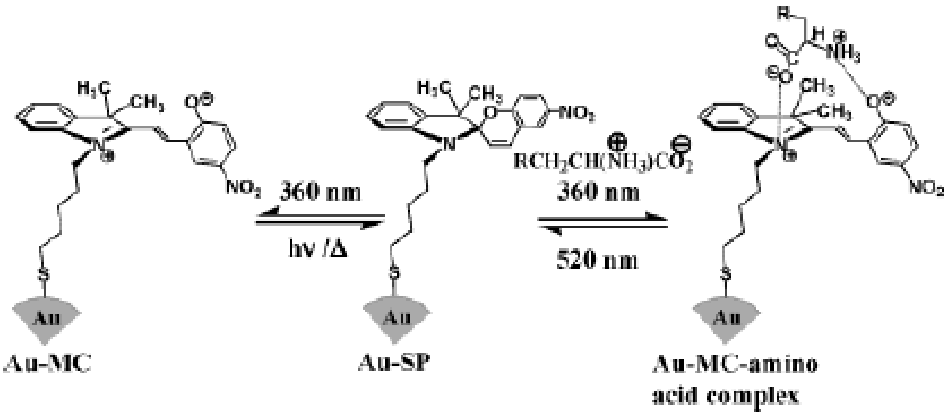

Figure 1.16. Schematic Representations of the Photochemical Ring Opening and Closing of Au-SP in the Absence and in the Presence of Amino Acids

Photoswitching of Au-SP was investigated in the presence of various amino acid derivatives such as L-tryptophan, L-tyrosine, L-DOPA, and R-methyl-L-DOPA. The absorption spectra of Au-SP remains unaffected on addition of a saturated solution of various amino acid derivatives under dark conditions (e.g., trace a in Figure 1.17), that means that the system Au-SP is not affected by the presence of the amino acids. After irradiation at 360 nm formation of a visible absorption band (trace b in Figure 1.17) was observed.

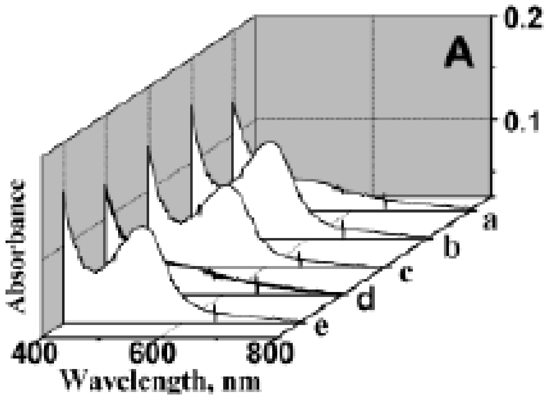

Figure 11.7. Absorption spectra of (a) a methanolic solution of Au-SP containing L-DOPA (42 mM), (b) immediately after irradiation with UV light (360-nm band-pass filter), (c) after 2 h, (d) after further irradiation with visible light (520-nm band-pass filter), and (e) after subsequent irradiation with UV light (360-nm band-pass filter).

The first observation is that, in the presence of amino acids, an initial decrease in the intensity of the visible absorption band was observed, but, then, the absorbance persisted, indicating the stabilization of the zwitterionic merocyanine form (trace c in Figure 17). On the contrary the absence of any amino acid allowed the quick thermal ring closure of Au-MC. It indicated the formation of a stable complex between Au-MC and the aminoacids, which prevented the thermal ring closure of Au-MC. The switch to the SP form can, however, be achieved by irradiation at 520 nm and undergoes thermal ring closure to Au-SP, releasing the amino acid derivatives (trace d in Figure 17).

1.3. CONCEPT OF THE THESIS

The examples discussed in the introduction have demonstrated the power of monolayer protected gold nanoparticles as unique scaffold for catalysis, recognition purposes and tuneable nanosystems. The general scope of this thesis is to extend the use of Au NP as multivalent systems for the development of complex functional systems.

In Chapter **2** the possibility to broaden the spectrum of reactions that can be catalyzed by Au NP will be investigated. The final scope here is to induce asymmetric catalysis of C-C bond forming reactions using catalytic systems composed of catalytic units embedded in a self-assembled chiral environment surrounding gold nanoparticles.

Chapter **3** will deal with the development of a universal assay able to detect a broad range of different small organic molecules. The main aim will be to create a modular system in which the design and synthetic steps are reduced to a minimum. The possibility to modulate the selectivity of the assay by simply changing or adding a different host is one of the key targets. This system should provide a controlled access to sensing systems of higher complexity that go beyond those developed to detect a single analyte.

Chapter **4** introduces the use of self-assembled molecular switches to the surface of Au NP. They will be used as “cofactors” to modulate by light in a reversible manner the controlled release of small molecules and the catalytic activity of Au NP.

1.4. BIBLIOGRAPHY

1. Sanchez, C., Arribart, H. & Guille, M. M. G. Biomimetism and bioinspiration as tools for the design of innovative materials and systems. *Nat. Mater.* **4,** 277–288 (2005).
2. Mark J.E, Lee C. Y-C, Hybrid Organic-Inorganic Composites. ACS Symposium Series; American Chemical Society: Washington, DC (1995).
3. Lehn J. Supramolecular Chemistry. *Science* **260** (1993).
4. Lehn, J. Supramolecular Chemistry: Concepts and Perspectives. Wiley-VCH: Weinheim, Germany*.* 1995).
5. Whitesides, G. Nanoscience, Nanotechnology, and Chemistry. *Small* **1,** 172–179 (2005).
6. Sanchez, F. & Sobolev, K. Nanotechnology in concrete – A review. *Constr. Build. Mater.* **24,** 2060–2071 (2010).
7. Whitesides, G. M. & Boncheva, M. Beyond molecules: self-assembly of mesoscopic and macroscopic components. *Proc. Natl. Acad. Sci. U. S. A.* **99,** 4769–74 (2002).
8. Velonia, K. Protein-polymer amphiphilic chimeras: recent advances and future challenges. *Polym. Chem.* **1,** 944 (2010).
9. Lim, Y., Moon, K.-S. & Lee, M. Rod-coil block molecules: their aqueous self-assembly and biomaterials applications. *J. Mater. Chem.* **18,** 2909–2918 (2008).
10. Whitesides, G. M. The once and future nanomachine. *Sci. Am.* **285,** 78–83 (2001).
11. Whitesides, G. M., Mathias, J. P. & Seto, C. T. Molecular self-assembly and nanochemistry: a chemical strategy for the synthesis of nanostructures. *Science* **254,** 1312–1319 (1991).
12. McNeil, S. E. Nanotechnology for the biologist. *J. Leukoc. Biol.* **78,** 585–594 (2005).
13. Shevchenko, E. V., Talapin, D. V., Kotov, N. A., O'Brien, S. & Murray, C. B. Structural diversity in binary nanoparticle superlattices. *Nature* **439,** 55–59 (2006).
14. Katz, E. & Willner, I. Integrated Nanoparticle-Biomolecule Hybrid Systems: Synthesis, Properties, and Applications. *Angew. Chem. Int. Ed.* **43,** 6042–6108 (2004).
15. Daniel, M.-C. & Astruc, D. Gold nanoparticles: assembly, supramolecular chemistry, quantum-size-related properties, and applications toward biology, catalysis, and nanotechnology. *Chem. Rev.* **104,** 293–346 (2004).
16. Krishnamurthy, V. M., Estroff, L. a & Whitesides, G. M. Approaches in Drug DiscoVery Wiley-VCH: Weinheim, Germany*.* (2006).

17. Descalzo, a B., Martínez-Mañez, R., Sancenón, F., Hoffmann, K. & Rurack, K. The supramolecular chemistry of organic-inorganic hybrid materials. *Angew. Chem. Int. Ed.* **45,** 5924–5948 (2006).

18. Ercolani, G. Assessment of Cooperativity in Self-Assembly. *J. Am. Chem. Soc.* **125,** 16097–16103 (2003).

19. Major, R. C. & Zhu, X.-Y. The surface chelate effect. *J. Am. Chem. Soc.* **125,** 8454–5 (2003).

20. Montalti, M., Prodi, L., Zaccheroni, N. & Falini, G. Solvent-induced modulation of collective photophysical processes in fluorescent silica nanoparticles. *J. Am. Chem. Soc.* **124,** 13540–13546 (2002).

21. Brasola, E., Mancin, F., Rampazzo, E., Tecilla, P. & Tonellato, U. A fluorescence nanosensor for Cu2+ on silica particles. *Chem. Commun.* **2,** 3026–3027 (2003).

22. Breslow, R. Biomimetic chemistry and artificial enzymes: catalysis by design. *Acc. Chem. Res.* **28**, 146–153 (1995).

23. Tomalia, D. a. Dendritic effects: dependency of dendritic nano-periodic property patterns on critical nanoscale design parameters (CNDPs). *New J. Chem.* **36,** 264 (2012).

24. Delort, E., Darbre, T. & Reymond, J.-L. A strong positive dendritic effect in a peptide dendrimer-catalyzed ester hydrolysis reaction. *J. Am. Chem. Soc.* **126,** 15642–15643 (2004).

25. Daniel, M. C. & Astruc, D. Gold Nanoparticles: Assembly, Supramolecular Chemistry, Quantum-Size-Related Properties, and Applications Toward Biology, Catalysis, and Nanotechnology. *Chem. Rev.* **104,** 293–346 (2004).

26. Brust, M., Walker, M., Bethell, D., Schiffrin, D. J. & Whyman, R. Synthesis of Thiol-derivatised Gold Nanoparticles *Chem Comm*. **17**, 801–802 (1994).

27. Astruc, D., Lu, F. & Aranzaes, J. R. Nanoparticles as recyclable catalysts: the frontier between homogeneous and heterogeneous catalysis. *Angew. Chem. Int. Ed.* **44,** 7852–72 (2005).

28. Giljohann, D. A. Seferos, D. S., Daniel, W. L., Massich, M. D., Patel, P. C., and. Mirkin, C. A. Gold Nanoparticles for Biology and Medicine. *Angew. Chem. Int. Ed.* **49,** 3280–3294 (2010).

29. Burda, C., Chen, X., Narayanan, R. & El-Sayed, M. A. Chemistry and properties of nanocrystals of different shapes. *Chem. Rev.* **105,** (2005).

30. Imahori, H. Arimura, M., Hanada T., Nishimura, Y., Yamazaki, I., Sakata, Y. and Fukuzumi S. Photoactive Three-Dimensional Monolayers: Porphyrin-Alkanethiolate-Stabilized Gold Clusters Hiroshi *J. Am. Chem. Soc.* **123**, 335-336 (2001),

31. Sapsford, K. E., Berti, L. & Medintz, I. L. Materials for Fluorescence Resonance Energy Transfer Analysis: Beyond Traditional Donor–Acceptor Combinations. *Angew. Chem. Int. Ed.* **45,** 4562–4589 (2006).

32. Bigioni, T. P., Whetten, R. L. & Dag, Ö. Near-Infrared Luminescence from Small Gold Nanocrystals. *J. Phys. Chem. B* **104,** 6983–6986 (2000).

33. Link, S. & El-Sayed, M. A Shape and size dependence of radiative, non-radiative and photothermal properties of gold nanocrystals. *Int. Rev. Phys. Chem.* **19,** 409–453 (2000).

34. Dulkeith, E., Morteani, A.C., Niedereichholz, T., Klar, T.A. and Feldmann J. Fluorescence Quenching of Dye Molecules near Gold Nanoparticles: Radiative and Nonradiative Effects. *Phys. Rev. Lett.* **89,** 203002 (2002).

35. Jiang, Y., Zhao H., Zhu N., Lin Y., Yu P. and Mao L. A simple assay for direct colorimetric visualization of trinitrotoluene at picomolar levels using gold nanoparticles. *Angew. Chem. Int. Ed.* **47,** 8601–8604 (2008).

36. Jain, P. K., El-Sayed, I. H. & El-Sayed, M. A. Au nanoparticles target cancer. *Nano Today* **2,** 18–29 (2007).

37. Ray, P. C., Fortner, A. & Darbha, G. K. Gold nanoparticle based FRET assay for the detection of DNA cleavage. *J. Phys. Chem. B* **110,** 20745–8 (2006).

38. Chen, N.-T., Cheng, S.-H., Liu, C.-P., Souris, J. S., Chen, C.-T. Mou, C.-Y., Lo, L.-W. Recent advances in nanoparticle-based förster resonance energy transfer for biosensing, molecular imaging and drug release profiling. *Int. J. Mol. Sci.* **13,** 16598–623 (2012).

39. Chen, G., Song, F., Xiong, X. & Peng, X. Fluorescent Nanosensors Based on Fluorescence Resonance Energy Transfer (FRET). *Ind. Eng. Chem. Res.* **52,** 11228–11245 (2013).

40. Saha, K., Agasti, S. S., Kim, C., Li, X. & Rotello, V. M. Gold nanoparticles in chemical and biological sensing. *Chem. Rev.* **112,** 2739–2779 (2012).

41. Nguyen, B. T. & Anslyn, E. V. Indicator-displacement assays. *Coord. Chem. Rev.* **250,** 3118–3127 (2006).

42. Luo, X., Morrin, A., Killard, A. J. & Smyth, M. R. Application of Nanoparticles in Electrochemical Sensors and Biosensors. *Electroanalysis* **18,** 319–326 (2006).

43. Drummond, T. G. *et al.* Electrochemical DNA sensors. *Nat. Biotechnol.* **21,** 1192–9 (2003).

44. Guo, S. & Wang, E. Synthesis and electrochemical applications of gold nanoparticles. *Anal. Chim. Acta* **598,** 181–192 (2007).

45. Castañeda, M. T., Alegret, S. & Merkoçi, a. Electrochemical sensing of DNA using gold nanoparticles. *Electroanalysis* **19,** 743–753 (2007).

46. Lahav, M., Shipway, A. N., Willner, I., Nielsen, M. B. & Stoddart, J. F. An enlarged bis-bipyridinium cyclophane-Au nanoparticle superstructure for selective electrochemical sensing applications. *J. Electroanal. Chem.* **482,** 217–221 (2000).

47. Ashton, P. R., Menzer, S., Raymo, F. M., Shimizu, G. K. H., Stoddart, J. F., Williamsb, D. J.The template-directed synthesis of cyclobis (paraquat-4 , 4 ’ -biphenylene). *Chem. Comm.* **4,** 487–490 (1996).

48. Lahav, M., Shipway, A. N. & Willner, I. Au-nanoparticle–bis-bipyridinium cyclophane superstructures: assembly, characterization and sensoric applications. *J. Chem. Soc. Perkin Trans. 2* 1925–1931 (1999). doi:10.1039/a902763g

49. Astruc, D. & Chardac, F. Dendritic catalysts and dendrimers in catalysis. *Chem. Rev.* **101,** 2991–3023 (2001).

50. Pieters, G. & Prins, L. J. Catalytic self-assembled monolayers on gold nanoparticles. *New J. Chem.* **36,** 1931 (2012).

51. Bartz, M., Küther, J., Seshadri, R. & Tremel, W. Colloid-bound catalysts for ring-opening metathesis polymerization: A combination of homogenous and heterogeneous properties. *Angew. Chem. Int. Ed.* **37,** 2466–2468 (1998).

52. Manea, F., Houillon, F. B., Pasquato, L. & Scrimin, P. Nanozymes: Gold-nanoparticle-based transphosphorylation catalysts. *Angew. Chem. Int. Ed.* **43,** 6165–6169 (2004).

53. Fahrenbach, A. C., Warren S. C., Incorvati J. T., Avestro A.-J., Barnes J. C., Stoddart J. F. and Grzybowski B. A. Organic Switches for Surfaces and Devices. *Adv. Mater.* **25,** 331–348 (2013).

54. Bortolus, P. & Monti, S. Cis/Trans Photoisomerization of Azobenzene-Cyclodextrin Inclusion Complexes *J. Phys. Chem.*, **91**, 5046–5050 (1987).

55. Fujimoto, T., Nakamura, A., Inoue, Y., Sakata, Y. & Kaneda, T. Photoswitching of the association of a permethylated ??-cyclodextrin-azobenzene dyad forming a Janus [2]pseudorotaxane. *Tetrahedron Lett.* **42,** 7987–7989 (2001).

56. Asakawa, M., Ashton, P. R., Balzani, V., Credi, A., Mattersteig, G., Matthews, O. A., Montalti, M., Spencer, N., Stoddart, J. F., Venturi, M. Electrochemically induced molecular motions in pseudorotaxanes: A case of dual-mode (oxidative and reductive) dethreading. *Chem. Eur. J.* **3,** 1992–1996 (1997).

57. Balzani, V., Credi, A., Mattersteig, G., Matthews, O. A., Raymo, F. M., Stoddart, J. F., Venturi, M., White, A. J. P., Williams, D. J. Switching of pseudorotaxanes and catenanes incorporating a tetrathiafulvalene unit by redox and chemical inputs. *J. Org. Chem.* **65,** 1924–1936 (2000).

58. Leroux, Y., Lacroix, J. C., Fave, C., Trippe, G., Fe, N., Aubard, J., Hohenau, A., Krenn, J. R. Tunable Electrochemical Switch of the Nanoparticles. *ACS Nano* **2,** 728–732 (2008).

59. Ashton, P. R., Ballardini, R., Balzani, V., Gomez-Lopez, M., Lawrence, S. E., Martinez-Diaz, M. V., Montalti, M., Piersanti, A., Prodi, L., Stoddart, J. F., Williams, D. J., Hydrogen-Bonded Complexes of Aromatic Crown Ethers with (9-Anthracenyl)ammonium Derivatives. Supramolecular Photochemistry and Photophysics. pH-Controllable Supramolecular Switching. *J. Am. Chem. Soc.* **119,** 10641–10651 (1997).
60. Nam, J., Won, N., Jin, H., Chung, H. & Kim, S. pH-Induced Aggregation of Gold Nanoparticles for Photothermal Cancer Therapy. *J. Am. Chem. Soc.* **131,** 13639–13645 (2009).
61. Sharma, J., Chhabra, R., Yan, H. & Liu, Y. pH-driven conformational switch of ‘i-motif’ DNA for the reversible assembly of gold nanoparticles. *Chem. Commun.* 477–9 (2007). doi:10.1039/b612707j
62. Gittins, D. I., Bethell, D., Schiffrin, D. J. & Nichols, R. J. A nanometre-scale electronic switch consisting of a metal cluster and redox-addressable groups. *Nature* **408,** 67–69 (2000).
63. Ipe, B. I., Mahima, S. & Thomas, K. G. Light-induced modulation of self-assembly on spiropyran-capped gold nanoparticles: A potential system for the controlled release of amino acid derivatives. *J. Am. Chem. Soc.* **125,** 7174–7175 (2003).
64. Lukyanov, B. S. & Lukyanova, M. B. Spiropyrans: Synthesis, Properties, and Application. *Chem. Heterocycl. Compd.* **41,** 281–311 (2005).

CHAPTER 2: SELF-ASSEMBLED NANOSYSTEMS FOR ENANTIOSELECTIVE CATALYSIS

2.1. INTRODUCTION

The demand for atom-efficient chemical transformations with a low environmental impact makes catalyst development one of the main challenges for chemists. A wide variety of innovative approaches are being developed aimed either at a rapid identification and screening of new catalysts or at a facilitated use of established catalysts. Examples include combinatorial high-throughput screening protocols[1,2], supramolecular catalysis[3] and the use of supported homogeneous catalysts.[4] Traditional heterogeneous catalysts are rather limited in the nature of their active sites, which poses limits to the substrate selectivity of the reactions. Soluble catalysts can catalyse a much larger variety of reaction types but suffer from a higher cost (amongst others originating from a more difficult preparation and recovery). The new challenge is to merge the advantages of homogeneous and heterogeneous catalysts by matching the active site of homogeneous catalysts (providing selectivity, solubility, multivalency with a solid support.

The asymmetric catalysis of organic reactions to provide enantiomerically enriched products is of central importance to modern synthetic and pharmaceutical chemistry. Consequently, the design of novel chiral ligands is at the core of asymmetric catalysis. An important subfield in enantioselective catalysis is the construction of artificial metalloenzymes. The catalytic efficiency and high selectivities achieved by natural metalloenzymes are a continuing source of inspiration for the construction of innovative bioinspired catalysts. In the last decades, this field of catalysis oriented its attention to combine the catalytic power of transition metal catalysis with the chiral architectures of biopolymers such as proteins and DNA, with the ultimate goal of creating new catalysts that combine the best of both worlds.

Reetz et al demonstrated the power of Cu^{2+}-phthalocyanine conjugates of serum albumins as enantioselective catalysts in Diels–Alder reactions.[5] The creation of this artificial metalloenzymes involves the incorporation of a synthetic transition-metal catalyst into a human serum albumin (HSA) (Figure 2.1).

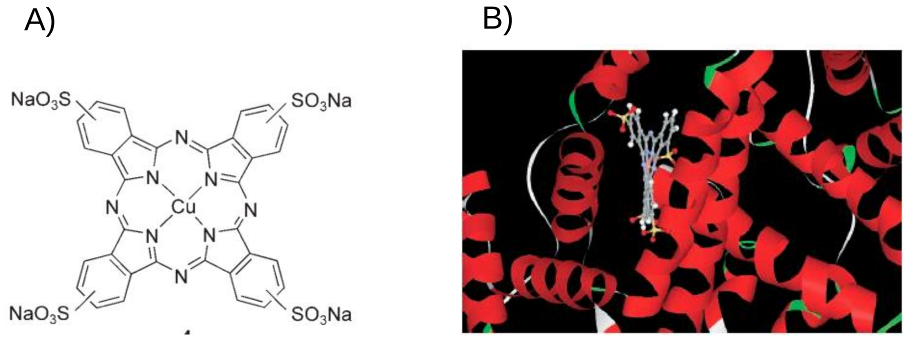

Figure 2.1. A) Achiral catalytic Cu^{2+} phthalocyanine B) Model of phthalocyanine-HSA based on X-ray crystal structure of hemin-HAS

Previous studies reported that the sodium salts of di-, tri-, and tetrasulfonic acid derivatives of porphyrins, phthalocyanines, and corroles bind strongly to serum albumins in a noncovalent manner, although the exact position of anchoring in the proteins was not elucidated with absolute certainty in all cases.[6,7,8,9,10] The reaction investigated (Scheme 1) was selected for a number of reasons: an aqueous environment is beneficial for the Diels-Alder reaction[11] and often the reaction is accompanied with large structural changes leading towards the transition state. The latter makes the Diels-Alder reaction sensitive to interactions with the biomolecular scaffold. Thanks to phthalocyanine conjugates of serum albumins the *endo/exo* ratio was 96:4 and the enantioselectivity of the major endo diastereomer was 93% *ee* with bovine serum albumin (BSA) under optimized conditions (formate buffer pH=4 using only 2 mol% of the catalyst). It was observed that the *endo* selectivity was not influenced significantly by the presence of BSA because the Cu^{2+} phthalocyanine alone leads to a 95:5 in ratio with no *ee*, so they concluded that the enantioselectivity was a result of the protein environment.

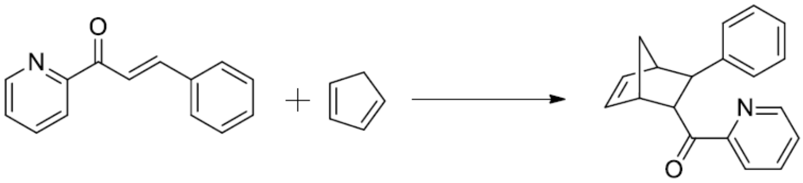

Scheme 1. Diels-Alder reaction of aza-chalcone with cyclopentadiene

Oligonucleotides have also been demonstrated to be versatile chiral scaffolds for enantioselective synthesis and catalysis. The concept of DNA-based asymmetric catalysis has been reported by Feringa, Roefles et al.[12] This involves the modular assembly of a DNA-based catalyst from natural duplex DNA, usually salmon testes DNA (st-DNA), and a copper complex of a nonchiral ligand that intercalates the DNA duplex (figure 2). As a result the catalysed reaction takes place in, or very close to, the DNA helix, which allows the chirality of DNA to be transferred to the reaction centre resulting in the enantioenriched formation of the reaction products.

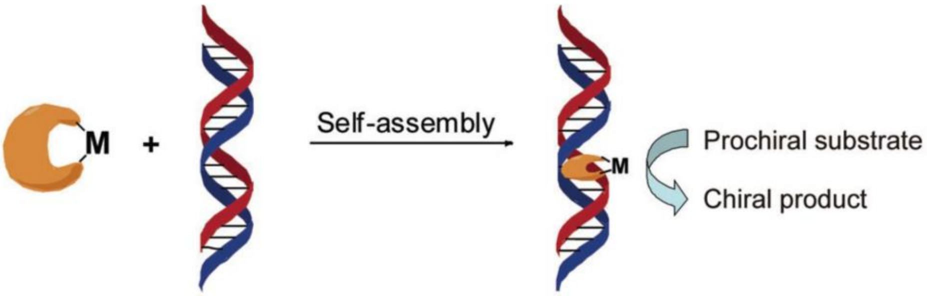

Figure 2.2. Schematic representation of DNA-based asymmetric catalysis using the supramolecular anchoring strategy

These artificial DNAzymes are generated through the propensity of small aromatic molecules to intercalate in a noncovalent, yet kinetically stable and stereoselective fashion, which enables the anchoring of metal complexes to DNA. Feringa's group reported the design of two general classes of ligand.[13] In the first generation of ligands the active site was attached via a short spacer to a metal binding moiety. In particular, the intercalator used was 9-amino acridine and aminomethyl pyridine was used as metal chelating agent. The length of the alkyl chain between the binding and the catalytic moieties was varied demonstrating that, when the catalytic site is moved away from the chiral environment, it causes a rapid decrease in enantioselectivity. This result led to the design of ligands of second generation that do not require a spacer. These ligands, that included, among others, bipyridine derivatives such as 2,2'-bipyridine (bipy) and 4,4'- dimethyl-2,2'bipyridine (dmbipy, Figure 2.3), were evaluated in the Cu^{2+} catalyzed Diels-Alder reaction of aza-chalcone with cyclopentadiene (Scheme 1). It was found that, with these second generation ligands, significantly higher *ee*'s were obtained. The *ee* could be increased even further by placing methyl groups at the 4- and 4'-positions of the bipyridine probably due alteration of the geometry of the substrate-catalyst-DNA complex by the methyl groups. In the case of dmbipy an *endo/exo* selectivity of >99:1 and an excellent *ee* of 99% for the endo isomer of the Diels Alder product was obtained.

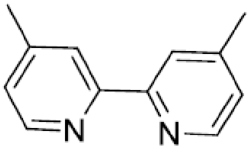

Figure 2.3. 4,4'-dimethyl-2,2'bipyridine, the best candidate of the second generation ligands

To broaden the range of reactions catalyzed by the DNA-catalytic system an alternative substrate was introduced: α,β-unsaturated 2-acyl imidazoles. Evans *et al.* had demonstrated that *α,β*-unsaturated 2-acyl imidazoles were good substrates in a variety of Lewis acid-catalyzed reactions[14] *e.g.*, Friedel-Crafts reactions, and 1,3-dipolar cycloadditions.[15]

The advantages of this class of substrates include a straightforward preparation and facile removal of the imidazole group after the catalytic reaction, allowing for further synthetic transformations. The power of the DNA-based asymmetric catalysis concept with this kind of substrates was, demonstrated in several of the archetypical C–C bond forming reactions, such as the Diels–Alder, Michael addition and Friedel–Crafts alkylation reactions (Figure 2.4).

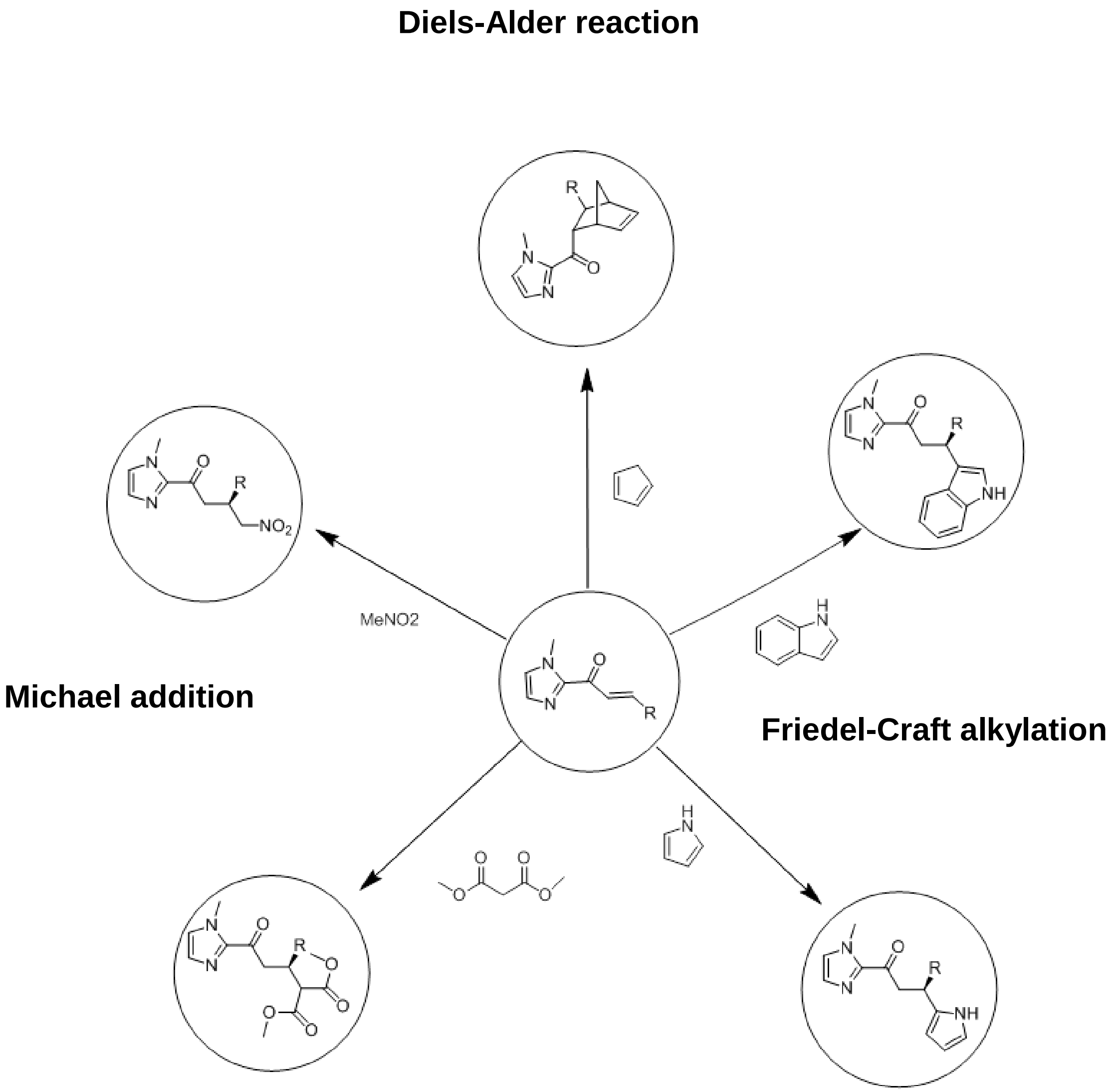

Figure 2.4. Reactions catalyzed by DNA-dmbipy based catalysis

An example of a dynamic combinatorial catalyst developed using a supramolecular approach was reported by Reek.[16] In the complex operational mechanisms of enzymes, cofactors, i.e. small molecules that influence the enzyme activity, play a dominant role in controlling chemical transformations. From this reflection, a system with an artificial transition metal catalyst that could be regulated by chiral molecules, cofactors, that are noncovalently bound to the catalytic complex has been proposed. More in detail, they used an achiral biphosphine rhodium complex, equipped with a binding site for the recognition of a chiral anion guest. Upon binding small chiral guests cofactors, the rhodium complex becomes chiral and can be used for asymmetric catalysis. For this study they used a bisphosphine ligand, which contained a diamidodiindolylmethane anion receptor, which strongly binds carboxylate anions in order to have a large library of potential chiral cofactors (Figure 2.5).

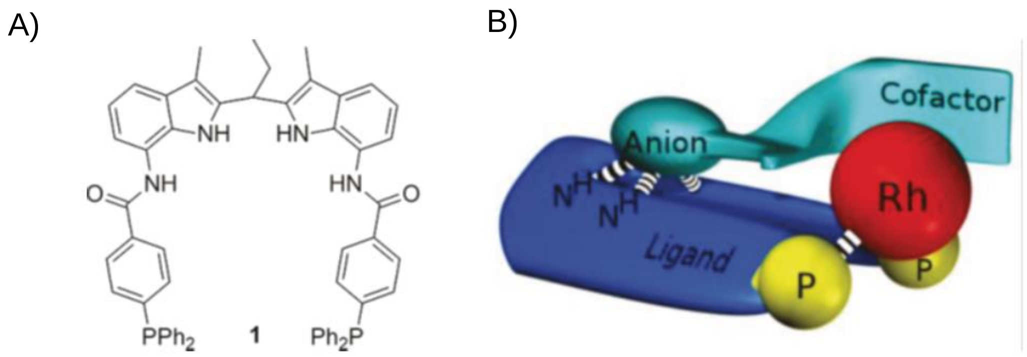

Figure 2.5. A) Structure of the ligand B) general concept of cofactor controlled enantioselective catalysis

This supramolecular catalyst was tested in the asymmetric hydrogenation of methyl 2-acetamidoacrylate. The screening of a library of cofactors revealed that the best cofactors led to hydrogenation catalysts that form the products with high enantioselectivity (*ee*'s up to 99%). Interestingly, a 'natural selection' experiment showed that the cofactor that induces the highest selectivity dominates the catalysis when applied in a mixture of 12 different cofactors.

2.2. CONCEPT

The main aim of the project is to create a new hybrid dynamic catalytic system for the stereoselective catalysis of organic reactions such as Diels-Alder, Michael addition and Friedel-Craft alkylation. It is well established that a self-assembled monolayer (SAM) can play a crucial role in determining the catalytic properties of an embedded catalyst.[17] In mixed monolayers, thiols surrounding the catalyst can affect its efficiency and selectivity. Indeed, embedding the catalyst within the SAM rather than at the periphery may create an enzyme-like catalytic cleft, which may affect substrate orientation and thus, the selectivity of product formation. Starting from this premise, three thiols equipped with the metal active site with different chain lengths will be synthetized and their activities investigated (Figure 2.6).

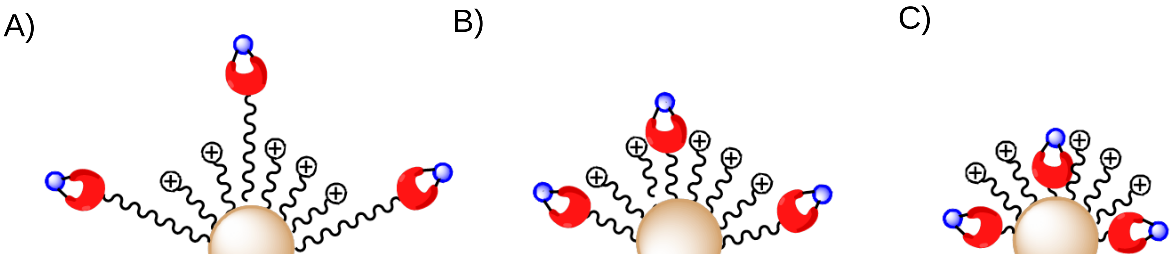

Figure. 2.6. Schematic representation of three different SAM in presence of mixed monolayer gold nanoparticles (MMAuMPCs) A) Metal active site positioned above the monolayer B) Metal active site positioned even the monolayer C) Active site embedded in the monolayer

The final aim is to induce asymmetric catalysis by creating a chiral space through the self-assembly of chiral entities (such as peptides) on the surface of monolayer protected gold nanoparticles, which would, then, transfer the chirality to the catalytic centres embedded in the monolayer. The particular challenge is to use the monolayer to alter and fine tune the catalytic properties of the system. The system should combine the power of artificial metalloenzymes and the possibility to achieve stereoselectivity by dynamic transfer of conformational chirality. Previous studies in the Prins' group have shown that the cationic surface of Au NP functionalized with 8-trimethylammonium-octanethiol (Thiol **1**) can bind quantitatively oligoanions even at low μM concentrations in water. Thus, negative charged peptides will be synthetized and self-assembled on the surface to create a chiral environment. The ability of the resulting nanosystem to induce enantioselectivity in the target reaction has been investigated (Figure 2.7).

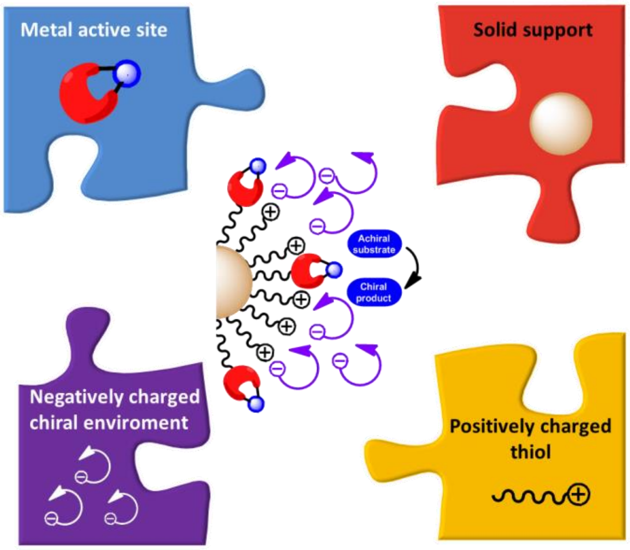

Figure 2.7. General representation of covalent linked catalytic system

2.3. RESULTS AND DISCUSSION

2.3.1. Ligand design

The 8-trimethylammonium-octanethiol (Thiol **1**) was used to form a self-assembled monolayer on Au NP **I**. This thiol was used to prepare three different self-assembled mixed-monolayers (SAM) that also contain the presence of a metal binding moiety. Three thiols **5a-c** with different chain length equipped with the dmbipy ligand were synthesized. In a previous work[13], dimethylbipyridine (dmbipy) was selected as optimal ligand for the Cu^{2+}-catalyzed Diels-Alder reaction of aza-chalcone with cyclopentadiene as well as in several of the archetypical C–C bond forming reactions, such as Michael addition and Friedel–Crafts.[18]

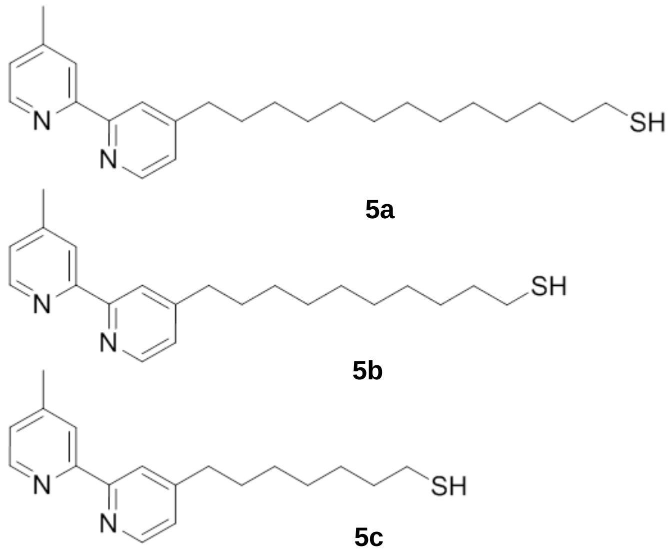

Figure 2.9. Chemical structures of thiol 5a, 5b, 5c

The synthesis was carried out following a reported procedure.[19,20]

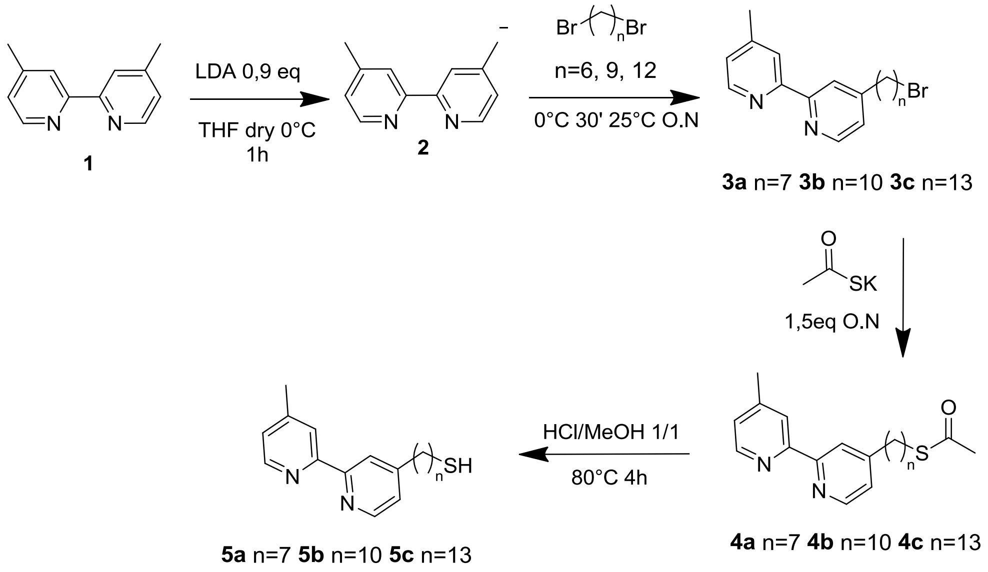

Scheme 2. Schematic synthesis of 5a, 5b, 5c

2.3.2. Synthesis of the catalytic systems

The synthesis of Au NP **I** was carried out using a protocol reported by Peng *et al*[21] and Scrimin *et al*[22]. In the first step, an aqueous solution of Au(III) ions (yellow) is transferred to a toluene solution using tetraoctylammonium bromide (TOABr) as phase-transfer agent. Then, dioctylamine is added and a colourless solution obtained. The addition of sodium borohydride promotes the final reduction to gold (dark solution). Lastly, by adding a solution containing the desired thiols stable nanoparticles are obtained. Dioctylamine is used as an intermediate stabilizing agent and its concentration controls the size of the nanoparticles. Also, the weak Au-N interaction permits formation of the final thiol protected gold clusters under very mild conditions, which are compatible with most biomolecules and other water soluble compounds. The Au NP **I** were synthetized following this procedure and characterized by ^{1}H-NMR, TEM, TGA, DLS. These techniques provide information about the dimensions of the nanoparticles, in particular the distributions profile is given by TEM (1.2 ± 0.31 nm), and the hydrodynamic radius (6,8 nm), including the layer of surfactant and the associated solvation shell is provided by DLS. ^{1}H-NMR give us information about the composition of monolayer and and TGA about the surface ligand coverage of gold nanoparticles, providing the Au/S ratio (% weight loss = 49,48% corrisponding to Au/S = 127/99).

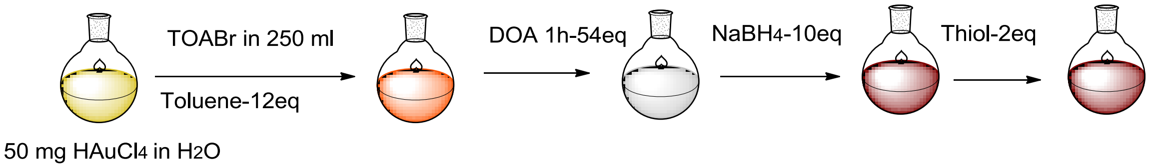

Figure 2.8. Schematic representation of AuNPs synthesis. DOA= dioctylamine, TOABr=Tetraoctylammonium bromide (all the equivalent refer to the startin $HAuCl_4$)

Exchange protocols in which a new thiolate ligand is incorporated into a monolayer by displacing the existing thiol leads to monolayers comprising a mixture of thiols.[23] Thus, starting from Au NP **I**, mixed monolayer gold nanoparticles using thiols **5a** (Au NP **II**), **5b** (Au NP **III**), **5c** (Au NP **IV**) were synthetized by ligand place exchange reactions (Figure 2.9).

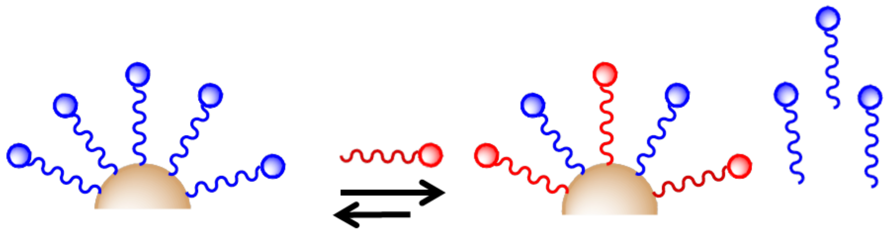

.

Figure 2.9. Thiols place-exchange mechanism

Place-exchange mechanism leads to monolayers comprising a mixture of thiols with a composition that, sometimes, can be difficult to control. The thermodynamics that govern mixed monolayer formation are complex, but generally reflect the relative solubilities of the components in solution as well as chain-chain interactions in the monolayer. Indeed, several parameters are involved in the reaction, such as the time of exchange between thiols, the solvents used and the ratio between ligands already present on the surface and the entering thiols free in solution. Thus, the optimization of these parameters led, finally, to the catalytic systems Au NP **III** (mixed monolayer between Thiol **1** and **5b**) and **IV** (Thiol **1** and **5c**). In the case of Au NP **III** the optimized parameters were an exchange time of 1.5 h, a ratio of free thiol **5b**/headgroup = 0.5/1 and a solvent system composed of EtOH/H_2O=2/1.

The Au NP were characterized by ^{1}H-NMR and by using “longitudinal-eddy-current-delay (LED) pulse sequence[24] (diff-on ^{1}H-NMR) that permits to differentiate molecules based in their diffusion coefficients. This provides an equivocal proof that thiols are bound to the AuNP surface (broad signals) as well as a way to assess the purity of the samples. Diffusion filter ^{1}H-NMR experiments[24] (diff-on ^{1}H-NMR) in D_2O, hence, allowed us to identify the peaks related to the thiol **5b** embedded in the monolayer. Six peaks, that are characteristic of the aromatic proton of the bipyridine, were identified (Figure 2.10 encircled in blue). Compared to the ^{1}H-NMR spectrum of the free thiol, that presents three characteristic signals, the dmbipy constrained in the monolayer had lost its symmetry owing to the asymmetric alignment with respect to the neighbouring thiols. Furthermore, the singlet in the ^{1}H-NMR spectrum originating from the methyl group attached in position 4 of the bipyridine was identified.

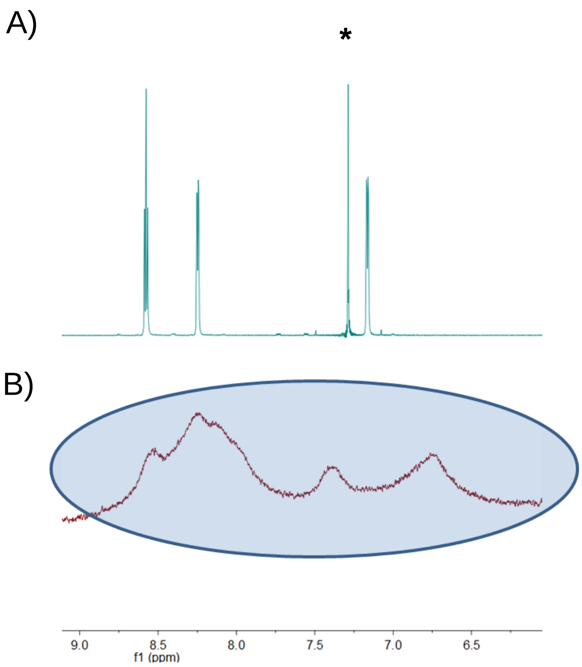

Figure 2.10. Zoom of ^{1}H-NMR of a) thiol **5b** b) Au NP **III. ***peak of the solvent

Au NP **IV** was synthesized with a slightly different protocol compared to Au NP **III** (6 h of exchange, ratio free thiol **5c**/headgroup 0.8/1 carried out in EtOH/H_2O 1/1). In the ^{1}H-NMR spectrum there are, now, three broad signals in the aromatic region, which are comparable with those of the free thiol. In Figure 2.11 is reported the comparison between ^{1}H-NMR of Au NP **III** and Au NP **IV** and a clear difference can be observed. The environment in which the dmbipy moiety is embedded could explain this difference. In the case of Au NP **IV**, the dmbipy ligands extend out of the monolayer because of the longer alkylchain present in thiol **5c** compared to thiol **1**. This might explain why the ligands' NMR signals do not show signs of desymmetrization.

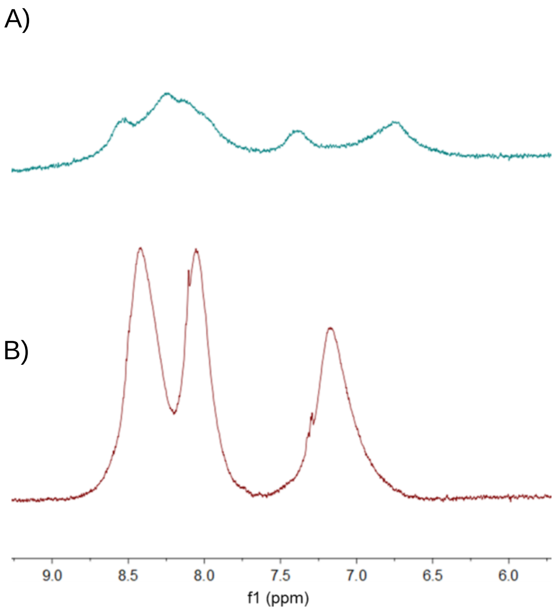

Figure 2.11. Zoom of ^{1}H-NMR of a) Au NP **III** b) Au NP **IV**

Both Au NP **III** and Au NP **IV** were characterized by TEM, DLS, TGA (see experimental section) providing respectively a diameter of 1 and 1,1 nm, an hydrodynamic radius of 8,6 and 4,6 nm and a % of weight loss of 43,10% and 63,06%.

Regrettably, the synthesis of Au NP **II** could not be achieved because the instability of the system after exchange resulted in all cases in the formation of insoluble clusters.

2.3.3. Quantification of 4-methyl-2,2'bipyridine-alkylthiols in mixed monolayers

Taking into account that the mechanism of place-exchange does not permit a perfect control of the composition of the mixed monolayer, the quantification of the 4,4'-dimethyl-2,2'-bipyridine linked to the surface was the first challenge to be dealt with. The quantification was performed using UV-vis spectroscopy, taking advantage of the shift in absorption when bipyridine is forming a complex with Cu^{2+} (Figure 2.12 A). To validate the method, the titration of Cu^{2+} on free dmbipy was carried out first.

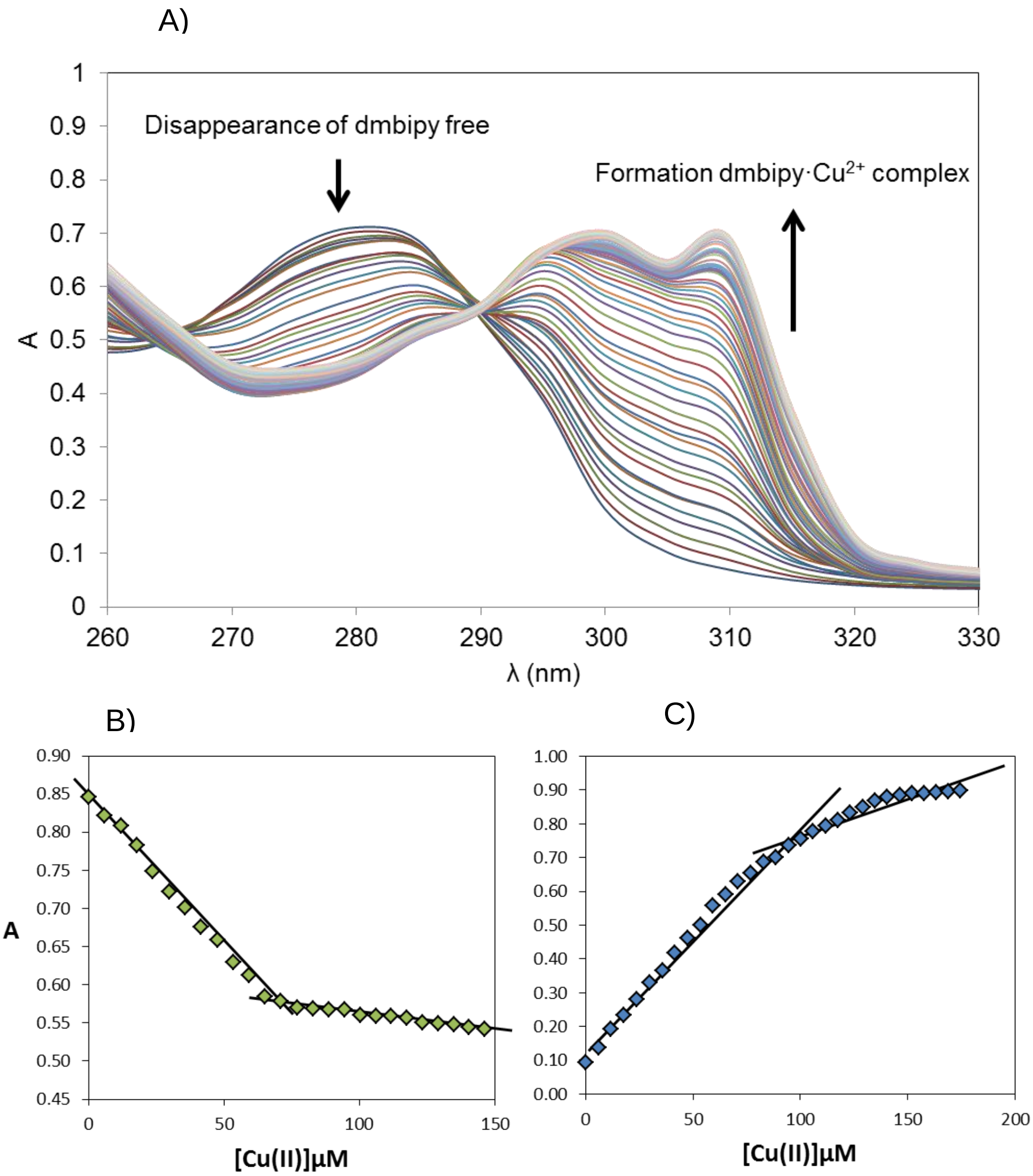

Figure 2.12. A) UV Absorption of dmbipy free at different concentration of Cu^{2+} B) Absorption as function of [Cu^{2+}] at 280 nm C) Absorption as function of [Cu^{2+}] at 310 nm

The titration of Cu^{2+} to dmbipy causes significant changes in the UV-spectrum, but is characterized by an isosbestic point at 290 nm (Figure 2.12 A). The absorption at 280 nm (maximum of free dmbipy) and 310 nm (maximum of the dmbipy-Cu^{2+} complex was plotted as function of the amount of Cu^{2+} (figure 2.12 B-C). Given that the complex forms under saturation conditions, from the intersection of the two straight lines it was possible to calculate the concentration of dmbipy The average calculated concentration (70 μM) of dmbipy compared well to the known concentration of dmbipy (65 μM, obtained by weight measurements), which validated the method. When the ligand is present in the mixed monolayer of Au NP **III** and **IV,** the isosbestic point is still present, although less evident. The titration of Cu^{2+} on the surface of the Au NP was carried out and the changes in absorption at 280 nm (ʎ maximum of free ligand) and 310 nm (ʎ maximum of the complex) as a function of the concentration of Cu^{2+} allowed a quantification of the concentration of catalytic sites on the cluster (Figure 2.13).

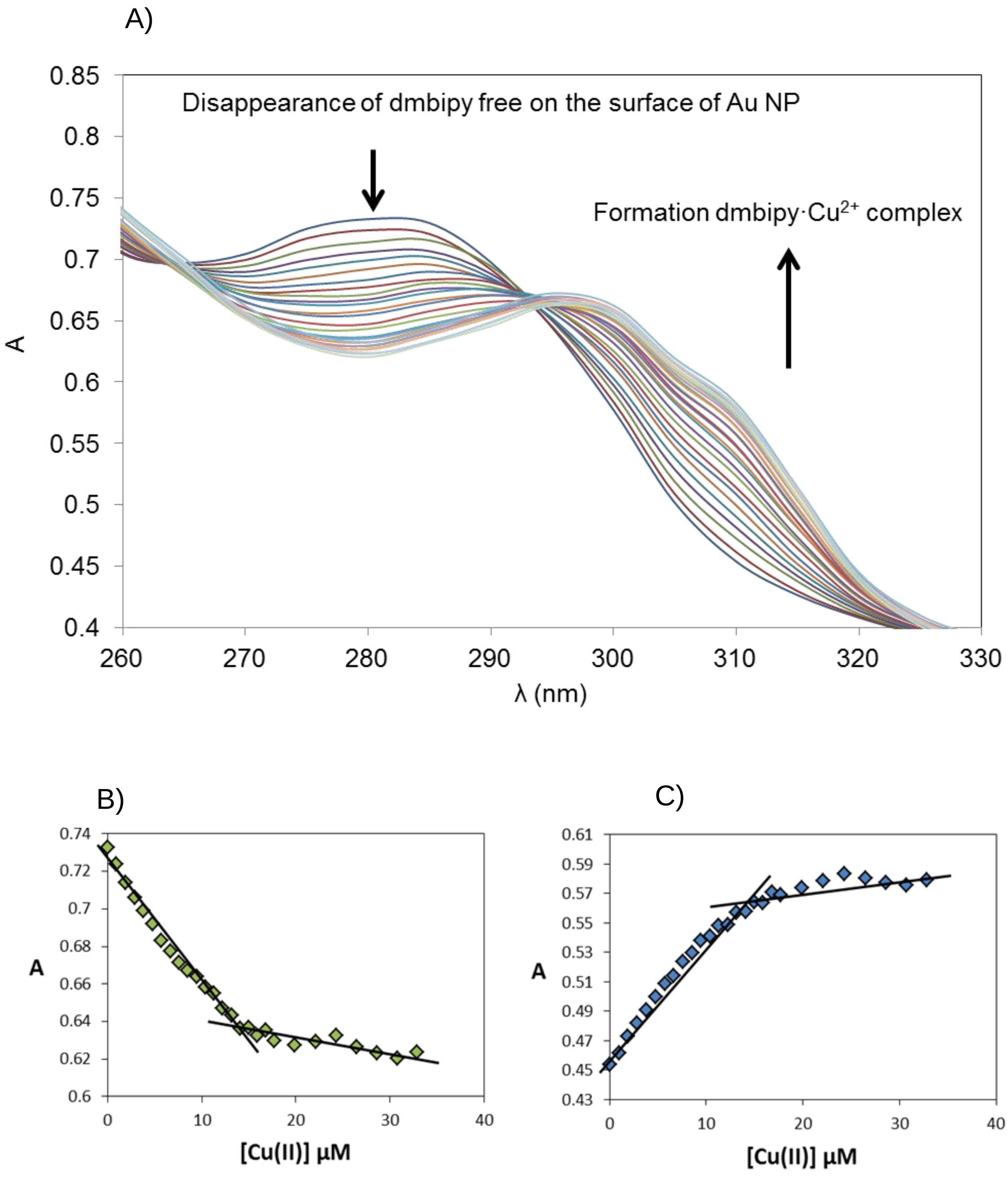

Figure 2.13. A) UV spectrum of Au NP **III** at increasing amount of Cu^{2+} B) Absorbance as function of [Cu^{2+}] at 280 nm C) Absorbance as function of [Cu^{2+}] at 310 nm

The profiles indicated the quantitative formation of the complex and showed an average concentration of dmbipy moiety in solution about 15 μM. The same procedure was followed for Au NP **IV** (See Figure S11).

2.3.4. Reaction under investigation

The reaction taken as model for the investigation of catalytic activity of the AuNP was the Diels-Alder reaction between 2-cinnamoyl-1-methyl-1*H*-imidazole **10** and cyclopentadiene. Recently, *α,β*-unsaturated-1-acyl-3,5-dimethylpyrazoles were reported as substrates for the catalytic Diels-Alder reaction leading to generally good yields and enantioselectivities.[25]

Evans et al had demonstrated that α,β-unsaturated 2-acyl imidazoles were good substrates in a variety of Lewis acid-catalyzed reactions, e.g.,Friedel-Crafts reactions, 1,3-dipolar cycloadditions.[15] The advantages of this class of substrates include a straightforward preparation and facile removal of the imidazole group after the catalytic reaction, allowing for further synthetic transformations. Roelfes et al.[18] confirmed the applicability of this substrate in the catalysis with dmbipy hybrid complexes in most of organic reactions. The synthesis of the dienophile was achieved following reported protocols (Scheme 3).

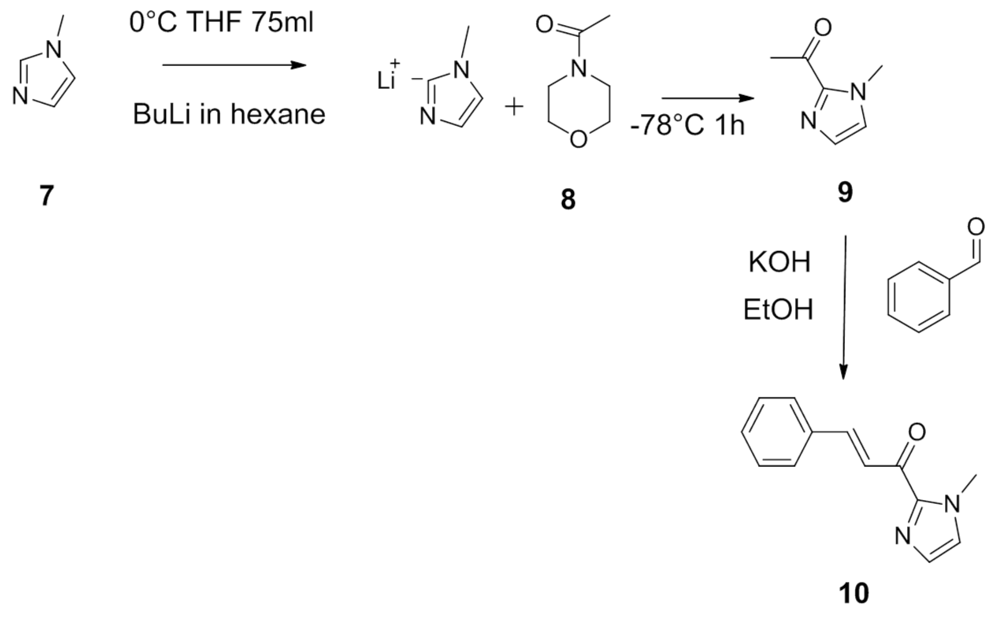

Scheme 3. Schematic synthesis of α,β-unsaturated 2-acyl imidazoles

The ^{1}H-NMR spectrum of the *α,β*-unsaturated 2-acyl imidazole **10** confirmed the reproducibility of the reaction reported in literature. Cyclopentadiene was used as diene in the Diels-Alder reaction. At room temperature, this cyclic diene dimerizes over the course of hours to give dicyclopentadiene via a Diels–Alder reaction. This dimer can be restored by heating at boiling point to give the monomer and collecting the lower boiling cyclopentadiene using a fractionating column. The distilled monomer was analyzed by ^{1}H-NMR to confirm the purity.

2.3.5. Catalysis

2.3.5.1. Influence of the monolayer on the activity and selectivity of the catalyst

The effect of the bipyridine moiety anchored to Au NP **III** and **IV** on the Lewis-acid- catalyzed Diels-Alder reaction of substituted *α,β*-unsaturated 2-acyl imidazole **10** with cyclopentadiene was investigated in water (Figure 2.14).

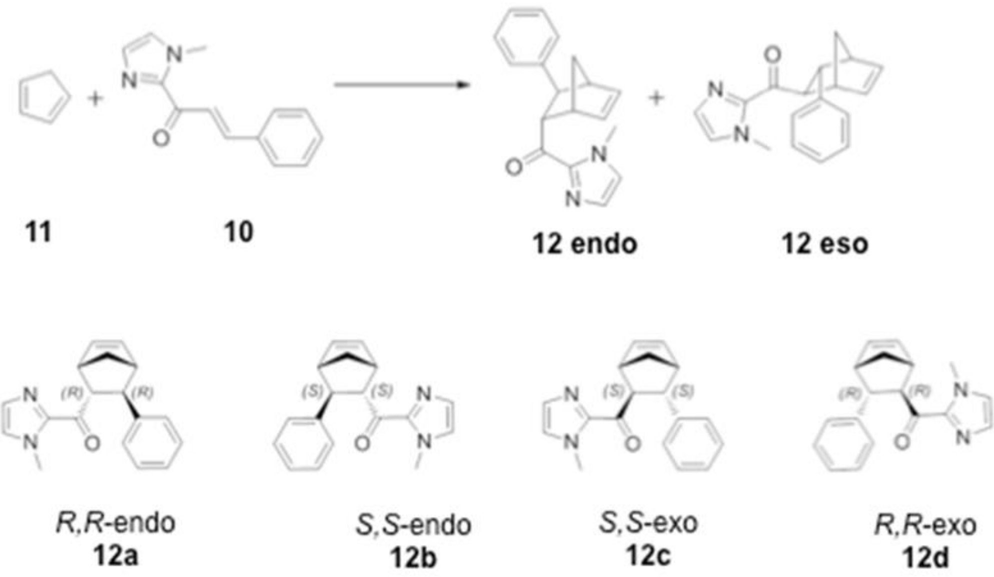

Figure 2.14. Four isomers of compound **12**.

The reaction produces four different products: (*R,R*)- and (*S,S*)- endo-**12** (**12 a** and **12 b**) as well as (*S,S*)- and (*R,R*)-exo-**12** (**12c** and **12d**). This is of interest because it enables the assessment of the influence of ligands on the *endo-exo* ratio of **12** as well as on the enantioselectivity in case chiral elements are introduced.

The ability of the system to catalyze the reaction was evaluated in a first experiment in which the reaction was performed in the presence of 5% mol of catalyst (0.1 mM catalyst referring to dmbipy, 2 mM dienophile, 16 mM diene, MES pH 6.5 20 mM) at r.t. for 5 days as reported in the literature.[18] The products were analyzed by HPLC using a chiral column functionalized with tris-(3,5 dimethylphenylcarbamate) in a gradient of hexane/isopropanol. The catalytic activity of Au NP **III** and Au NP **IV** was compared to the activity of the complex dmbipy-Cu^{2+} (at the same concentration) in solution (considered as blank) and with the activity of the same complex in the presence of Au NP **I**, containing just ammonium head groups (at the same NP concentration). As can be observed in Figure 2.15 A and B, for both control experiments identical ratios of *endo* (major diastereoisomers at 8.1 and 9.3 mins) and *exo*-products were formed (*endo ratio* 49/51, *eso 48/52)*. (minor diastereoisomers at 6.7 and 7.8

mins). Besides, both diastereoisomers were formed as racemates. All peaks were assigned based on literature.[26]

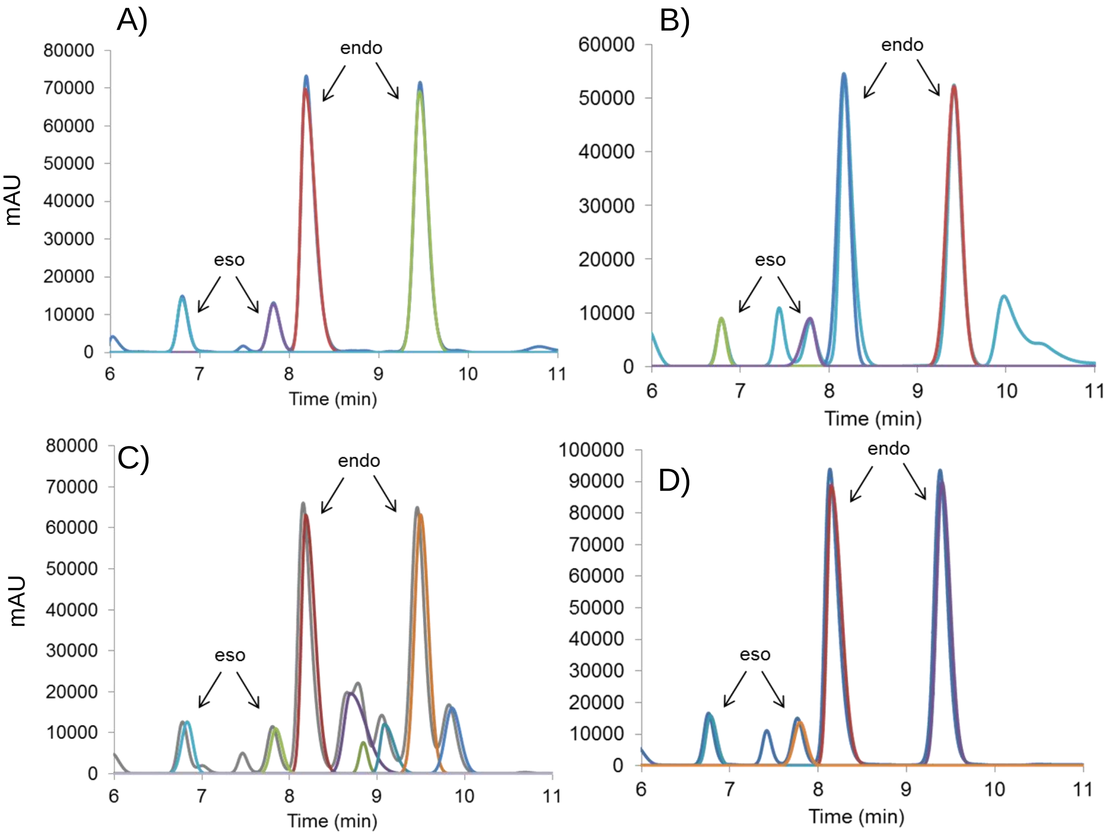

Figure 2.15. HPLC chiral chromatograms measured by DP-HPLC. Conditions: 2,5%-5% B in 20 minutes; A: hexane, B: isopropanol of the reaction catalyzed by A) the complex formed by dmbipyand Cu^{2+} free in solution B) AuNPs **I** and dmbipy Cu^{2+} complex C) Au NP **III** D) Au NP **IV**

The chromatogram of the reaction performed in the presence of Au NP **III** indicates the formation of additional products. In particular two peaks at 8.6 and 9.8 minutes were detected corresponding to significant concentrations (Figure 2.15 C). Unfortunately, it has not been possible to characterize these, because the impossibility to separate and collect significant amounts of product. These additional peaks suggest a different reactivity and selectivity of the substrates owing to steric interactions between the alkyl chains and the catalysts when the catalyst is levelled with the monolayer surface. On the contrary, when Au NP **IV** is the catalyst no additional products are observed and the chromatogram is nearly identical to the one obtained for the catalyst free in solution (Figure 2.15

A and 2.15 D). This is probably due to the fact that the catalyst extends out of the SAM (**5b** extends of two methylene groups compared to Thiol **1**), behaves most closely as a homogenously solubilized catalyst.

The monolayer may also affect the diastereoselectivity of the reaction, by enforcing a different geometry of the complex formed by ligand, copper (II) and dienophile. Comparison of the results obtained for Au NP **III** and the complex dmbipy-Cu^{2+} show slight differences in diastereoselectivity in favour of the *endo* products (80,3% *vs* 89,9% respectively) (Figure 2.16). For Au NP **IV** no differences were observed compared to the control. Although present, this effect is not significant (less than 1%), indeed also the control presented the same high ratio.

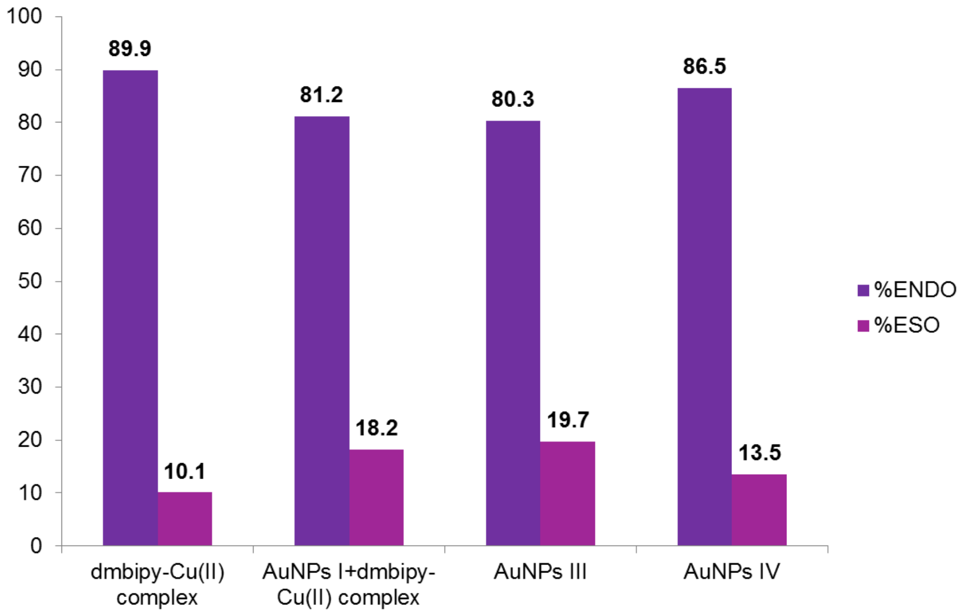

Figure 2.16. Diastereoselectivity (%) of the four different catalytic systems: **1.** Dmbipy-Cu^{2+} complex **2.** AuNPs **I** and Dmbipy-Cu^{2+}complex **3.** Au NP **III** **4.** Au NP **IV**

2.3.5.2. Enantioselective catalysis

Encouraged by the fact that catalytic activity was observed, we then proceeded with the creation of an enantioselective catalytic system (Figure 2.17). In order to create a chiral catalytic site, the self-assembly of negatively charged chiral peptides onto the positively charged monolayer of Au NP **IV** was investigated. Au NP **IV** was chosen because it was anticipated that the catalytic center (extending out of the monolayer) would have a higher chance of being sensitive to the presence of neighbouring chiral peptides assembled on the monolayer.

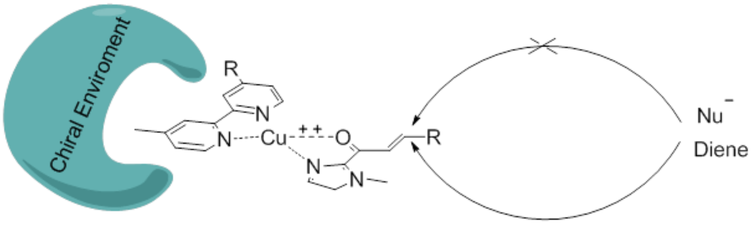

Figure 2.17. Enantioselective schematic system

The first peptide tested was **P3** (Figure 2.18) composed of a phospho-Ser as negatively charged unit for binding to cationic monolayers as well as a L-Trp-residue as fluorescent unit to detect binding and two L-Leu residues to provide the chiral environment. Its behaviour is well studied in our group and it is known that P3 has a high affinity for AuNP **I**. The surface saturation concentration (SSC) of peptide P3 bound to Au NP 1 is obtained from a fluorescence titration of the peptide to AuNP **I**, taking advantage of the ability of of gold nanoparticles to quench the fluorescence of bound fluorophores[27]

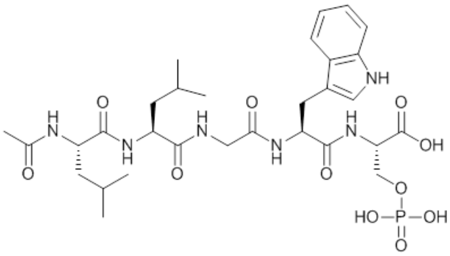

Figure 2.18. Chemical structure of Ac-(LLLL)-Leu-Leu-Gly-Trp-Ser(PO_3H_2)-**P3**

The binding experiments were performed in the same conditions used in the catalysis experiments conditions (0.1 mM of dmbipy-Cu^{2+} complex as head group, 20 mM MES, pH 6.5). The results indicated that **P3** has a surface saturation concentration (SSC) of about 40 μM for 100 μM of dmbipy-head group in the absence of copper(II), and about 60 μM in the presence of Cu^{2+}.

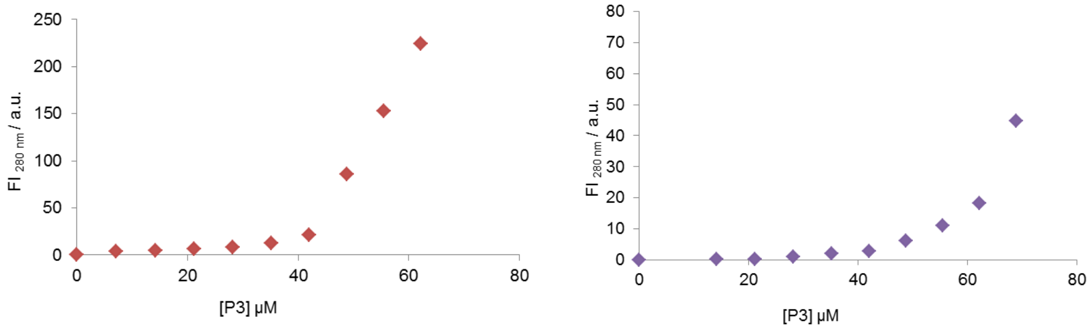

Figure 2.19. Determination of the fluorophore SSC. Fluorescence intensity as a function of the amount of **P3** added to A) a solution of AuNP **IV** [dmbipipy] = 100 µM and B) a solution of AuNP **IV** [dmbipipy] = 100 µM and [Cu^{2+}] = 100 µM. Conditions: [MES] = 30 mM, pH 6.5, 25 °C, λ_{ex} = 280 nm, λ_{em} = 360 nm

After having confirmed the high affinity of **P3** for Au NP **IV**, we then proceeded by testing the catalytic activity of Au NP **IV** in the presence of peptide **P3**. The reactions were carried out adding **P3** to the reaction solution containing the Au NP **IV**-Cu^{2+} complexes. In order to avoid the possible binding of negative charged **P3** to Cu^{2+} a concentration lower than the surface saturation concentration was used leaving the surface partially free for catalysis. The reactions were performed with both 20 µM and 40 µM of **P3**. After 5 days the reaction was analyzed by HPLC. The resulting chromatograms are given in Figure 2.20.

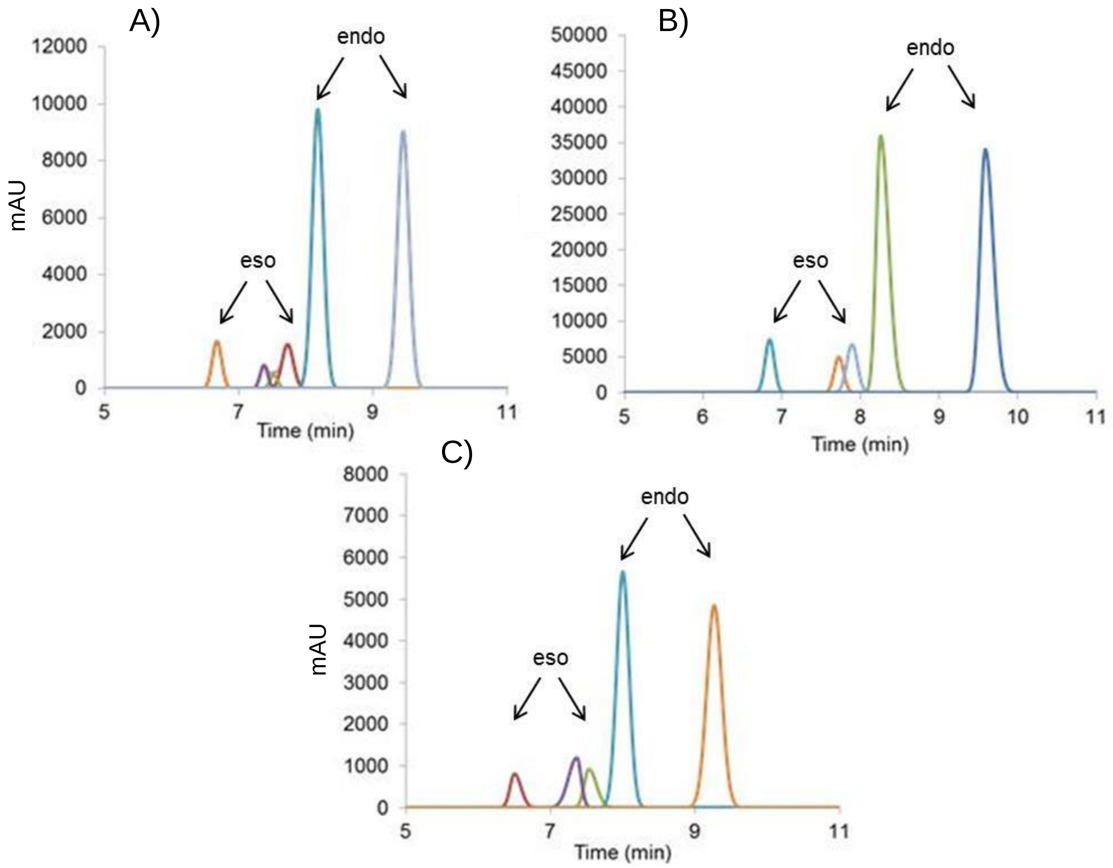

Figure 2.20. HPLC chiral chromatograms of the reaction in A) the absence of **P3** B) in the presence of 20μM of **P3** C) in the presence of 40 μM of **P3** measured by DP-HPLC. Conditions: 2.5%-5% B in 20 minutes; A: hexane, B: isopropanol. Reaction condition: [dmbipy·Cu^{2+}] = 0.1mM, [MES] = 30 mM, pH 6.5, [**10**] = 2 mM [**11**] = 16 mM, 5 days, 25 °C.

As in the previous experiments, the four diastereomers were clearly present, two *exo* isomers at 6.6 and 7.7 minutes and two *endo* isomers at 8.4 and 9.4 minutes. A first glance at the chromatograms (in particular Figure 2.20 C) reveals immediately that, the relative area of the peaks belonging to the enantiomers of the exo and endo isomers has changed. The *ee* % were calculated and plotted in Figure 2.21.

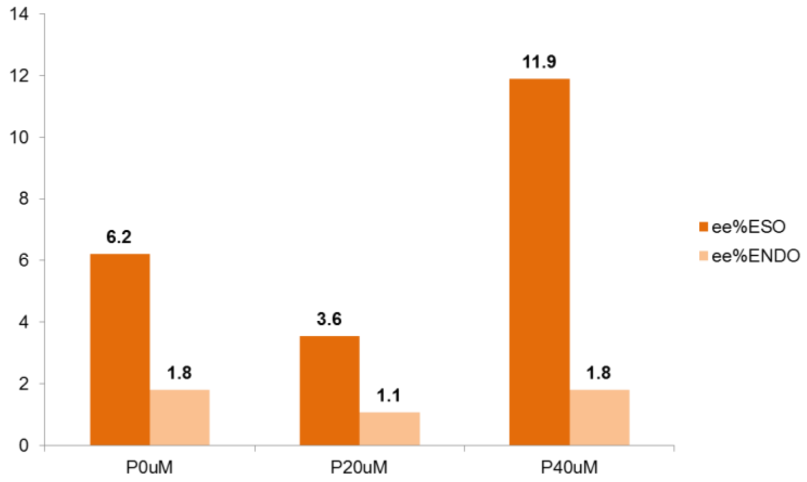

Figure 2.21. % Enantioselectivity of the three different catalytic systems: A**)** Au NP **IV,** no **P3**. B**)** Au NP **IV, P3** 20 µM. C) Au NP **IV, P3** 40 µM

These results are quite promising as they suggest that **P3** induces an enantioselectivity, which is twofold higher than the reaction performed in the absence of peptide (the large errors originate from the difficult to perform accurate integrations). However, the observed *ee* were rather modest. The cause could be the low surface coverage of the catalyst with **P3**. In fact, the concentration of peptide compared to that of dmbipy head groups is 20% or 40%, respectively, but this percentage drops drastically if we compare this concentration to the concentration of positively charged head groups present on nanoparticles (both dmbipy-Cu^{2+} complex ligand and 8-trimethylammonium-octanethiol). From this point of view the observed *ee* could be considered an encouraging result. Finally, the last issue which is worth to be pointed out, is the overall low yield of the reaction. Indeed, typical yields of around 5 and 10 % were obtained after 5 days. It is well known[28] that, in artificial metallo-enzymes, the choice of the correct bioscaffold permits both the achievement of high *ee* and a rate enhancement of the reaction. However it seems that the presence of an apolar pocket seems to be a key requirement to achieve this. The absence of such a pocket in our system may be the reason for the fact that rate acceleration is not observed.

2.4. CONCLUSION

The synthesis and the characterization of mixed monolayer Au NP containing dmbipy·Cu^{2+} metal complex as functional head groups has been reported. Their ability to catalyze the Diels-Alder reaction between 2-cinnamoyl-1-methyl-1H-imidazole and cyclopentadiene in water has been demonstrated. This system was then turned into a chiral nanocatalyst by assembling a chiral peptide on the monolayer surface.

Although the fact that an *ee* is observed is promising, the actual value is very modest. The concentration of peptide bound to the surface that can be achieved in these conditions probably is too low to create an chiral environment able to envelop the catalyst and induce high enantioselectivities.

Furthermore, the maximum concentration of dmbipy head group that could be introduced in the system without compromising the stability and solubility of the system is rather low (5-10%). This entails that the amount of nanoparticles needed for the catalysis is considerable and that, in this way, the advantages of using the catalyst are lost.

Moreover, our impression is that the nanoparticles, due to their spherical shape, do not allow the formation of an apolar pocket that it is usually generated by bioscaffold and this prevents significant rate accelerations.

Indeed, the most important point of reflection, as focused before, are the low yields of the reaction. The attainment of small amount of products complicates the study of the system (*i.e*. the calculation of the diastereoselectivity) as well as the easy employment of most of the analytical techniques and makes the work up of the sample after the reaction critical.

2.5. EXPERIMENTAL SECTION

2.5.1. Instrumentation

NMR Analysis

^{1}H-NMR and ^{13}C-NMR spectra were recorded using a Bruker spectrometer operating 500 MHz for ^{1}H. Chemical shifts (δ) are reported in ppm using $CDCl_3$ residual solvent value as internal reference.[29] Diffusion-ordered ^{1}H-NMR spectra were recorded using the"longitudinal-eddy-current delay" (LED) pulse sequence.[24]

TEM Analysis

TEM images were recorded on a JEol 300 PX electron microscope. One drop of sample was placed on the sample grid and the solvent evaporated. TEM images were elaborated using the software ImageJ (http:// rsb.info.nih.gov/ij/).

DLS Analysis

Dynamic light scattering measurement were recorded on a Zetasizer Nano-S (Malvern Malvern, Worcestershire, UK) equipped with a thermostatted cell holder and Ar laser operating at 633 nm.

TGA Analysis

Thermogravimetric analysis (TGA) was run on ½ mg of nanoparticles samples using a Q5000 IR model TA instrument from 30 to 1000°C under continuous air flow.

pH measurements

The pH of buffer solutions was determined at room temperature using a pH-meter Metrohm-632 equipped with a Ag/AgCl/KCl reference electrode.

UV-Vis and Fluorescence spectroscopy

Uv-Vis measurements were recorded on a Varian Cary50 spectrophotometer, while Fluorescent measurements were recorded on a Varian Cary Eclipse

Fluorescence spectrophotometer. Both spectrophotometers were equipped with a thermostatted cell holder.

HPLC Analysis

HPLC purifications were performed on a preparative HPLC Shimadzu LC-8A equipped with a Shimadzu SPD-20A UV detector. The column used for the separation was Jupiter Proteo 4u 90A 250 x 21.20, 4 µm. All the runs were carried out using a flow of 17 mL/min. Eluents: H_2O(A) / and ACN (B) +0.1% TFA.

The chiral products were analyzed by NP-HPLC Shimadzu LC-10AT equipped with a Simadzu SPD-10A UV detector. The separation was carried out using a chiral column (Lux 5µ Cellulose-1) functionalized with cellulose tris(3,5-dimethylphenylcarbamate) in a gradient of hexane/isopropanol.

The deconvolution of the peaks was carried out using the freeware software Fityk.

ESI-MS Analysis

ESI-MS measurements were performed on an Agilent Technologies 1100 Series LC/MSD Trap-SL spectrometer equipped with an ESI source, hexapole filter and ionic trap.

2.5.2. Materials

4,4’-Dimethyl-2,2’-bipyridine, LDA, 1,9-dibromononane, 1,6-dibromohexane, 1,12-dibromododecane, 1,8-dibromoctane, trimethylammine ethanol solution, potassium thioacetate were purchased from Sigma Aldrich. $Cu(NO_3)_2$ was an analytical grade product. Stock solutions were prepared using deionized water filtered with MilliQ-water-purified (Millipore) and stored at 4 °C.

2.5.3. Synthesis of compounds 5a, 5b and 5c

General procedure. The treatment of 0.840g (4.6 mmol) 4,4’-dimethyl-2,2’-bipyridine (**1**) dissolved in 25mL of THF with 0.9 equivalent of LDA in THF (2,1 mL of a solution 2M), at 0°C for one hour afforded the dark orange-red mono-lithium compound. The addition of 1 eq of the respective alkyl dibromide (1,9-dibromononane, 1,6-dibromohexane, 1,12-dibromododecane) to the carbanion species yielded the crude product. Products **3a, 3b** and **3c** were obtained with RP-HPLC H_2O/ACN (gradient 5%-95% of ACN in 30’). Potassium thioacetate (1.5 eq) was added to a solution of products **3a-c** dissolved in 50 ml of acetone and stirred overnight. After filtration product **4** was purified by column chromatography on silica (DCM/MeOH = 95/5). The treatment of **4** with a solution of HCl 6N/EtOH = 1/1 at 80°C gave the pure products **5a-c.** 102.3 mg of **5a** was obtained as dark red solid (90 mg, yield = 5%). **5b** was obtained as pink solid (235,7 mg, yield= 15%) and **5c** was obtained as pink solid (108 mg, yield = 7,4%).

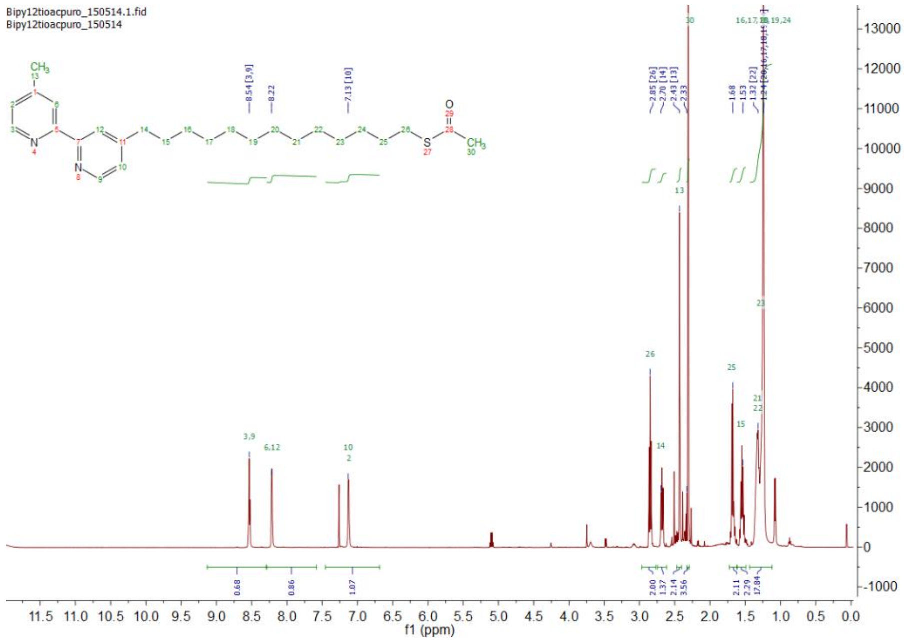

Figure S1. ^{1}H-NMR spectra of **4a** in $CDCl_{3,}$ ($CDCl_3$, 500 MHz, 298K)

4a **^{1}H-NMR**: ($CDCl_3$, 500 MHz), δ: 8.54 (t, 2H), 8.22 (d, 2H), 7.13 (t, 2H), 2.85 (t, 2H), 2.70 (t, 2H), 2.43 (s, 3H), 2.33 (s, 3H), 1.68 (quint, 2H), 1.53 (quint, 2H), 1.24 (broad, 22H)

MS (ESI,+,MeOH): *m/z* [M+H$^+$], 427.2, calc. 427.27

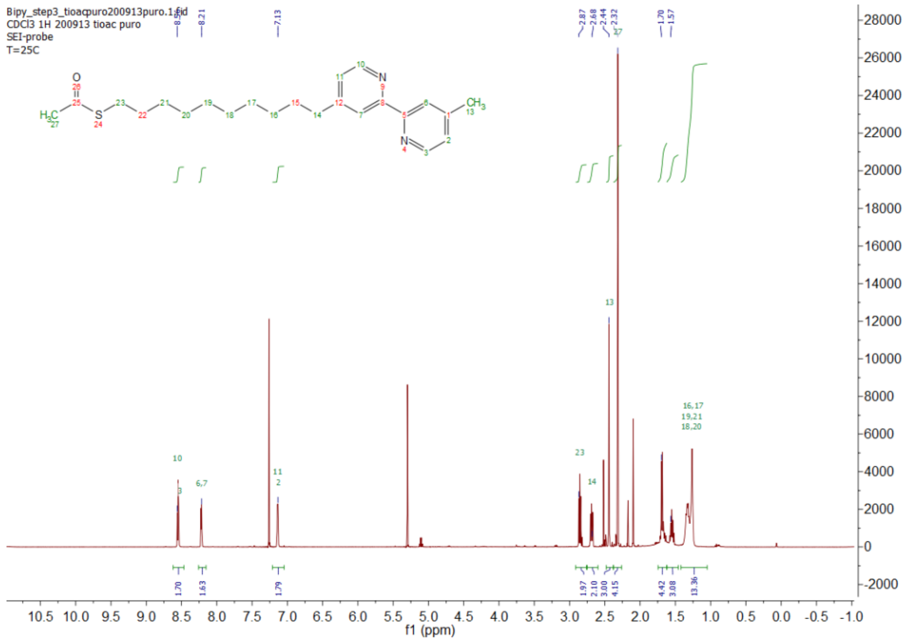

Figure S2. ^{1}H-NMR spectra of **4a in** $CDCl_3$, ($CDCl_3$, 500 MHz, 298K)

4b ^{1}H-NMR ($CDCl_3$, 500 MHz), δ: 8.56 (t, 2H), 8.21 (d, 2H), 7.13 (t, 2H), 2.87 (t, 2H), 2.68 (t, 2H), 2.44 (s, 3H), 2.32 (s, 3H), 1.70 (m, 4H), 1.57 (m, 4H), 1.21 (broad, 12H)

MS (ESI,+,MeOH): *m/z* [M+H$^+$], 385.3, calc. 385.22

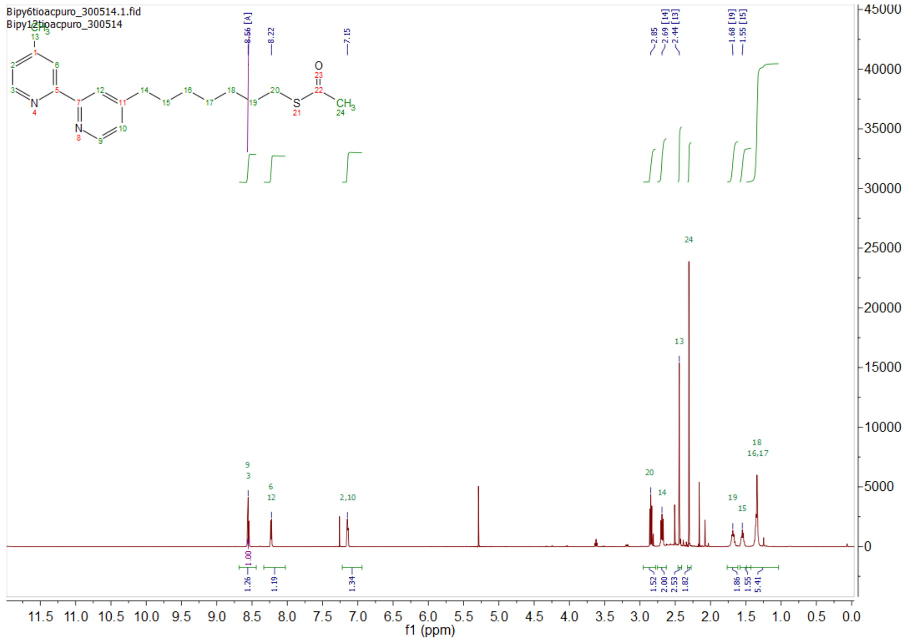

Figure S3. ^{1}H-NMR spectra of **4c** in $CDCl_3$ ($CDCl_3$, 500 MHz, 298K)

4c ^{1}H-NMR (CDCl$_3$, 500 MHz), δ: 8.56 (t, 2H), 8.22 (d, 2H), 7.14 (t, 2H), 2.85 (t, 2H), 2.69 (t, 2H), 2.44 (s, 3H), 2.31 (s, 3H), 1.68 (quint, 2H), 1.55 (quint, 2H), 1.34 (m, 6H)

MS (ESI,+,MeOH): *m/z* [M+H$^+$], 343.1, calc. 343.18

2.5.4. Synthesis of 8-trimethylammonium octanethiol (Thiol 1)

1,8-Dibromoctane (4.35 g, 16.0 mmol) was dissolved in acetone (40 mL). Potassium thioacetate was added (1.826 g, 15.99 mmol) and the resulting mixture was kept at room temperature under nitrogen overnight. After evaporation of the solvent, the yellowish solid was dissolved with CH$_2$Cl$_2$ and extracted with water (3 x 40 mL). The organic phase was dried with Na$_2$SO$_4$. After solvent evaporation, the crude product was purified by flash chromatography (silica gel, eluent: CH$_2$Cl$_2$, rf=0.71). 1.75 g (41%) of 8-thioacetyl-octyl bromide were obtained as a yellowish oil.

^{1}H-NMR (CDCl$_3$, 500 MHz), δ: 3.38 (t, 2H), 2.84 (t, 2H), 2.30 (s, 3H), 1.83 (quint, 2H), 1.55 (quint, 2H), 1.33 (br, 8H).

8-Thioacetyl-octyl bromide (0.500 g, 1.87mmol) was dissolved in AcN (10 mL). Trimethylammine ethanol solution (30% w/w) was added (0.35 g, 1.78 mmol) and the reaction was performed in a sealed tube at 82°C overnight. After solvent evaporation, the crude 8-thioacetyl-1-trimethylammonium-octane was purified by flash chromatography (silica gel, eluent: CH$_2$Cl$_2$, and then MeOH). 0.49g (81%) were obtained as a white solid.

^{1}H-NMR (ACN, 500 MHz), δ: 3.15 (m, 2H), 2.94 (s, 9H), 2.69 (t, 2H), 2.26 (s, 3H) 1.53 (broad, 2H), 1.39 (quint, 2H), 1.17 (m, 8H)

MS (ESI,+, H$_2$O): *m/z* [M+H$^+$], 246.3, calc. 246.19

8-Thioacetyl-1-trimethylammonium-octane (0.200 g, 0.62 mmol) was dissolved in EtOH (2 mL). HCl 6M (2 ml) was added and the reaction was performed under nitrogen at 78°C for 3 hours. After solvent evaporation 0.145 g (98%) of pure product were obtained as a white solid.

^{1}H-NMR (ACN, 500 MHz), δ: 3.15 (m, 2H), 2.95 (s, 9H), 2.42 (t, 2H), 1.77 (t, 2H), 1.62 (m, 2H),1.50 (m, 2H,), 1.17 (m, 6H).

2.5.5. Synthesis of Au NP I

All the glassware used in the nanoparticles preparation was washed with aqua regia and rinsed with distilled water. $HAuCl_4$ is strongly hygroscopic and was weighted within a dry-box.

A solution of $HAuCl_4 \cdot H_2O$ (100 mg, 0.281 mmol) in water (7 mL) was extracted with a solution of tetraoctylammonium bromide (2.74 g, 5.01 mmol) in N_2 purged toluene (125 mL divided in 3 portions). To the resulting reddish-orange organic solution, a second solution of tetraoctylammonium bromide (2.74 g, 5.01 mmol) and dioctylamine (3.36 g, 13.9 mmol) is added (the amount of dioctylamine was calculated in order to obtain 2 nm nanoparticles). The mixture is vigorously stirred under N_2 for 30 min. During this period of time the colour of the mixture fades. A solution of $NaBH_4$ (93.0 mg, 2.46 mmol) in H_2O (4.20) is then rapidly added. The colour of the solution turns rapidly to black due to nanoparticles formation. After 5 hours of stirring, the aqueous layer is removed. To a suitable portion of the above nanoparticle solution, different amounts of solutions of 2 and 3 in isopropanol were rapidly added in the desired ratios. The precipitation of Au NP was immediately observed. After addition of 5 ml of water, the aqueous layer was extracted several times with toluene, diethyl ether and ethyl acetate and finally evaporated. Finally the samples were purified by Sephadex G-25 resin (eluent: water).and Sephadex L-20 (eluent: MeOH).

Au NP **I** was characterized by ^{1}H-NMR (Figure S4), TEM, DLS and TGA analysis (Figure S5). The obtained NMR spectra with (S4 B) and without (S4 A) the diffusion filter showed that only minimal amounts of unbound additives were present in the final sample.

TEM analysis yields an average diameter for the inorganic core of the Au NP of 1.2 ± 0.3 nm. The size of the nanoparticles was confirmed by dynamic light scattering (6.8 nm). NMR analysis (Figure S4) indicate monolayer formation (broadening of all bands), as confirmed by diffusion filtered experiments.

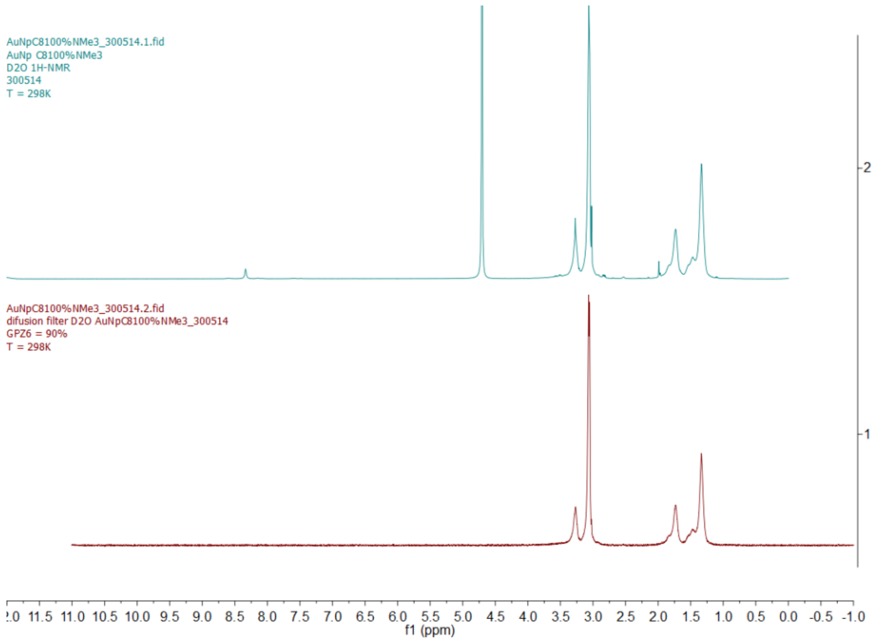

Figure S4. ^{1}H-NMR of AuNPs **I** in D_2O A) ^{1}H-NMR diffusion filter off B) ^{1}H-NMR diffusion filter on, (D_2O, 500 MHz, 298K)

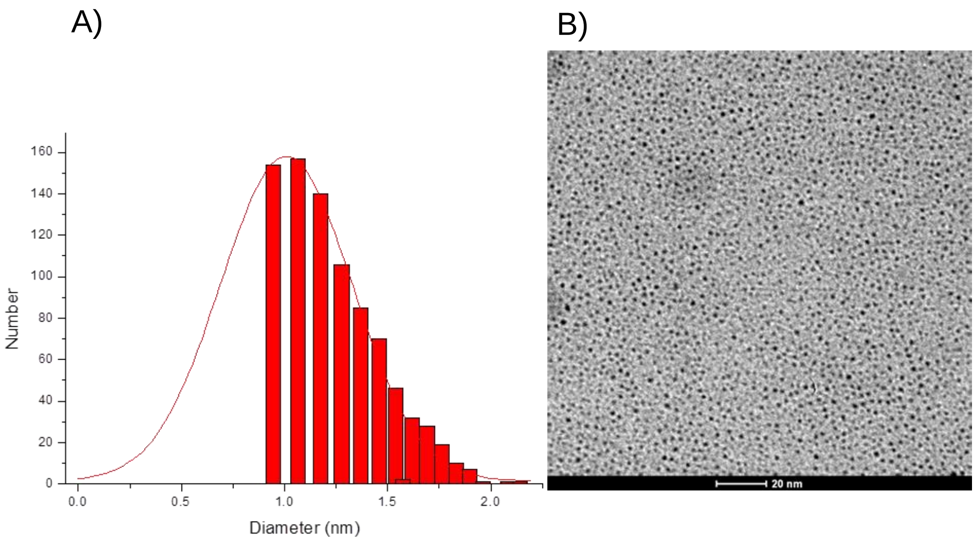

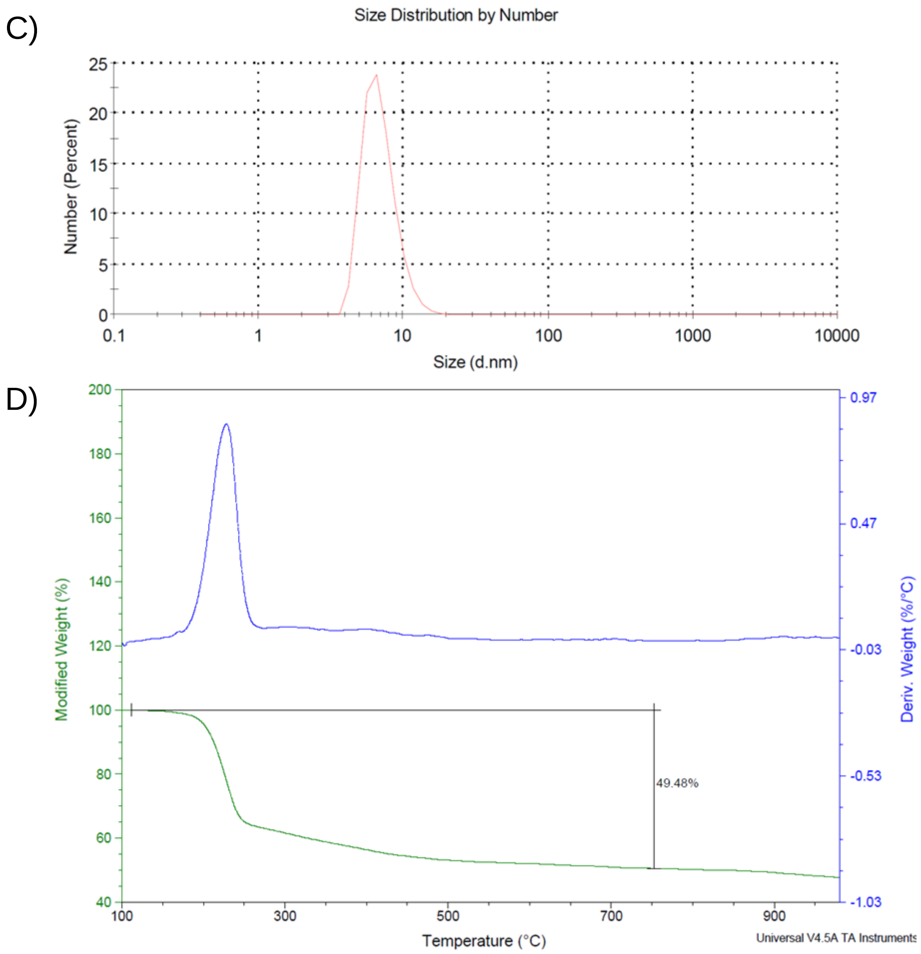

Figure S5. A) ImageJ elaboration corresponding to B) TEM image (scale bar 20 nm) B) C) DLS analysis D) TGA analysis

Finally, the weight loss measured by TGA was 49.48% (Figure S5) that is comparable to data reported before (Figure S5 D).[30]

2.5.6. Determination of the AuNPs I concentration

The quantification of the trimethylammonium head group was carried out through ^{1}H-NMR spectroscopy and pyrazine was used as internal standard. Considering the presence of aromatic protons in the internal standard the delay time t1 was increased to 10 s. In order to recover the sample of nanoparticles a coaxial internal tube was used. An example of ^{1}H-NMR is reported in figure S6. Considering that the singlet due to the presence of pyrazine integrated for 4H and the broad peaks belonging to the thiols on the nanoparticles integrated for

12 H, knowing the concentration of the internal standard it is easy to calculate the concentration of the head group on the nanoparticles with the following formula, where 0.108 is a coefficient that consider the presence of a coaxial tube.

$$\frac{4}{12} \times 11.97 \times [pyrazine] \times 0.108 = [Head\ groups]$$

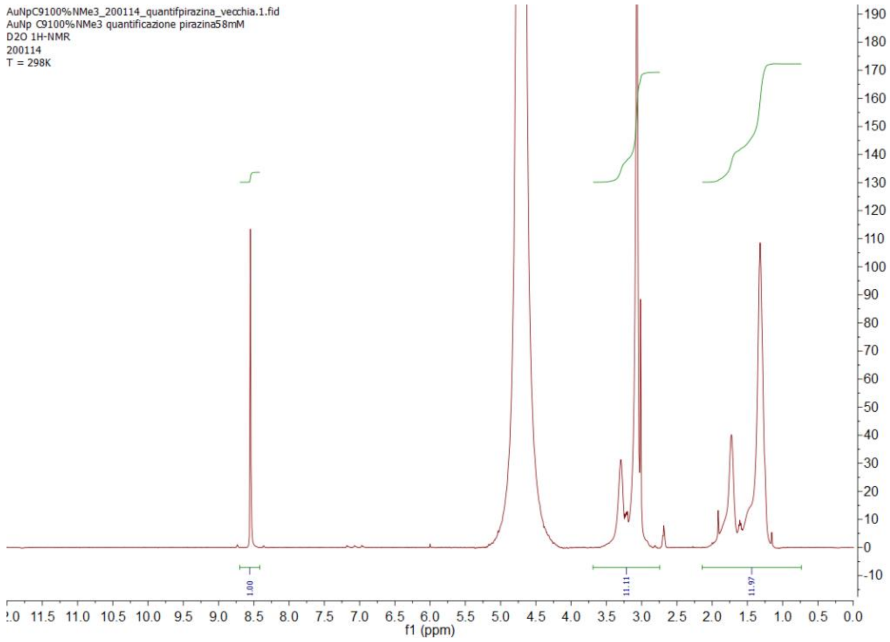

Figure S6. ^{1}H-NMR of AuNPs **I** for the quantification of trimethylammonium head groups in D_2O, (D_2O, 500 MHz, 298K)

2.5.7. Synthesis of Au NP III and Au NP IV

Starting from Au NP **I**, mixed monolayer gold nanoparticles were synthetized by ligand place exchange reactions using thiols **5a** (Au NP **II**), **5b** (Au NP **III**), **5c** (Au NP **IV**) The synthesis of these Au NP required an accurate optimization of the experimental parameters. For Au NP **III** the optimized parameters were 1.5 h of exchange, ratio free thiol/headgroup 0.5/1 carried out in EtOH/H_2O 2/1. Diffusion filter ^{1}H-NMR experiments in D_2O, allowed us to identify the peaks related to the thiol **5b** attached to the gold nanoparticles.

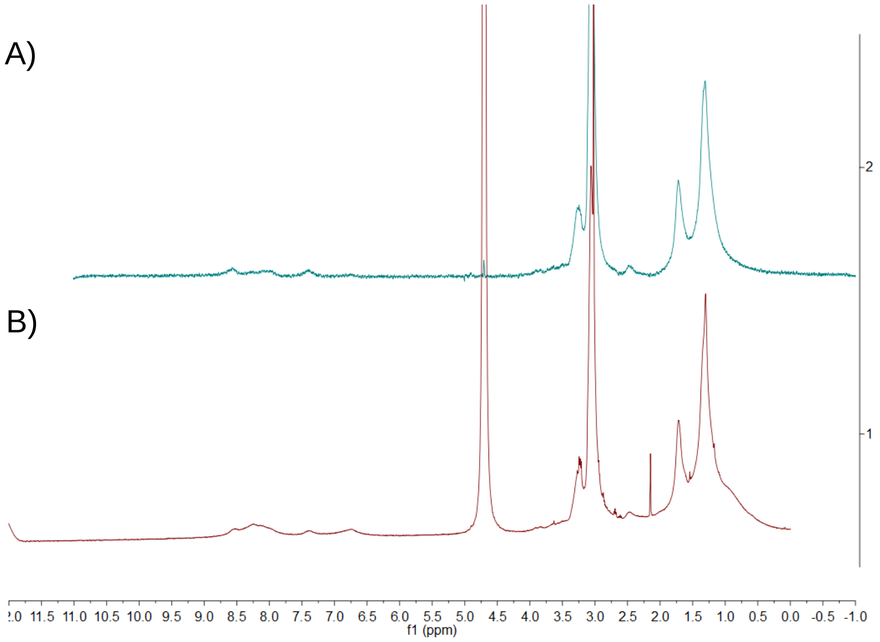

Figure S7. ^{1}H-NMR spectra of Au NP **III** in D_2O A) ^{1}H-NMR diffusion filter on B) ^{1}H-NMR diffusion filter off (D_2O, 500 MHz, 298K)

Au NP **IV** were synthetized with a slightly different protocol compared to Au NP **III** (6 h of exchange, ratio free thiol/headgroup 0.8/1 carried out in EtOH/H_2O 1/1).

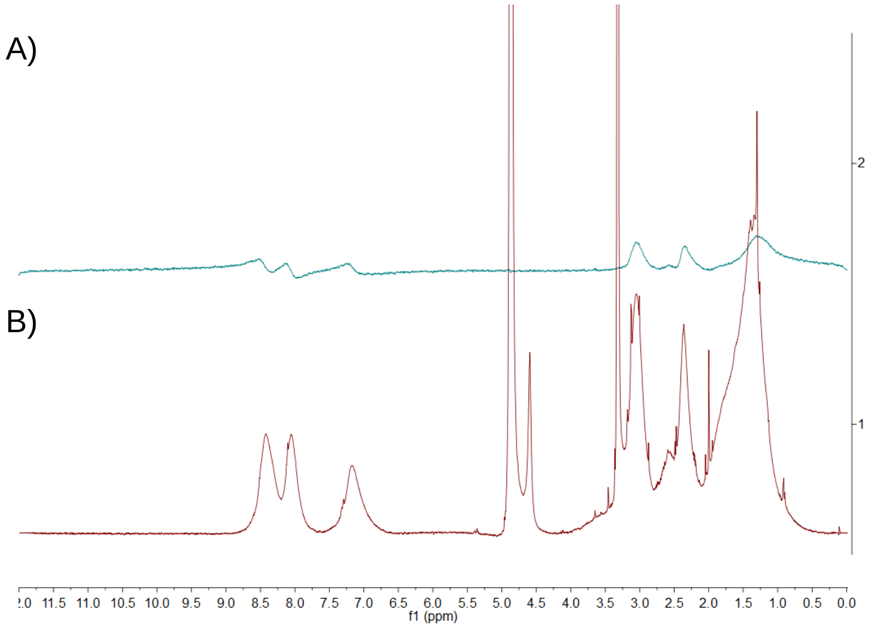

Figure S8. ^{1}H-NMR of Au NP **IV** in D_2O A) ^{1}H-NMR diffusion filter on B) ^{1}H-NMR diffusion filter off (D_2O, 500 MHz, 298K)

Au NP **III** and **IV** were additionally characterized by TEM, DLS and TGA revealing respectively an average diameter of 1 nm and 1.1 nm. The hydrodynamic radius observed by DLS were 8.6 ± 3 nm and 4.6 ± 0.66 nm, respectively. Finally the weights loss measured by TGA were 43.10% and 63.06%. It is interesting to observe that, during the increase of the temperature, in both cases a change in the slope was observed. This is a further indication of the presence of two different thiols on the surface.

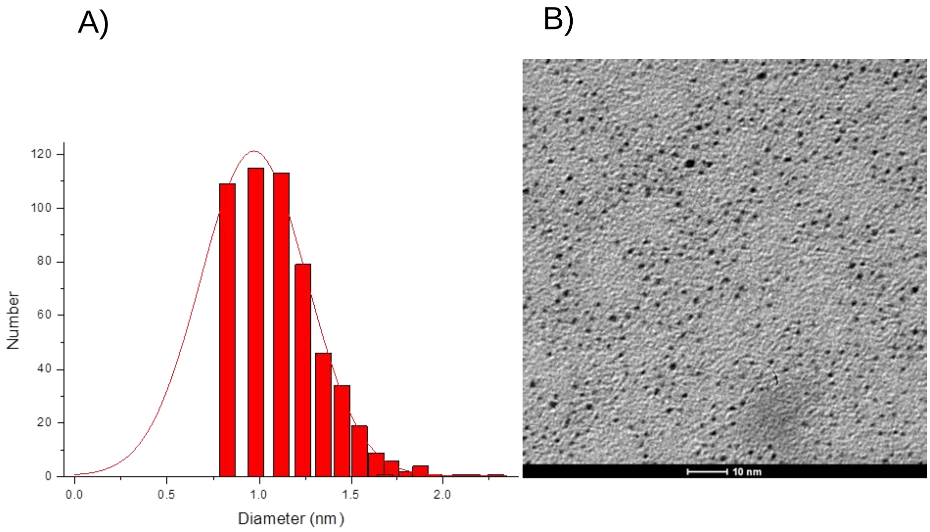

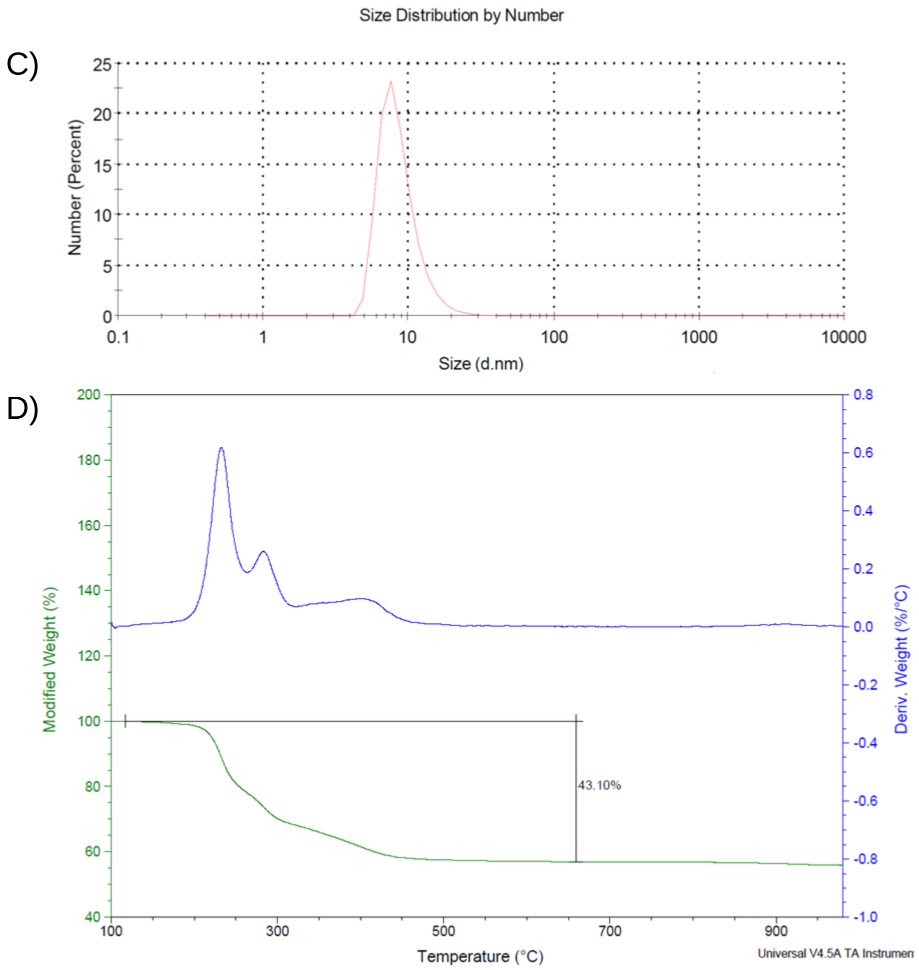

Figure S9. A) ImageJ elaboration corresponding to B) TEM image (scale bar 10 nm) C) DLS analysis D) TGA analysis of Au NP **III**

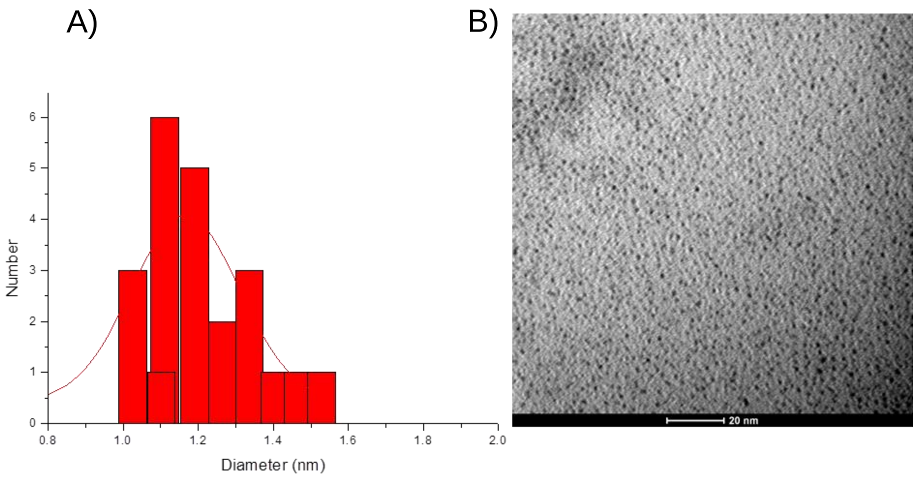

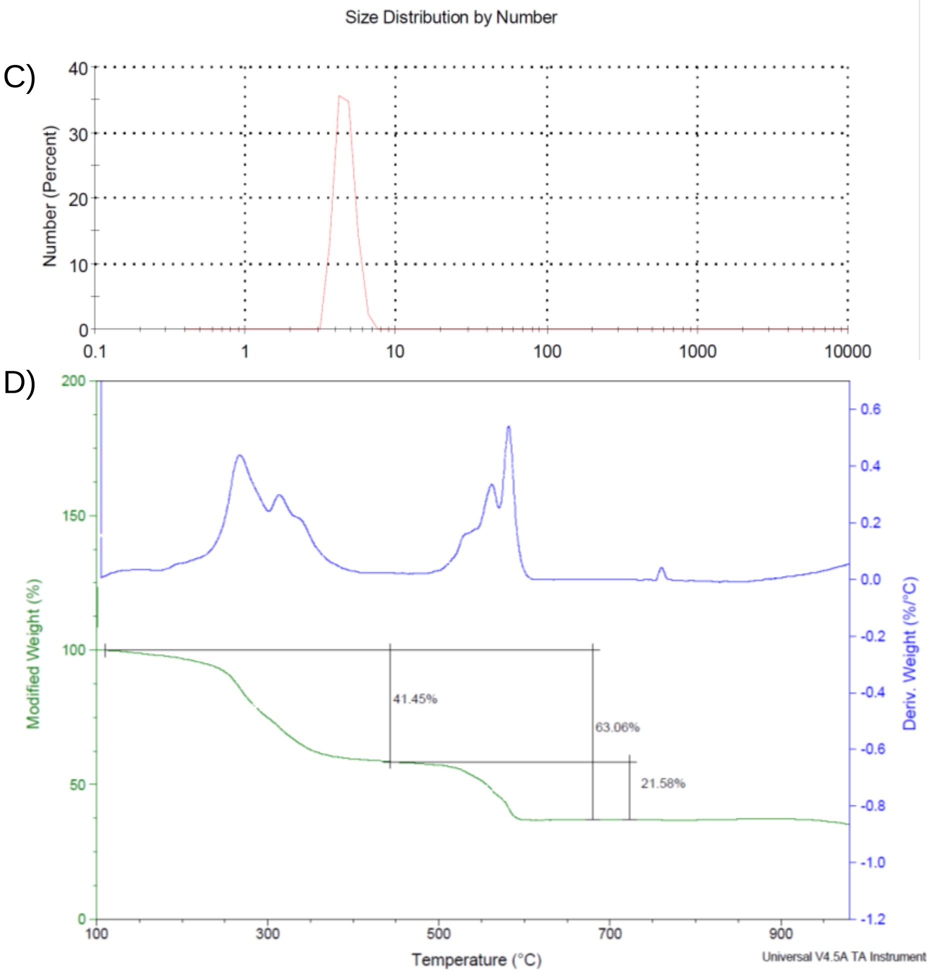

Figure S10. A) ImageJ elaboration corresponding to B) TEM image (scale bar 10 nm) C) DLS analysis D) TGA analysis of Au NP **IV**

2.5.8. Determination of the concentration of bipyridine head groups on Au NP III and Au NP IV

Control experiment

To a 1 mL buffered solution (MES pH 6,5) 70 µM (12 mg) of dmbipy, previously dissolved in DMSO, were added. Then, an increasing amount of Cu^{2+} was added to the solution and the absorption spectra were recorded after each addition. The absorption at 280 nm (λ_{max} of dmbipy) and at 310 (λ_{max} of the dmbipy-Cu^{2+} complex) were plotted against the [Cu^{2+}]. The interpolation of the straight line given by the curve provided the concentration of saturation of dmbipy by Cu^{2+}(about 65µM). After the validation of the method, the same procedure was performed with AuNP **III** and **IV**.

In Figure 2.13 are reported the curves obtained after the titration of Cu^{2+} on AuNP **III**.

In Figure S11 the absorption curves obtained after titration of Cu^{2+} on AuNP **IV** are shown.

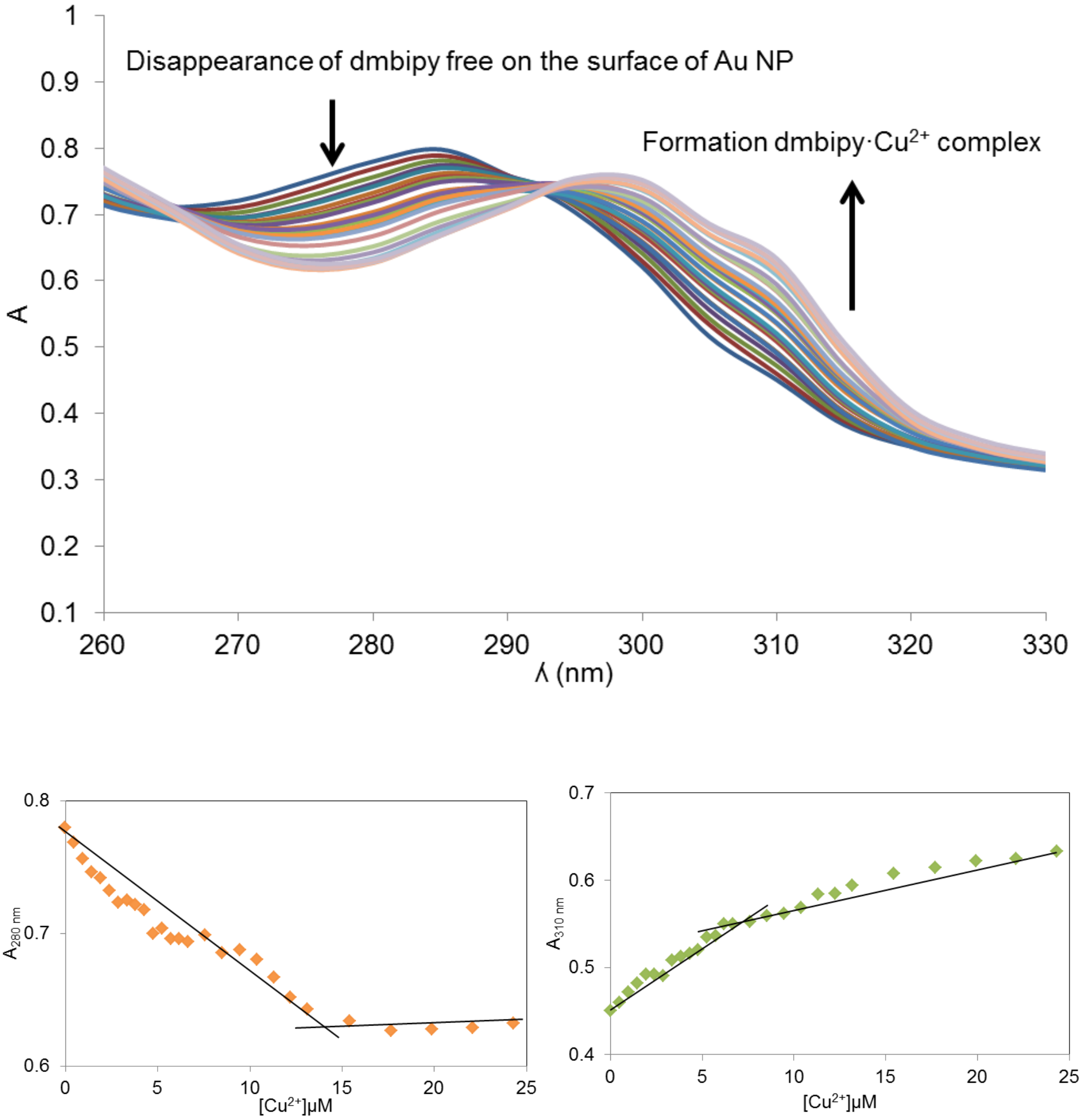

Figure S11. A) UV spectrum of AuNP **IV** at increasing amount of Cu^{2+} B) Absorbance as function of $[Cu^{2+}]$ at 280 nm C) Absorbance as function of $[Cu^{2+}]$ at 310 nm

The absorption at 280 nm and 310 nm was plotted in function of the concentration of Cu^{2+} titrated. The saturation profiles indicated the quantitative formation of the complex and showed an average concentration of dmbipy moiety on the surface about 14 μM.

2.5.9. Synthesis of compound 10

2.5.10. 2-acetyl-1-methylimidazole

The substrate was synthesized following a reported procedure.[31]

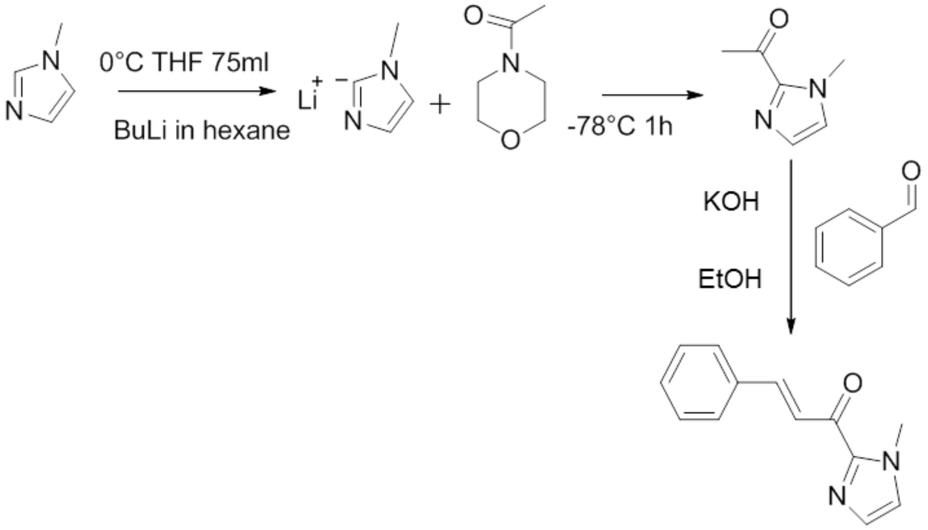

Figure S12. Synthesis of the substrate

2-acetyl-1-methylimidazole: 4-acetylmorpholine (11.6 mL, 100 mmol, 1,0 equiv) and THF (100 mL) were added to a 500 mL round bottom flask and cooled to -78 °C. 1- methylimidazole (8.8 mL, 110 mmol, 1,1 equiv) and THF (75 mL) were added to 5 min, and saturated NaCl (30 mL) and saturated $NaHCO_3$ (30 mL) were added. The resulting mixture was transferred to a separatory funnel, and extracted with EtOAc (3 x 100 mL). The organic extracts were combined and dried over sodium sulfate. The solution was concentrated on a rotatory evaporator and dried under vacuum to give a pale orange oil. The unpurified oil was enriched in the product (~90%, ^{1}H NMR) and used without further purification.

2.5.11. 2-Cinnamoyl-1-methyl-1H-imidazole 10

2-acetyl-1-methylimidazole (1,24 g, 10,0 mmol, 1,0 equiv) and EtOH (20 mL) were added to a 100 mL RBF followed by the benzaldehyde (10,0 mmol, 1,0 equiv) and a catalytic amount of KOH (2 pellets, ~100 mg). The solution was stirred for 12 h depending upon howquickly the product precipitated from the solution. The solution was filtered and the product was washed with water (20 mL) and EtOH (25 mL).
The compound **11** (0.8 g, 42%) was obtained as a white solid Rf = 0.40 (90/10 ether/hexane).

^{1}H NMR (500 MHz, $CDCl_3$) δ 8,12 (d, 1H), 7.87 (d, 1H), 7.74 (m, 2H), 7.42 (m, 3H), 7.29 (s, 1H), 7.11 (s, 1H), 4.13 (s, 3H);
MS (ESI,+, MeOH): *m/z* [M+H$^+$], 212.2 , calc. 213.07

2.5.12. General procedure for the Cu^{2+}-catalyzed Diels Alder cycloaddition

A 5 mL solution of Cu^{2+} catalyst* (0.1 mM) in 30 mM MES buffer, pH 6.5, was prepared. To this solution was added 20 µL solution of dienophile 2-cinnamoyl-1-methyl-1*H*-imidazole (2 mM in DMSO (500 mM), in order to obtain a final concentration in solution of 2 mM. After addition of cyclopentadiene (20 µL, final concentration 16 mM) the reaction was stirred 5 days by continuous inversion at r.t. The product was isolated by extraction with EtOAc (2x 10 ml). After drying (Na_2SO_4) and removal of the solvent the crude product was dissolved in 1 mL of hexane and analyzed by HPLC. Conditions: 2,5%-5% B in 20 minutes; A: hexane, B: isopropanol.
*The concentration of catalytic groups on nanoparticle was measured as reported in **5.10** and 0.1 mM of bipy-Cu^{2+} head groups was used as catalyst.

2.5.13. Synthesis of BP1

A suspension of 4,4'-dimethyl-2,2'-bipyridine (4.6 g, 25 mmol) and SeO_2, (3.13g, 25mmol) in 1,4-dioxane (260mL) was heated at reflux for 24h with stirring and filtered hot. The filtrate was cooled to room temperature resulting in the formation of a precipitate which was filtered off as a light-brown solid. After the solvent was removed by rotary evaporation, the residue was treated in ethyl acetate (500 mL) and filtered to remove a solid. The filtrate was extracted with 1.0 M Na_2CO_3 (2 x 100mL) to remove carboxylic acids and with 0,3M $Na_2S_2O_5$ (3 x 100mL) to form aldehyde bisulfite addition compound(s). The combined aqueous extracts were adjusted to pH 10 with Na_2CO_3 to release the aldehyde(s) and extracted with CH_2Cl_2 (4 x l00mL). Solvent was removed from the combined organic extracts under vacuum to afford the monoaldehyde (34%) as a white solid.

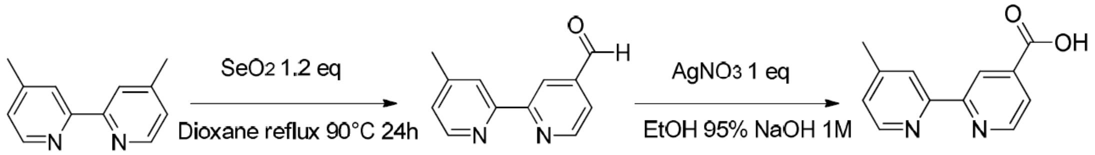

Figure S13. Synthesis of4-methyl-2,2'-bipyridine-4-carboxylic acid

^{1}H NMR (500 MHz, $CDCl_3$) ƌ 2,47 (s, 3H), 7,20 (d 1H), 7,72 (d, 1H). 8,28 (d 1H), 8,58 (d, 1H), 8.83 (broad s, 1H), 8,90 (d,1H), and 10,19ppm (s, 1H)).

Then, a solution of $AgNO_3$ (7.2 mmol) in water (20mL) was added to a suspension of the monoaldehyde (8 mmol) in 95% ethanol (95 mL). The yellow suspension was stirred rapidly as a solution of 1 M NaOH (50mL) was added dropwise over 20min to form Ag_2O. The dark black reaction mixture was stirred rapidly for 15 h. Ethanol was removed by rotary evaporation and the aqueous residue was filtered through a fine-porosity glass frit to remove Ag_2O and metallic silver. The solids were washed with 1.3M NaOH (2 x 20mL) and water (20mL). The combined basic filtrates were extracted with CH_2Cl_2 2 x 50 mL) to remove unreacted aldehyde and adjusted to pH3.5 with 1:1(v/v) 4N HCl/acetic acid, which produced a white precipitate. After the mixture was kept at 0°C was 4 hours , the white solid was collected and vacuum dried to afford pure 4-methyl-2,2'-bipyridine-4-carboxylic acid (85% yield).

^{1}H NMR ($(CD_3)_2SO$) ƌ 2,43 (broad s, 3 H) 7.34 (d, 1H), 7,87 (d 1H), 8,27 (d, 1H), 8,59 (d,1H), 8,84 (d, 1H), 8,87 (d,1H)

MS (ESI,+, MeOH): *m/z* [$M+H^+$], 213,0 calc. 212.09

2.6. BIBLIOGRAPHY

1. Gennari, C. & Piarulli, U. Combinatorial libraries of chiral ligands for enantioselective catalysis. *Chem. Rev.* **103,** 3071–100 (2003).
2. Reetz, M. T. Combinatorial Transition-Metal Catalysis: Mixing Monodentate Ligands to Control Enantio-, Diastereo-, and Regioselectivity. *Angew. Chem. Int. Ed.* **47,** 2556–2588 (2008).
3. Van Leeuwen, P. W. N. M. *Supramolecular catalysis*. (Wiley-VCH, 2008).
4. Astruc, D., Lu, F. & Aranzaes, J. R. Nanoparticles as recyclable catalysts: the frontier between homogeneous and heterogeneous catalysis. *Angew. Chem. Int. Ed. Engl.* **44,** 7852–72 (2005).
5. Reetz, M. T. & Jiao, N. Copper-phthalocyanine conjugates of serum albumins as enantioselective catalysts in Diels-Alder reactions. *Angew. Chem. Int. Ed. Engl.* **45,** 2416–9 (2006).
6. Mahammed, A., Gray, H. B., Weaver, J. J., Sorasaenee, K. & Gross, Z. Amphiphilic corroles bind tightly to human serum albumin. *Bioconjug. Chem.* **15,** 738–746 (2004).
7. Gantchev, T. G., Ouellet, R. & van Lier, J. E. Binding interactions and conformational changes induced by sulfonated aluminum phthalocyanines in human serum albumin. *Arch. Biochem. Biophys.* **366,** 21–30 (1999).
8. Chatterjee, S. & Srivastava, T. S. Spectral investigations of the interaction of some porphyrins with bovine serum albumin. *J. Porphyr. Phthalocyanines* **4,** 147–157 (2000).
9. Ding, Y., Lin, B. & Huie, C. W. Binding studies of porphyrins to human serum albumin using affinity capillary electrophoresis. *Electrophoresis* **22,** 2210–2216 (2001).
10. Kragh-Hansen, U., Chuang, V. T. G. & Otagiri, M. Practical aspects of the ligand-binding and enzymatic properties of human serum albumin. *Biol. Pharm. Bull.* **25,** 695–704 (2002).
11. Rideout, D. C. & Breslow, R. Hydrophobic Acceleration of Diels-Alder Reactions. *J. Am. Chem. Soc.* **102,** 7816–7817 (1980).
12. Roelfes, G. & Feringa, B. L. DNA-based asymmetric catalysis. *Angew. Chem. Int. Ed. Engl.* **44,** 3230–2 (2005).

13. Boersma, A. J., Megens, R. P., Feringa, B. L. & Roelfes, G. DNA-based asymmetric catalysis. *Chem. Soc. Rev.* **39,** 2083–92 (2010).
14. Evans, D. a. & Fandrick, K. R. Catalytic enantioselective pyrrole alkylations of α,β- unsaturated 2-acyl imidazoles. *Org. Lett.* **8,** 2249–2252 (2006).
15. Evans, D. a, Song, H.-J. & Fandrick, K. R. Enantioselective nitrone cycloadditions of alpha,beta-unsaturated 2-acyl imidazoles catalyzed by bis(oxazolinyl)pyridine-cerium(IV) triflate complexes. *Org. Lett.* **8,** 3351–4 (2006).
16. Dydio, P., Rubay, C., Gadzikwa, T., Lutz, M. & Reek, J. N. H. 'Cofactor'-controlled enantioselective catalysis. *J. Am. Chem. Soc.* **133,** 17176–9 (2011).
17. Pieters, G. & Prins, L. J. Catalytic self-assembled monolayers on gold nanoparticles. *New J. Chem.* **36,** 1931 (2012).
18. Boersma, A. J., Feringa, B. L. & Roelfes, G. Alpha,beta-unsaturated 2-acyl imidazoles as a practical class of dienophiles for the DNA-based catalytic asymmetric Diels-Alder reaction in water. *Org. Lett.* **9,** 3647–50 (2007).
19. Peterson, J. ^{1}H-NMR Analysis of Mixtures Using Internal Standards A Quantitative Experiment for the Instrumental Analysis Laboratory. *Journal of Chemical Education* **69,** 843–845 (1992).
20. Norsten, T. B., Frankamp, B. L. & Rotello, V. M. Metal Directed Assembly of Terpyridine-Functionalized Gold Nanoparticles. *Nano Letters* **2**, 1345-1348 (2002).
21. Jana, N. R. & Peng, X. Single-phase and gram-scale routes toward nearly monodisperse Au and other noble metal nanocrystals. *J. Am. Chem. Soc.* **125,** 14280–1 (2003).
22. Manea, F., Bindoli, C., Polizzi, S., Lay, L. & Scrimin, P. Expeditious synthesis of water-soluble, monolayer-protected gold nanoparticles of controlled size and monolayer composition. *Langmuir* **24,** 4120–4124 (2008).

23. Hostetler, M. J., Templeton, A. C., Murray, R. W., Hill, C. & Carolina, N. Dynamics of Place-Exchange Reactions on Monolayer-Protected Gold Cluster Molecules. *Langmuir* **15**, 3782–3789 (1999).
24. Wu, D. H., Chen, a. D. & Johnson, C. S. An Improved Diffusion-Ordered Spectroscopy Experiment Incorporating Bipolar-Gradient Pulses. *J. Magn. Reson. Ser. A* **115,** 260–264 (1995).
25. Ishihara, K. & Fushimi, M. Design of a Small-Molecule Catalyst Using Intramolecular Cation−π Interactions for Enantioselective Diels−Alder and Mukaiyama−Michael Reactions : L-DOPA-Derived Monopeptide, Cu (II) Complex. *Organic Letters* **4,** 10412–10413 (2006).
26. Otto, S. & Engberts, J. B. F. N. A Systematic Study of Ligand Effects on a Lewis-Acid-Catalyzed Diels - Alder Reaction in Water . *J. Am. Chem. Soc.* **121**, 6798–6806 (1999).
27. Link, S. & El-Sayed, M. a. Shape and size dependence of radiative, non-radiative and photothermal properties of gold nanocrystals. *Int. Rev. Phys. Chem.* **19,** 409–453 (2000).
28. Bos, J. & Roelfes, G. Artificial metalloenzymes for enantioselective catalysis. *Curr. Opin. Chem. Biol.* **19,** 135–43 (2014).
29. Gottlieb, H. E., Kotlyar, V. & Nudelman, A. NMR Chemical Shifts of Common Laboratory Solvents as Trace Impurities. *J. Org. Chem.* **62,** 7512–7515 (1997).
30. Bonomi, R., Cazzolaro, A. & Prins, L. J. Assessment of the morphology of mixed SAMs on Au nanoparticles using a fluorescent probe. *Chem. Commun. (Camb).* **47,** 445–7 (2011).
31. Myers, M. C., Bharadwaj, A. R., Milgram, B. C. & Scheidt, K. a. Catalytic conjugate additions of carbonyl anions under neutral aqueous conditions. *J. Am. Chem. Soc.* **127,** 14675–14680 (2005).

CHAPTER 3: ORTHOGONAL SENSING OF SMALL MOLECULES USING A MODULAR NANOPARTICLES-BASED ASSAY

3.1. INTRODUCTION

The development of universal assay able to detect a broad range of different molecular targets is highly desirable, as such modular platforms offer a single solution for tests that usually require a specific design of the system for each analyte. The presence of a recognition site able to selectively complex the target and a signaling unit that detects changes in the recognition site are essential components for a chemosensor. This has led to the development of molecular structures specifically designed to signal the presence of target analytes with high selectivity.[1,2] However, the excellent performances of such chemosensors are counterbalanced by their tedious synthesis and the limitation to detect only its specific analyte. For this reason, a strong interest in chemosensors relying on the self-assembly of recognition and signaling units to form a functional system arose in the last years. [3,4,5,6] Traditionally, the most widely used approach for chemosensors is the IDA (Indicator Displacement Assay).[5] In an IDA, an indicator is first allowed to bind reversibly to a receptor. Then, a competitive analyte is introduced into the system causing the displacement of the indicator from the host, which in turn modulates an optical signal. Based on this principle, the major requirement for an IDA is that the affinity between the indicator and the receptor is comparable to that between the analyte and the receptor. It implies that the indicator has to be designed around the receptor considering all the non-covalent interaction that can occur during the binding process. This is why there has been a growing interest in systems in which the macroscopic structure and the physical properties can undergo detectable changes in response to external stimuli and where a readout strategy is independent from the receptor.

An example of a universal detecting system is reported by Kelley et al in 2012.[7] Here, a neutralizer displacement assay is proposed that allows charge-based sensing to be applied to any class of molecule irrespective of the analyte charge. In traditional electrostatic assays (Figure 3.1 A), a probe molecule is tethered to the surface of an electrode. Thus, prior to analyte introduction, the charge of the sensor is determined by such a probe molecule. After interaction with the analyte, the overall charge changes. The neutralizer displacement assay (NDA, Figure. 3.1 B) introduces the possibility to apply the same concept to neutral molecules. A probe molecule is tethered to the surface of an electrode and is joined by a neutralizer, which is a conjugate of a peptide nucleic acid (PNA) and cationic amino acids that specifically binds to the probe and neutralizes the charge of the probe. The probe-neutralizer complex is designed to include mismatches such that the analyte of interest binds the probe more strongly, rapidly and robustly leading to displacement of the neutralizer. To test the NDA concept, Kelley and co-workers used an electrocatalytic reporter system that provides a signal proportional to the charge change at the electrode surfaces. This way, sensitivity is achieved with all of the major classes of analytes (e.g. deoxyribonucleic acid, ribonucleic acid, cocaine, adenosine triphosphate and thrombin). It is clear, though, that this system needs an accurate design of the aptamer and of PNA, whose structure is strictly dependent to the target analyte.

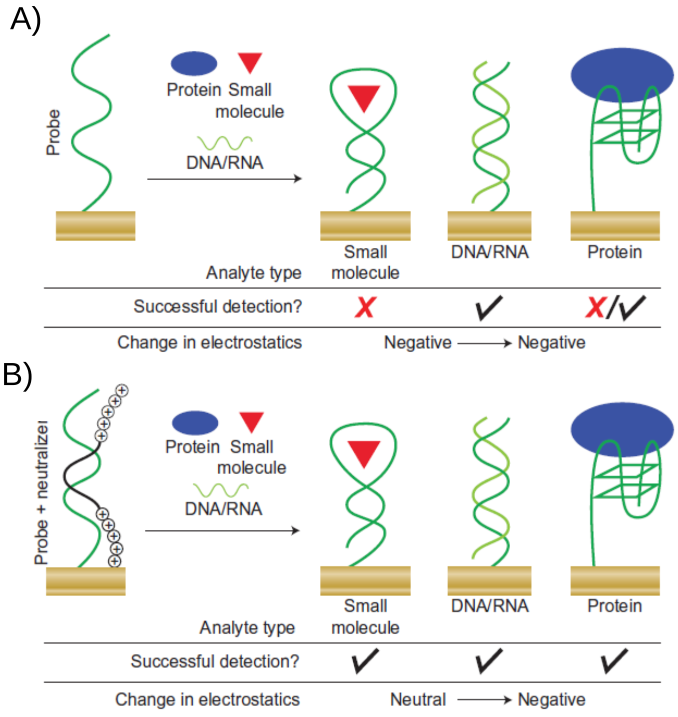

Figure 3.1. A) Traditional electrostatic detection. B) In NDA detection, small molecules, nucleic acids and proteins are all detectable as each one causes displacement of a neutralizer and a large change in charge.

Earlier, Xia and co-workers proposed a nearly universal colorimetric assay for the detection of DNA, small molecules, proteins and inorganic ions, employing single-stranded DNA probes, unmodified gold nanoparticles and a positively charged, water-soluble conjugated polyelectrolyte.[8] It is known that both single- and double-stranded DNA prevent gold nanoparticle aggregation at low salt concentrations and that, at specific conditions, the cationic conjugated polyelectrolyte poly[(9,9-bis (6-N,N,N-trimethylammonium) hexyl) fluorene-alt-1,4-phenylene] bromide (PFP-Br) preferentially binds single-stranded DNA to double-stranded or otherwise "folded" DNA. This appears to arise due to the greater hydrophobicity of single-stranded DNA. Starting from this observation an assay was constructed that relies on the ability of the system to detect double-stranded probe–target duplexes.

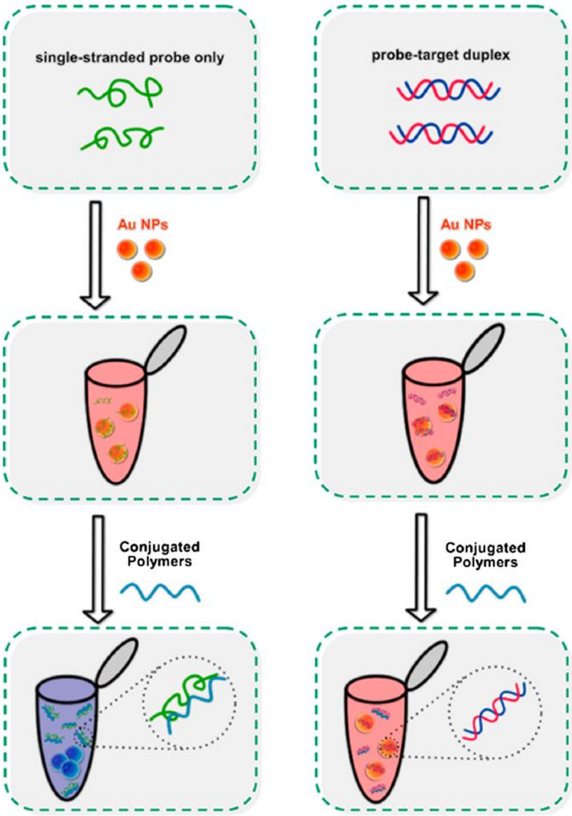

Figure 3.2. Assay principle

In this series of experiments, a solution of gold nanoparticles (*d* = 20 nm) is added to two samples: the first sample is the control, containing a single-stranded probe DNA; the second sample is the target solution, containing the probe DNA and its complementary DNA target. The addition of nanoparticles produced in both samples a readily visible red color due to the intense surface plasmon resonance (SPR) absorption of the nanoparticles at 520 nm. The subsequent addition of the conjugated polymer sequesters most of single-stranded DNA, leaving it unable to stabilize the nanoparticles against aggregation and thus leading to a characteristic blue color for the control sample (which only contains single-stranded DNA). In the presence of the complementary target sequence, a significant concentration of double-stranded DNA occurs, which only weakly binds the conjugated polyelectrolytes and thus remains largely free to stabilize the nanoparticles against aggregation. This, in turn, causes the sample to retain the red color associated with dispersed nanoparticles. Although this approach is convenient, allowing semiquantitative detection *via* visual and sensitive inspection (achieving picomolar detection limits for DNA detection), various steps are required to obtain the result that is strictly dependent on the stability conditions of DNA structure.

Another example was recently proposed by Hamachi and co-workers.[9] In this work, a redox responsive peptide-based hydrogel, able to encapsulate enzymes, was proposed. The ultimate goal of this work is to construct unique stimuli-responsive soft materials, capable of sensing a variety of disease-related biomarkers. The H_2O_2-responsive supramolecular hydrogels consist of di- and tripeptides, bearing a *N*-terminal H_2O_2-reactive boronoarylmethoxycarbonyl (BAmoc) group (Figure 3.3 A). The removal of the BAmoc unit through an oxidation/elimination reaction triggered by H_2O_2 was expected to induce destabilization of the self-assembled nanofibers and subsequent collapse of the gel and hence occurrence of a gel–sol transition (Figure 3.3 B).

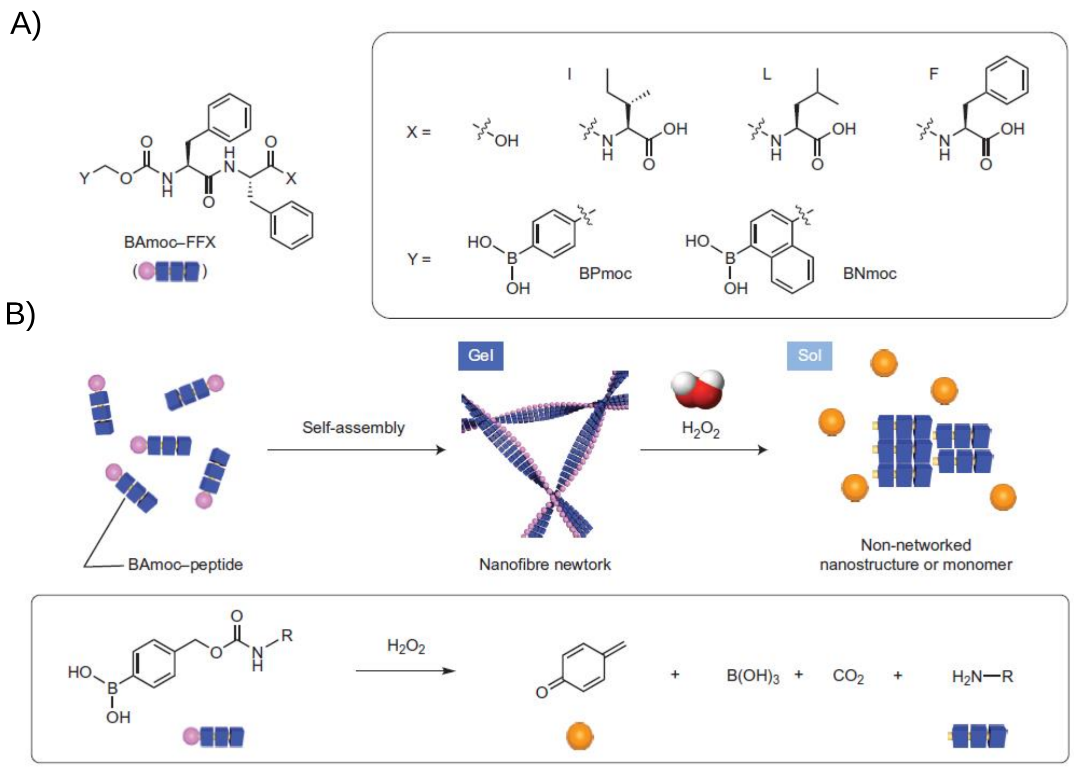

Figure 3.3. A) BAmoc–peptide hydrogels. BAmoc–peptides (FFX: F, phenylalanine; X: OH, isoleucine (I), leucine (L) or phenylalanine (F)). B) Schematic representation showing the self-assembly of BPmoc–peptides to form a nanofiber network (gel) and H_2O_2-triggered gel degradation (II).

H_2O_2 is naturally produced by oxidase enzymes involved in a variety of physiologically important biochemical pathways. When oxidases are embedded in the aforementioned hydrogel matrices, H_2O_2 is generated *in situ* and a gel–sol transition is triggered. In the same way, a reduction-responsive supramolecular hydrogel was developed. In this system, the reduction of the nitro group triggers the cleavage of the carbamate bond in NPmoc-F2 (Figure 3.4 A), leading to a collapse of the gel, causing a gel–sol transition. The lactic-acid sensing by the gel collapse was described by the following cascade reactions: NAD^+ is reduced to NADH during the oxidation of lactic acid by LDH in the hybrid gel, which facilitates the subsequent reduction of NPmoc-F2 by NR with the aid of the generated NADH (Figure 3.4 B). This system presents the advantage of an easy naked eye detection of the analytes, and overcomes the synthetic efforts. Critical points are the fact that each assay has to be prepared *ad hoc* for the target analyte and, in any case, does not permit the analysis of more than two molecules (two inputs). Another limit is the low sensitivity of the system.

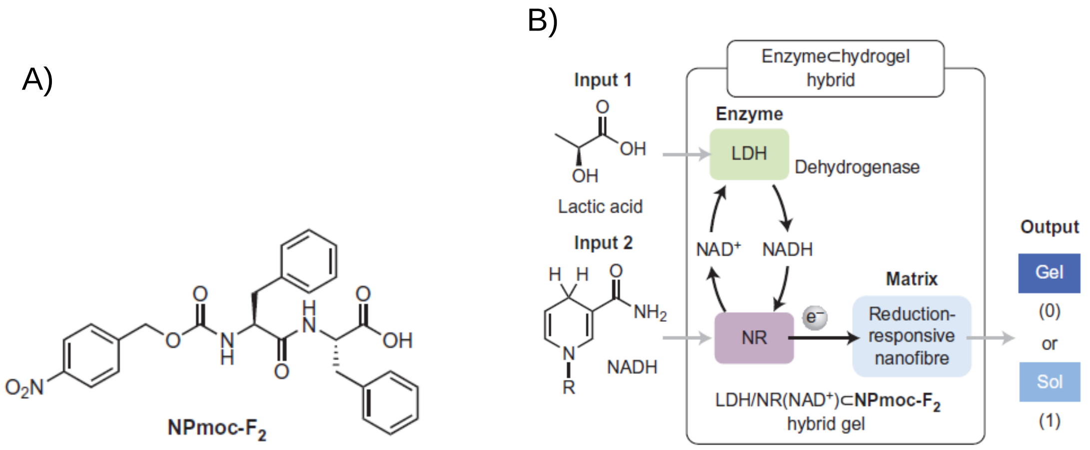

Figure 4. A) Chemical structure of NPmoc-F2. B) Schematic representation of the LDH/NR(NAD$^+$)-NPmoc-F2 hybrid gel. With the assistance of NR, NADH (input) can induce a gel–sol change as output through the degradation of a matrix that consists of reduction-responsive nanofibres. Also, NAD$^+$ in the hybrid gel is reduced to NADH during the oxidation of lactic acid (input) by LDH (NAD$^+$-dependent dehydrogenase), which eventually gives rise to a gel–sol change as output through the degradation of the matrix.

The main aim of the project is to create a universal modular gold nanoparticle-based system for the detection of small molecules, in which the design of the system and synthetic steps are reduced to a minimum. Au NP functionalized with TACN-Zn^{+2} moieties (Au NP **5**•Zn^{2+}) contain a positively charged monolayer that strongly interacts with negatively charged macrocycles (e.g. tetra-*p*-sulfonated calix[4]arenes, succinyl-*β*-cyclodextrins and sulfonate cavitands).[10] The addition of above-mentioned hosts promotes the displacement of a fluorescent probe previously present on the surface (signal on). We wondered whether the presence of a target guest for these hosts could alter their affinity for the nanoparticle and, in that way, alter the competition with the fluorophore. This difference should then be reflected by a change in the fluorescence intensity.

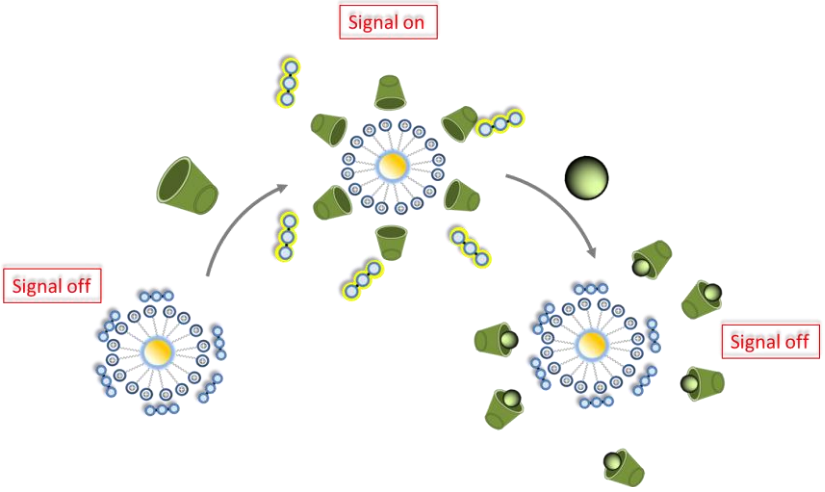

Figure 3.5. General representation of the steps of the assay.

The attractiveness of this system is given by the possibility to modulate the selectivity of the assay by simply changing or adding a different host, creating an *ad hoc* system for various needs. Indeed, the modular nature of the assay is attractive for the design of sensing systems because the selectivity can be tuned in a straightforward manner without changing the output signal (ΔFI at 450 nm). However, it also provides a controlled access to sensing systems of higher complexity that go beyond those developed to detect a single analyte. The idea, in fact, is to apply this general concept to a more complex system in which three different selective hosts are present on the nanoparticle surface at the same time. Such a system with a programmable response could then in principle be applied to Boolean logic gates (OR). Indeed, as illustration of the versatility and efficacy of the modular approach we show that the simultaneous use of different recognition modules gives the possibility to interpret the assay output signal as the result of a 3-bit molecular computing system.

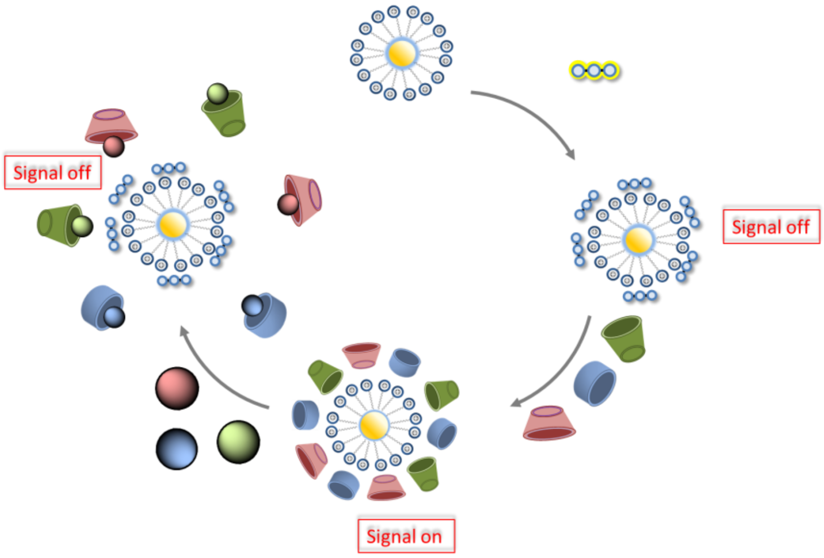

Figure 3.6. Representation of the steps of the modular assay.

3.2. RESULTS AND DISCUSSION

3.2.1. Determination of the surface saturation concentration

The synthesis and characterization of Au NP **5** has been described elsewhere[11]. The surface saturation concentration (SSC) of the fluorophore dATP$_{MANT}$ on Au NP **5**•Zn^{2+} was determined as described previously (λ_{ex} = 355 nm**,** λ_{em} = 448 nm, slit: 10/5 nm).[11] After each addition, the fluorescence intensity was measued after the signal had stabilized (typically up to 5 minutes). The obtained value was determined *via* extrapolation of the linear part of the curve (5 points). The SSC of **dATP$_{MANT}$** on Au NP **5**•Zn^{2+} (20 μM) was around 5.0 μM.

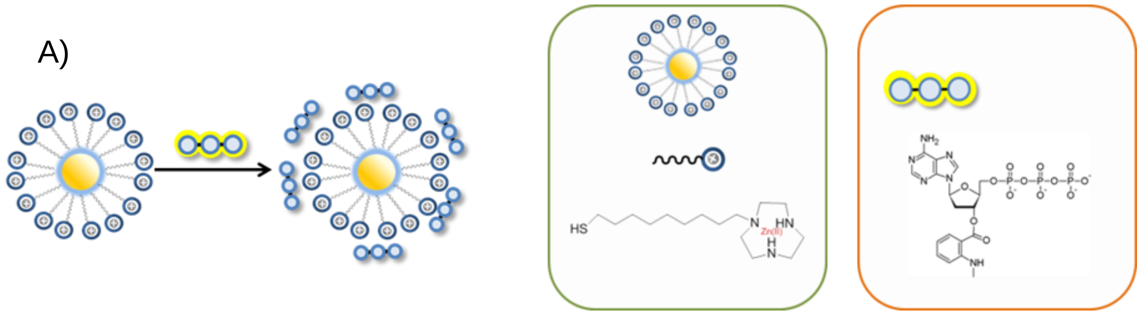

B)

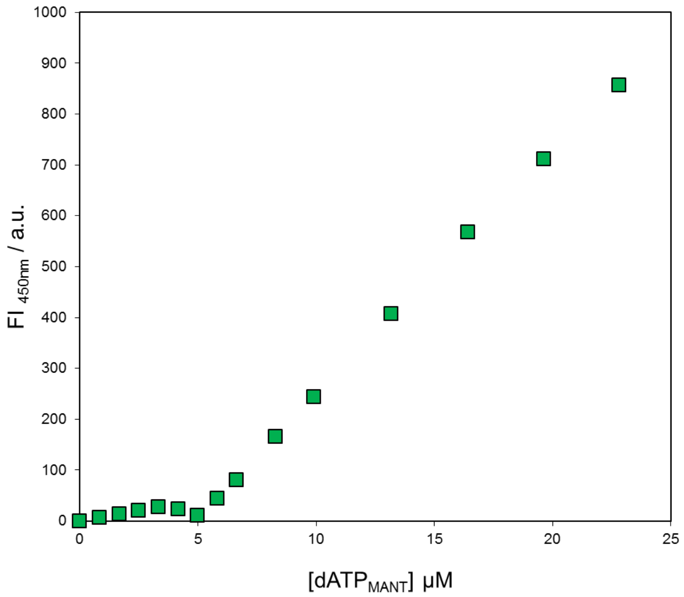

Figure 3.7. A) Schematic representation of the first step of the modular assay: determination of the fluorophore SSC.B) Fluorescence intensity as a function of the amount of $dATP_{MANT}$ added to a solution of Au NP **5**•Zn^{2+} [TACN] = 20 µM, [Zn^{2+}] = 20 µM, pH 7.0, 37 °C, λ_{ex} = 355 nm, λ_{em} = 448 nm, slit 10/5 nm.

3.2.2. Displacement experiments

The relative affinity of the negatively charged hosts **A-C** for the Au NP **5**•Zn^{2+} surface was determined using displacement experiments relying on a gradual displacement of $dATP_{MANT}$ upon the addition of increasing amounts of host.

In particular, we focused our studies on receptor **A**, because of its reported ability to detect sarcosine in acidified urine,[12] receptor **B** for its ability to interact with quaternary ammonium cations,[13,14] and receptor **C** which, due to its hydrophobic pocket forms inclusion complexes with hydrophobic compounds. This is of high interest for pharmaceutical as well as dietary supplement applications.

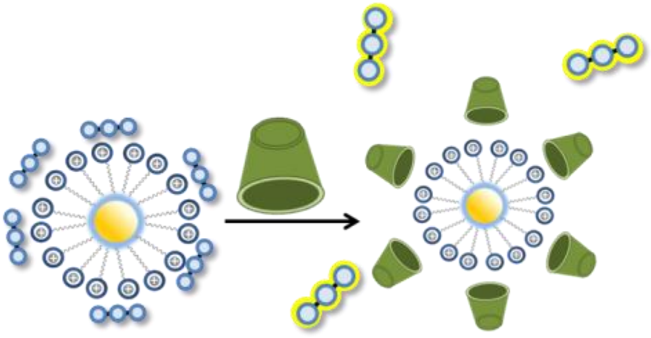

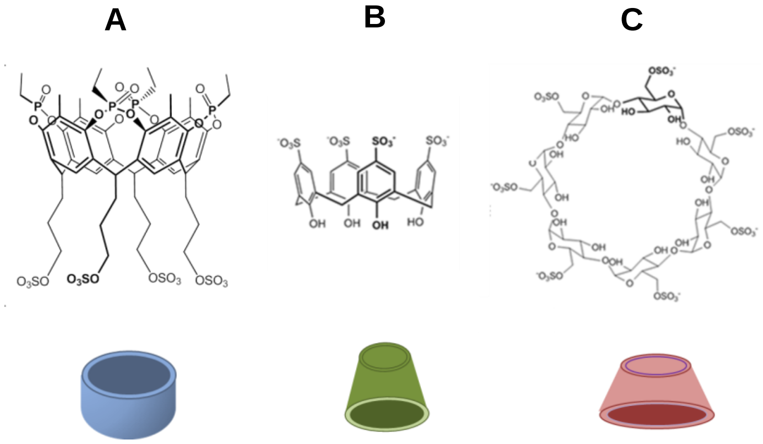

Figure 3.8. Schematic representation of the second step of the modular assay: displacement of the fluorescent probe from the surface promoted by the addition of one of the three hosts: phosphonate cavitand (**A**), sulfocalix[4]arene hydrate (**B**) heptakis(6-O-sulfo)-β-cyclodextrin heptasodium salt (**C**).

The displacement experiments were performed by measuring the fluorescent intensities upon adding consecutive amounts of a stock solution of the three hosts, phosphonate cavitand (**A**), sulfocalix[4]arene hydrate (**B**) and heptakis(6-O-sulfo)-β-cyclodextrin heptasodium salt (**C**) to buffered solution (HEPES 10 mM, pH = 7.0) containing Au NP **5**•Zn^{2+} covered with the fluorophore dATP$_{MANT}$ (5 μM). The fluorescent intensities, generated by the addition of small additional amounts of **A**, **B** and **C** to Au NP **5**•Zn^{2+} covered by the dATP$_{MANT}$, were registered. The curves reached a plateau, which, however, does not correspond to the maximum fluorescence intensities (FI) values expected for a full release of the probe. A plot of the FI against the concentratin of host allowed the determination of the optimal concentration of the host for the assay studies.

The concentration of receptor **A**-**C** ([**A**]= 5.8 μM, [**B**] = 6.5 μM, [**C**] = 6.15 μM) was chosen such to have a sufficient amount of **A-C** complexed on Au NP **5**•Zn^{2+} without having a large excess of receptor free in solution.

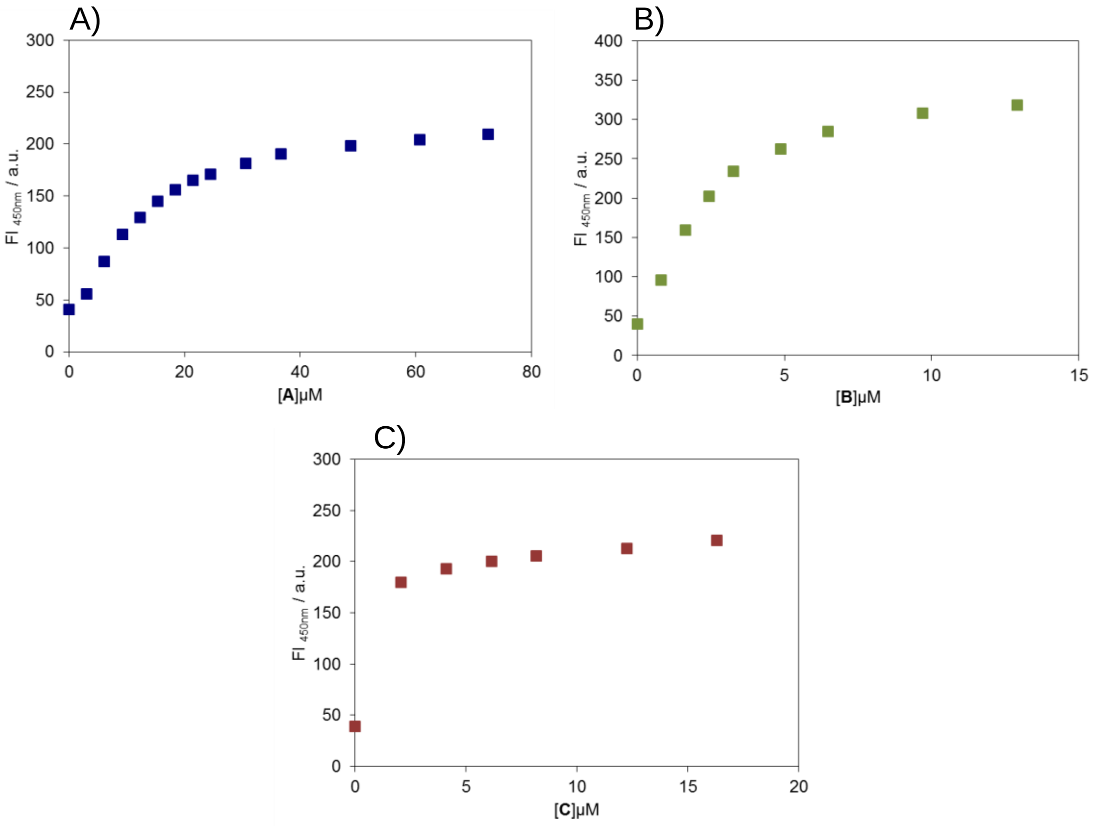

Figure 3.9. Fluorescence intensities as a function of the amount of (A) **A** (B) **B** (C) **C** added to a solution of [Au NP **5**•Zn^{2+}] = 20 µM and [**dATP$_{MANT}$**] = 5 µM, [HEPES] = 10 mM, pH 7.0, 37 °C, slit 10/10 nm.

3.2.3. Selectivity studies

The ability of the system to detect small molecules was tested on a library of small biologically relevant molecules of comparable structure.

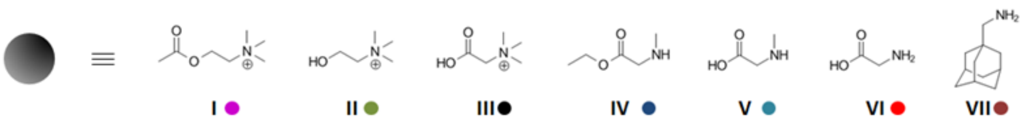

Figure 3.10. Library of small molecules: **I** acetylcholine, **II** choline, **III** betaine, **IV** sarcosine ethyl ester, **V** sarcosine, **VI** glycine, **VII** 1-Adamantanemethylamine

Choline and its metabolites acetylcholine and betaine are very important compounds in biology. Indeed, they have three main physiological purposes: structural integrity and signalling roles for cell membranes, cholinergic neurotransmission (acetylcholine synthesis), and a major source for methyl groups *via* trimethylglycine (betaine), which participates in the Sadenosylmethionine (SAMe) synthesis pathways. Glycine is as a precursor to proteins, such as its periodically repeated role in the formation of the collagen helix in conjunction with hydroxyproline, but it can act as an inhibitory neurotransmitter in the central nervous system, especially in the spinal cord, brainstem, and retina. The reason of the choice of sarcosine and its derivative was due to the appearance of a recent study, proposing sarcosine as biomarker of the aggressive forms of prostate cancer.[12] 1-Adamantanemethylamine was taken as analyte for its similarity with rimantadine, an antiviral drug, used to treat, and in rare cases prevent, infections.

The selectivity studies of the different systems containing either **A** or **B** or **C** were carried out following the changes of FI with respect to time. Firstly, 5 μM of **dATP$_{\mathbf{MANT}}$** was added to a solution containing Au NP **5**•Zn^{2+} and the system was left to equilibrate for 10 minutes. Then, one of the three hosts **A** (5.8 μM), **B** (6.5 μM) or **C** (6.15 μM) was added to the solution and the mixture was equilibrated until the fluorescent signal stabilised (10 minutes). Subsequently, after the addition of 100 μM of each guest of the library, the signal was followed for 20 minutes (Figure 3.11). This concentration was chosen in order to favour the shift of the equilibrium towards the formation of the complex.

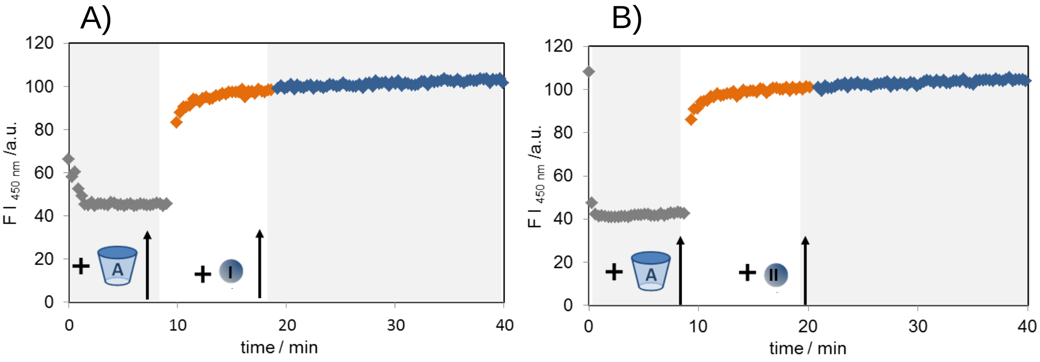

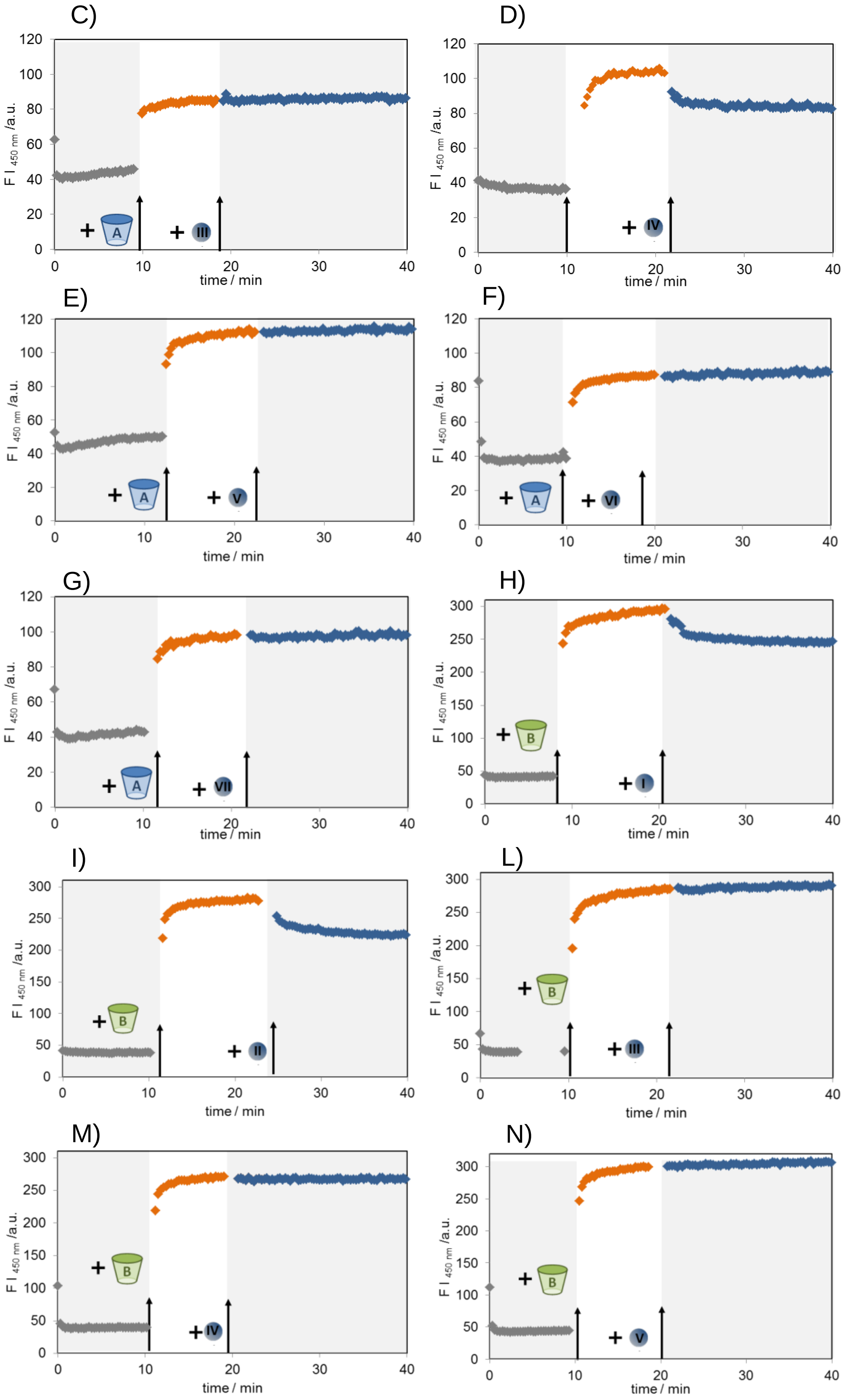
C)
+ A
+ III
D)
+ IV
E)
+ A
+ V
F)
+ A
+ VI
G)
+ A
+ VII
H)
+ B
+ I
I)
+ B
+ II
L)
+ B
+ III
M)
+ B
+ IV
N)
+ B
+ V
F I 450 nm /a.u.
time / min
0
10
20
30
40
0
20
40
60
80
100
120
0
50
100
150
200
250
300

O)

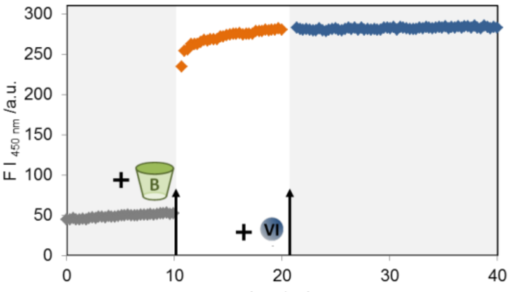
300
250
200
150
100
50
0
0
10
20
30
40
F I 450 nm /a.u.
time / min
+ B
+ VI

P)

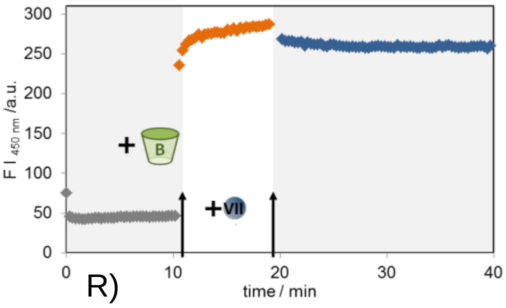
300
250
200
150
100
50
0
0
10
20
30
40
F I 450 nm /a.u.
time / min
+ B
+ VII

Q)

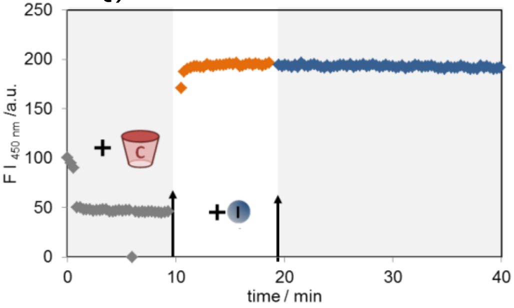
250
200
150
100
50
0
0
10
20
30
40
F I 450 nm /a.u.
time / min
+ C
+ I

R)

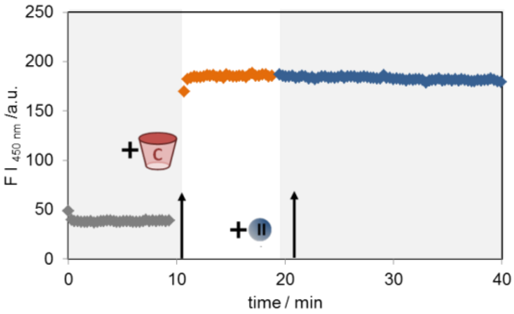
250
200
150
100
50
0
0
10
20
30
40
F I 450 nm /a.u.
time / min
+ C
+ II

S)

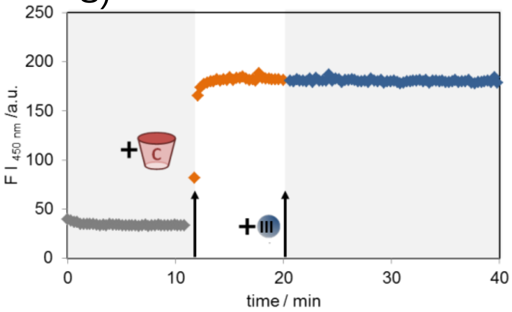
250
200
150
100
50
0
0
10
20
30
40
F I 450 nm /a.u.
time / min
+ C
+ III

T)

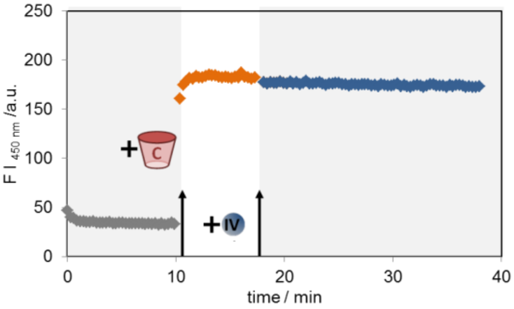
250
200
150
100
50
0
0
10
20
30
40
F I 450 nm /a.u.
time / min
+ C
+ IV

U)

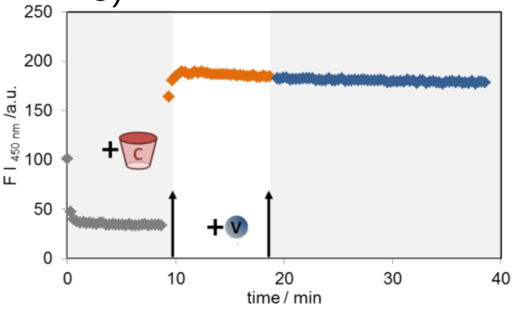
250
200
150
100
50
0
0
10
20
30
40
F I 450 nm /a.u.
time / min
+ C
+ V

V)

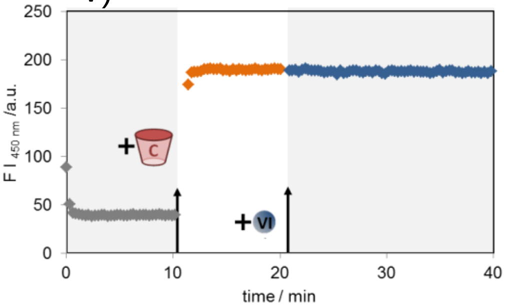
250
200
150
100
50
0
0
10
20
30
40
F I 450 nm /a.u.
time / min
+ C
+ VI

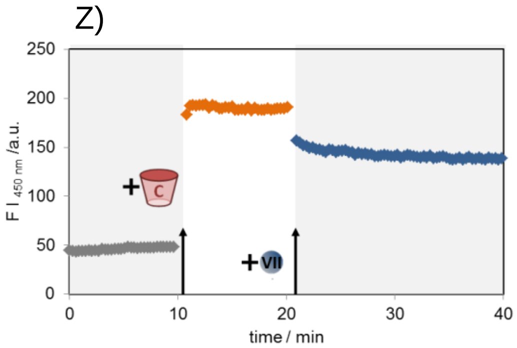

Figure 3.11. Fluorescence kinetics of the experiment used to determine the selectivity of the assay for each combination of receptor **A**-**C** and analyte **I**-**VII**. Addition of the receptor **A** (A-G) to Au NP **5**•Zn^{2+} saturated with the fluorescent probe $dATP_{MANT}$ causes a (partial) displacement of the probe from the surface. Subsequently, analyte (A) **I**, (B) **II**, (C) **III**, (D) **IV**, (E) **V**, (F) **VI** (G) **VII** is added and the change in fluorescence intensity is measured. The above was repeated for receptor **B** (H-P) and **C** (Q-Z). All measurements were performed as kinetics in order to ensure that final equilibrium values were reached. [Au NP **5**•Zn^{2+}] = 20 μM and [$\mathbf{dATP_{MANT}}$] = 5 μM, [**A**]= 5.8 μM, [**B**] = 6.5 μM, [**C**] = 6.15 μM, [HEPES] = 10 mM, pH 7.0, 37 °C. The instrument settings were those of 3.3. 2

The selectivity of the three different systems is summarized in Fig. 3.12. As reported in the literature,[13] tetrasulfonate calix[4]arene **B** interacts with quaternary ammonium cations like choline (**II**) and acetylcholine (**I**) and can slightly interact with 1-adamantane methylamine (**VII**), which is protonated at this pH. In the same way the phosphonate cavitand **A** permits the detection of mono methylated amines[15] thanks to the complementarity of hydrogen bonds, $N^{+}\cdots\cdots O=P$ cation dipole interactions and the CH-Π interactions that occur between the methyl group of the analyte and the Π system present in the host. The presence of heptakis(6-O-sulfo)-β-cyclodextrin **C** permits the formation of an inclusion complex with the adamantane derivative (**VII**). In addition, the dose-response curve revealed a clear correlation between the amount of guest added (10-2000 μM) and the extent of signal change (Figure 3.12 D-F). These curves also showed that analyte concentrations down to around 50 μM were sufficient to generate a detectable signal. These results show that the selectivity of the assay is determined by the selective interaction between the macrocyclic receptor and the analyte.

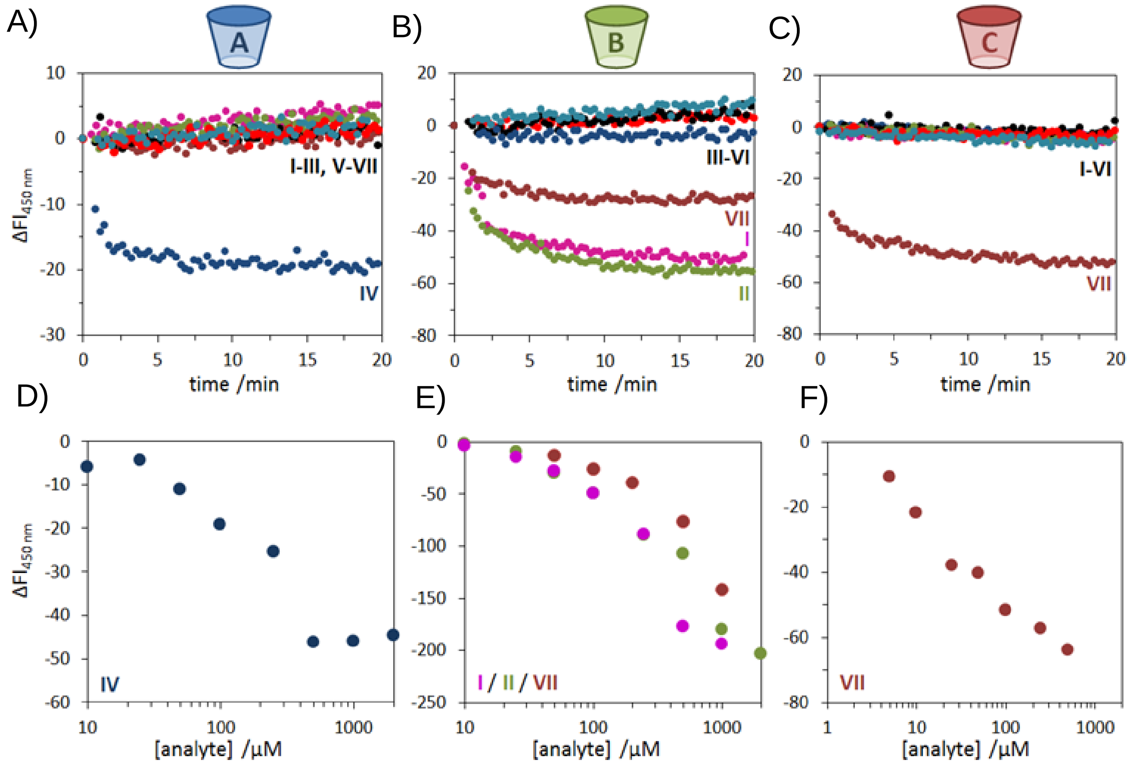

Figure 3.12. Changes in the fluorescence intensity (450 nm) as a function in time upon the addition of analytes **I**–**VII** to solutions containing AuNP **5** (20 µM), probe **dATP$_{\mathbf{MANT}}$** (5 µM) and either (A) receptor **A** (5.8 µM), (B) receptor **B** (6.5 µM), or (c) receptor **C** (6.15 µM). (D-E). Changes in the fluorescence intensity (450 nm) measured 20 minutes after the addition of increasing amounts of analytes (indicated in the figure) to solutions containing Au NP **5** (20 µM), probe **dATP$_{\mathbf{MANT}}$** (5 µM) and either (D) receptor **A** (5.8 µM), (E) receptor **B** (6.5 µM), or (F) receptor **C** (6.15 µM). Experimental conditions: [HEPES]=10 mM, pH 7.0, 37 °C. HEPES: 4-(2-hydroxyethyl)-1-piperazineethanesulfonic acid.

3.2.4. Screening in biological medium

An application in the area of biodiagnostics requires the assay to function also in complex media with a high content of salts and small molecules. To explore the tolerance of the assay to the presence of such potentially interfering compounds, we performed a series of experiments in synthetic urine (SURINE™), which contains all major components of human urine and is used as a negative control in urine analysis. In particular we focused our studies on the assay containing receptor **A**, because of its reported ability to detect sarcosine (**V**) in acidified human urine. The studies, reported in buffered solution at pH 7.0 (Figure 3.12), had shown that the assay containing phosphonate cavitand was able to detect sarcosine ethyl ester (**IV**) but not sarcosine. It can be observed (Figure 3.13 A) that the addition of **IV** to an equilibrated solution of Au NP **5**•Zn^{2+}, **dATP$_{MANT}$**, and **A** in synthetic urine also caused a significant decrease in fluorescence intensity, albeit lower in intensity compared to the studies performed in buffer. The dose-response curve confirmed that the decrease resulted indeed from complex formation between **A** and **IV** (Figure 3.13 B). A repetition of the experiment using the other analytes showed that the selectivity of the assay was maintained. However, we also observed that the addition of sarcosine (**V**) at 200 μM seemed to cause a small decrease in fluorescence intensity. This prompted us to measure the assay response at higher sarcosine concentrations (up to 1.5 mM), which confirmed the assay response to sarcosine. The improved response of the assay to sarcosine in synthetic urine, as compared to aqueous buffer, is not entirely clear and is currently under investigation. Importantly, these results demonstrate the tolerance of the assay towards high concentrations of salts, monocharged anions, and small molecules. This tolerance is in line with previously reported data and can be attributed to the strength of the multivalent interactions between oligoanions (such as **A** and **dATP$_{MANT}$**) and the monolayer surface of Au NP **5**•Zn^{2+}.[16]

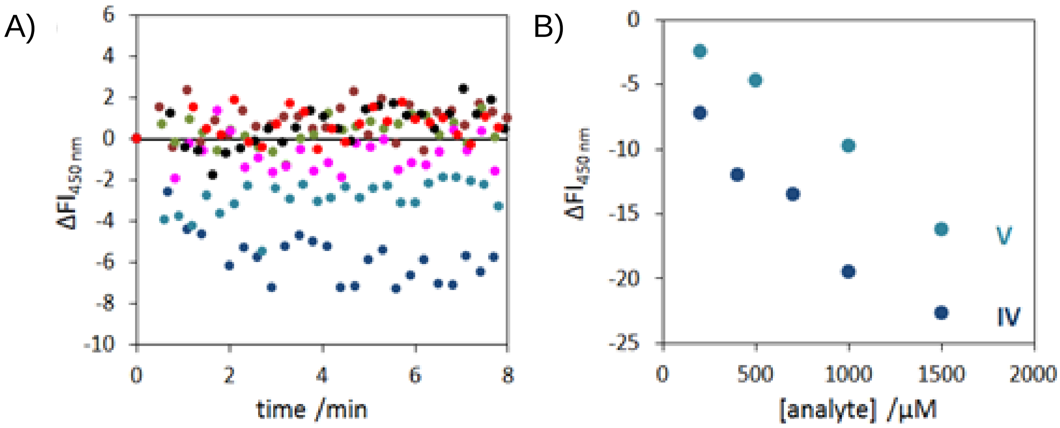

Figure 3.13. A) Changes in the fluorescence intensity (450 nm) as a function in time upon the addition of analytes **I–VII** (200 μM) to a solution of synthetic urine (SURINE^{TM}) containing Au NP **5**•Zn^{2+} (20 μM), probe dATP$_{MANT}$ (5 μM) and receptor **A** (5.8 μM). B) Changes in the fluorescence intensity (450 nm) measured 10 minutes after the addition of increasing amounts of analytes **IV** and **V** to a solution of synthetic urine (SURINE^{TM}) containing Au NP **5**•Zn^{2+} (20 μM), probe **dATP$_{MANT}$** (5 μM) and receptor **A** (5.8 μM).

Following the same procedure, the screening of guests **II**, **IV**, **VII**, in presence of host **B**, in Surine™ was performed, confirming the selective detection of compound **II**. This experiment confirmed us that the selectivity of the assay is maintained, also, in biological medium (Figure 3.14).

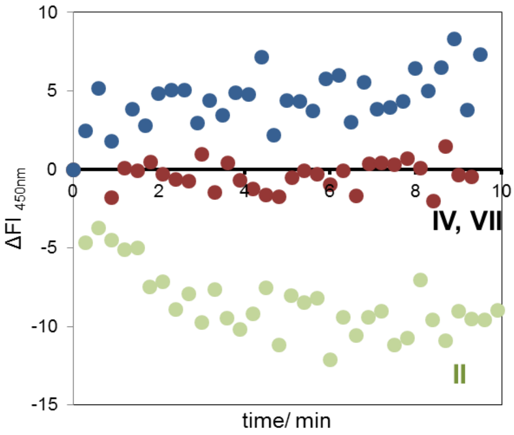

Figure 3.14. Changes in the fluorescence intensity (450 nm) as a function of time upon addition of **II**, **IV**, **VII** to solutions containing Au NP **5**•Zn^{2+} (20 µM), probe **dATP$_{MANT}$** (5 µM) and receptor **B** (6.5 µM).

3.2.5. Modularity

One of the advantages of the reported assay is its modularity. The possibility to tune the selectivity of the assay just by changing the anionic host independently from the indicator prevents any other synthetic effort. Furthermore, it also creates the possibility of sensing multiple analytes with a single assay. Generally, sensing systems able to detect multiple analytes generate a pattern of signals that act as a fingerprint for a given analyte. These systems typically have a rather low selectivity, which permits numerous analytes to interact with the receptor units and generate a response. The drawback of this approach is that statistical treatment of the output signals (such as principal component analysis (PCA) or linear component analysis (LDA)) is required to correlate the output signal to the analyte. This implies that the system needs to be 'trained' to recognize the fingerprints of each analyte. The application of these systems is particularly challenging in case mixtures of analytes are used. We argued that the simultaneous use of receptors **A–C** in combination with AuNP **5**•Zn^{2+} and **dATP$_{MANT}$** would lead to a single system able to detect multiple analytes, but, as opposed to the systems discussed above, with a high selectivity. Thus, we prepared an equilibrated solution containing all components and measured the response of the system to the subsequent additions of analytes **II**, **IV**, and **VII**, which were shown to interact with receptors **B**, **A**, and **C**, respectively. Concentrations were chosen such that the formation of each analyte-receptor complex would cause a comparable change in fluorescence intensity. After each addition, the output signal (FI at 450 nm) was measured in time in order to ensure that the system had reached equilibrium before the subsequent analyte was added. We were pleased to observe that each analyte caused a significant change in the output signal, which indeed demonstrated the capacity of the sensing system to respond to multiple analytes (Figure 3.15).

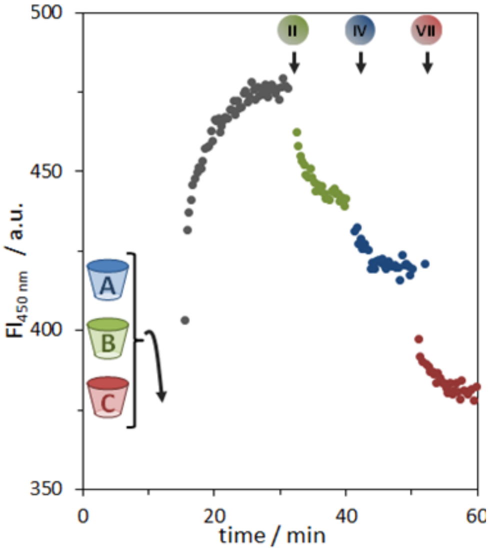

Figure 3.15. Fluorescence intensity (450 nm) as a function of time upon the successive additions of analytes **II** (200 μM), **IV** (200 μM) and **VII** (100 μM) to a solution containing Au NP **5**•Zn^{2+} ([Au NP **5**•Zn^{2+}] = 60 μM), **dATP$_{MANT}$** (15 μM) and receptors **A**–**C** (5.8 μM, 6.5 μM and 6.2 μM, respectively)

However, in order to demonstrate that the response induced by each analyte resulted from a selective interaction with the respective receptor, we proceeded with a study of the systems response in case one or more receptors **A**–**C** were systematically removed. Firstly, we tested the systems presenting just one of the three hosts **A**, **B** or **C** (Figure 3.16). To a buffered solution (HEPES pH = 7, 37 °C), AuNP **5**•Zn^{2+} and **dATP$_{MANT}$** were added. The system was left to equilibrate for 10 minutes. Then, the corresponding host was added (**A** or **B** or **C**). After the stabilization of the signal (about 20 minutes), choline was added and the FI was measured for 10 minutes. Afterwards sarcosine ethyl ester (**IV**) was added to the solution and the signal was again measured for 10 minutes.

Finally, 1-adamantanemethylamine was added and the value of the FI was measured for 10 minutes.

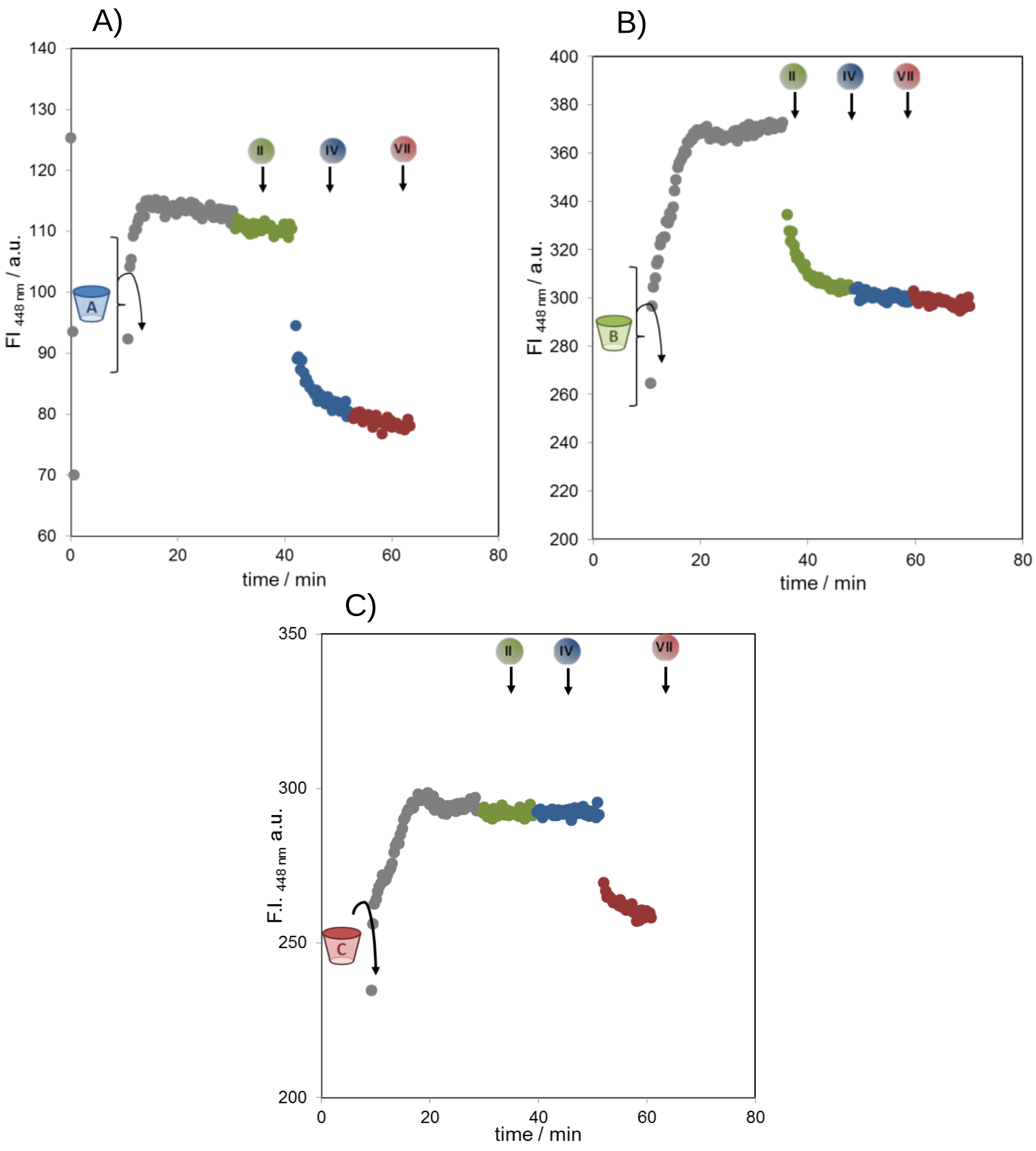

Figure 3.16. Fluorescence intensity (450 nm) as a function of time upon the successive additions of analytes **II** (200 μM), **IV** (200 μM) and **VII** (100 μM) to a solution containing (A-C) Au NP **5**•Zn^{2+} (20 μM), **dATP$_{MANT}$** (5 μM) and one of the receptors (A) **A** (5.8 μM), (B) **B** (6.5 μM) or (C) **C** (6.15 μM).

The same protocol was followed for the systems presenting the combination of two of the three guests (**A** and **B**, **A** and **C**, **B** and **C**, Figure 3.17).

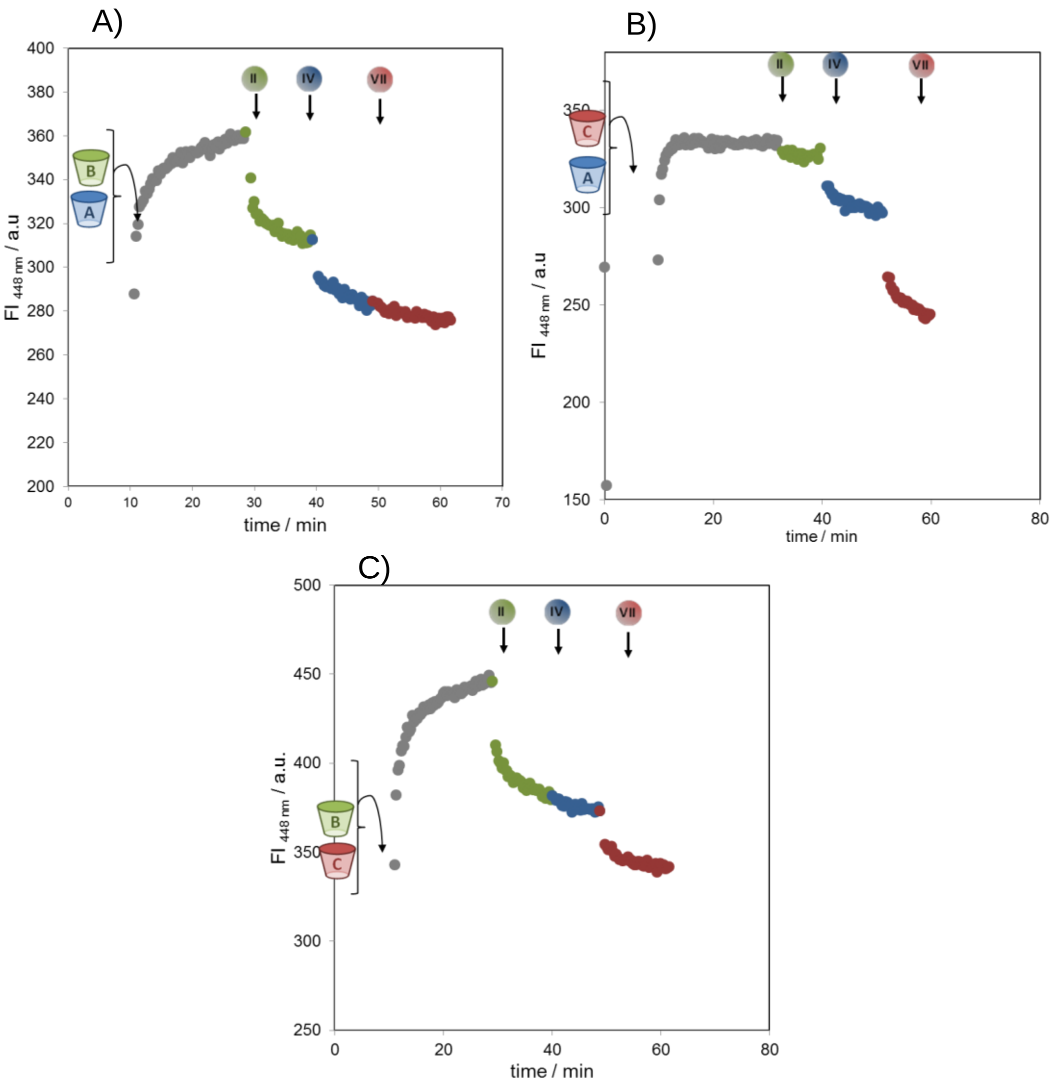

Figure 3.17. Fluorescence intensity (450 nm) as a function of time upon the successive additions of analytes **II** (200 μM), **IV** (200 μM) and **VII** (100 μM) to a solution containing (a-c) Au NP **5**•Zn^{2+} (40 μM), **dATP$_{MANT}$** (10 μM) and receptors (a) **A** (5.8 μM) and **B** (6.5 μM), (b) **A** (5.8 μM) and **C** (6.15 μM), (c) **B** (6.5 μM) and **C** (6.15 μM);

The control experiment was done by performing the subsequent addition of the three guests in the absence of host to demonstrate that the guests alone cannot influence the affinity of **dATP$_{MANT}$** for the surface (Figure 3.18).

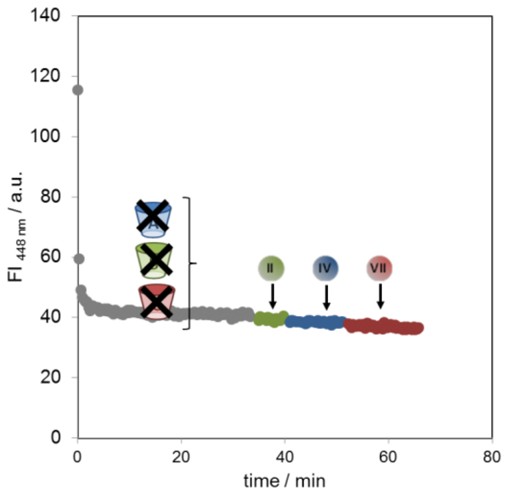

Figure 3.18. Fluorescence intensity (450 nm) as a function of time upon the successive additions of analytes **II** (200 μM), **IV** (200 μM) and **VII** (100 μM) to a solution containing Au NP **5**•Zn^{2+} (20 μM), **dATP$_{MANT}$** (5 μM) and no receptors.

Two important conclusions could be drawn from the obtained results. First, a neat correlation was observed between the presence of a given receptor (**B**, **A**, or **C**) and the ability of the analyte (**II**, **IV**, and **VII**, respectively) to create a positive response. For example, in the absence of any receptor no signal change was observed after any of the three additions (Figure 3.18). It is noted that the addition of analyte **VII** to the system containing just receptor **B** did not provide a positive response, contrary to what observed during the individual studies (Figure 12). This originates from the fact that analyte **VII** was added after analyte **II** and at lower concentrations (to tune the response of the system). Given the higher affinity of **II** for receptor **B** compared to **VII** (Figure 3.12 B), this makes that the formation of the complex between **B** and **II** suppresses the interaction between **B** and **VII**. The second feature of the system is the observed orthogonality of the interactions between receptors **A** – **C** and their respective analytes.

Considering the versatility and efficacy of the modular approach, we show that the simultaneous use of different recognition modules gives the possibility to interpret the assay output signal as the result of a 3-bit molecular computing system. The use of three receptors implies that eight different combinations can be created, including the system in which none of the receptors is present. A change of 10 arbitrary units (a.u.) in the fluorescence intensity after each analyte addition was taken as a threshold value to differentiate between a positive or a negative response. The threshold value was taken well above the normal fluctuation of the fluorescence signal (± 5 a.u.) under these conditions. Two important conclusions could be drawn from the obtained results. First, a neat correlation was observed between the presence of a given receptor (**B**, **A**, or **C**) and the ability of the analyte (**II**, **IV**, and **VII**, respectively) to create a positive response. The second feature of the system is the observed orthogonality of the interactions between receptors **A–C** and their respective analytes.

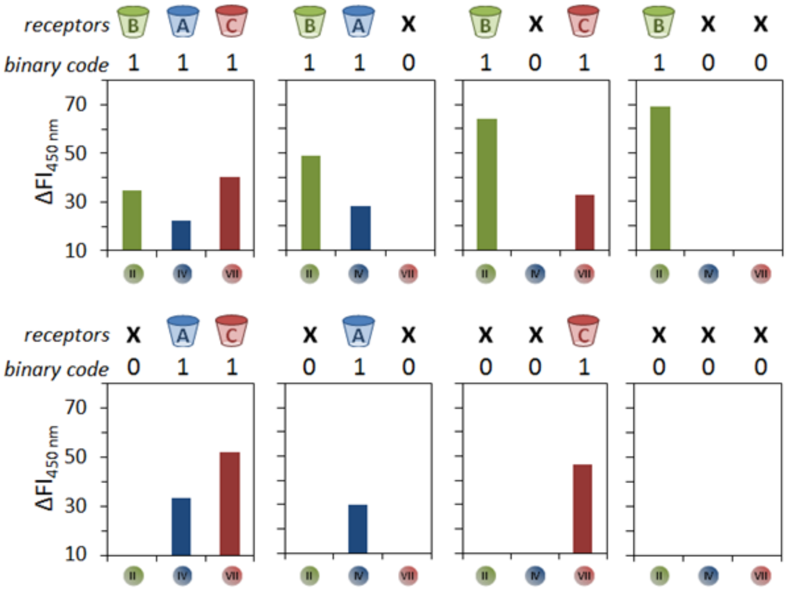

Figure 3.19. Assay response as a function of the presence/absence of receptors **A**–**C**. The fluorescence value of 10 a.u. is taken as a threshold-value to differentiate between a positive (1) or negative (0) response. Experimental conditions: [HEPES] = 10 mM, pH 7.0, 37 °C.

3.2.6. Signal amplification

There are various molecular approaches towards signal amplification in which a single analyte molecule affects the properties of a multitude of reporter molecules. The ability of a catalyst to convert a multitude of substrate molecules into products (defined by the turn over number) makes a catalyst an intrinsic signal amplifier in case the chemical conversion of the substrate is accompanied by a measurable change in physical properties. For sensing purposes, catalytic activity must depend on the interaction between the analyte and the catalyst.[18] It is reported that Au NP **5**•Zn^{2+} can catalyze the transphosphorylation reaction of 2-hydroxypropyl-4-nitrophenyl phosphate (HPNPP **13**), producing *p*-nitrophenolate, detectable by UV-Vis spectroscopy. Indeed, the spontaneous formation of multiple bimetallic catalytic sites due to the multivalency of the surface is capable of promoting the cleavage of this RNA model substrate.[19] It is possible to modulate the activity of Au NP **5**•Zn^{2+} through competition between the HPNPP and anionic probes, which leads to an alternative method to evaluate the relative affinity of these anionic probes for the nanoparticle surface. Indeed, oligo anions with high affinity for the surface of AuNP **5**•Zn^{2+} can completely inhibit the catalysis.

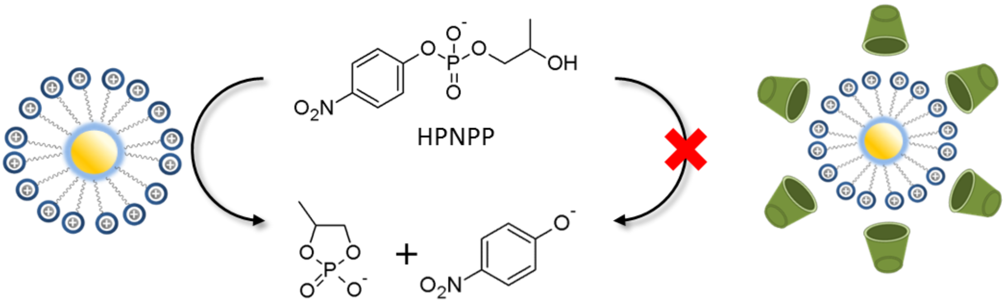

Figure 3.20. Schematic representation of the catalytic activity of Au NP **5**•Zn^{2+}.

In a preliminary stage, we wanted to determine to which extent host **B** would compete for the surface of Au Au NP **5**•Zn^{2+} **5** with the substrate. The affinity studies of tetrasulfonate calix[4]arene were carried out by measuring the catalytic activity in the presence of increasing amounts of **B**.

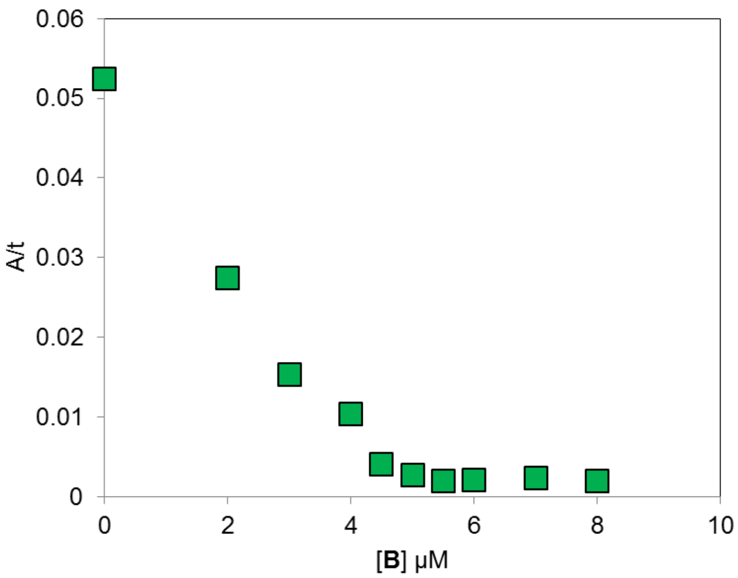

Figure 3.21.The curve A_{405nm} [tetrasulfonate calix[4]arene] demonstrate that 5 μM of host is sufficient to completely inhibit the catalysis of HPNPP. [Au NP **5**•Zn^{2+}] = 20 μM, [**13**] = 1 mM, [HEPES] = 10 mM, pH 8.0, 37 °C.

It is clear that the catalytic activity of the system depends on the accessibility of catalytic sites on the monolayer surface. Since our previous studies had shown that guest complexation by host **B** causes a decrease in the affinity for Au NP, we wondered whether this would also have an effect on the catalytic activity of the system. For that purpose we measured the catalytic activity in the presence of a fixed amount of host (5.5 μM) and guest (100 μM) complex, using the conditions employed in the fluorescence displacement studies.

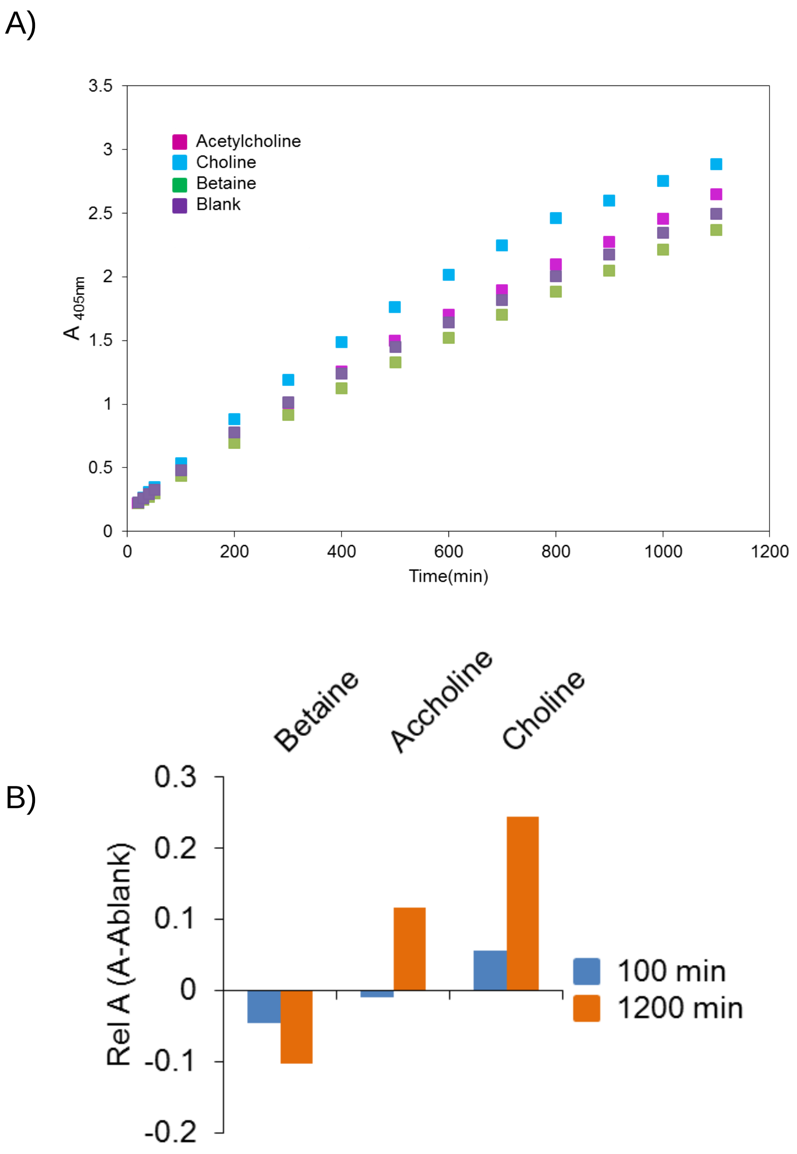

Figure 3.22. A) Kinetic curves of the catalysis of HPNPP in presence of [tetrasulfonate calix[4]arene] = 5.5 µM and [guest] = 100 µM. [Au NP **5**•Zn^{2+}] = 20 µM, [**13**] = 1 mM, [HEPES] = 10 mM, pH 8.0, 37 °C. B) Relative absorbance measured after 1200 min

From the kinetic curves it is possible to note that the presence of both choline and acetylcholine caused a slight increase in catalytic activity. These results are consistent with those reported in paragraph 3.2.3, indicating that the complexes formed by choline and acetyl choline with **A** presented a lower affinity for the surface compared with the affinity of **A** alone. The advantage of catalytic signal amplification becomes evident when longer time intervals are used for signal generation. Indeed, after 1200 minutes the difference in absorbance had increased from 0,5% after 100 min to 9.3% after 1200 min for choline and from

% (at 100 min) to 4.3% (1200 min) for acetylcholine (compared to the blank, Figure 3.22 B).

Based on these promising initial results we then investigated whether it would be possible to increase the rate of the catalysis in order to obtain signal amplification in a shorter time. Bearing in mind that the binding of anionic species on the surfaces of Au NP **5**•Zn^{2+} is sensitive to subtle changes in the molecular structure, we reasoned that, by tailoring the structure of HPNPP, it would be possible to create more competitive substrates towards highly charged oligo anions. Previous work in our group had led to the synthesis of the molecule 2-hydroxypropyl 3-trifluoromethyl-4-nitrophenyl phosphate (HPNP-$\mathbf{CF_3}$ (**14**)) which possesses 3-trifluoromethyl-4-nitrophenol as the leaving group. The presence of the trifluoromethyl moiety in position 3 of the phenol ring decreases the acidity of the leaving group, while assuring a higher hydrophobic contribution to the overall molecular structure. As a consequence, **14** has a higher k_{cat} and a lower K_M value compared to the original substrate **13**.

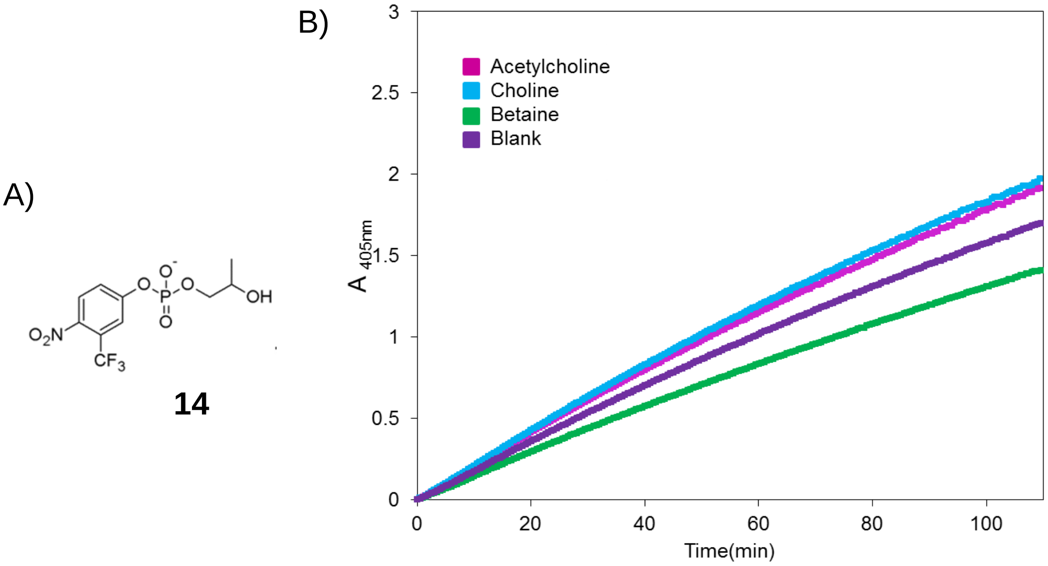

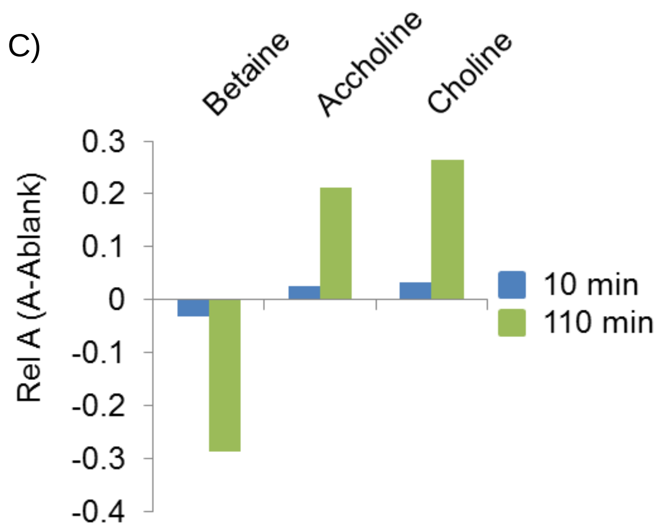

Figure 3.23. A) Chemical structure of the substrate **CF**$_3$ B) Kinetic curves of the catalysis of **14** in presence of [tetrasulfonate calix[4]arene] = 5.5 µM and [guest] = 100 µM. [Au NP 5•Zn^{2+}] = 20 µM, [**14**]= 1 mM, [HEPES] = 10 mM, pH 8.0, 37 °C. C) Relative absorbance measured after 110 min

Also in this case, the presence of the guest affected the catalytic activities of Au NP **5**•Zn^{2+} when host **A** was present The use of HPNP-**CF3** (**14**) permits to obtain the same increase in output signal as compared to HPNP, but in less time. Moreover, after 110 min we observed an increase in absorbance of 15% for acetylcholine and 19% for acetylcholine compared to the blank.

It was also surprising to observe a difference, although small, between choline and acetylcholine. Indeed, previous studies by Nau and co-workers had shown that receptor sulfonatocalix[4]arene is unable to discriminate between these two analytes.[20] It is also interesting to observe that the presence of betaine cannot interact with the host, reducing the catalysis if compared to the host alone. This can be ascribed to the presence of a negative charge on the guest that can allow its interaction with the monolayer acting as additional inhibitor.

3.3. CONCLUSIONS

In conclusion, we have developed a modular sensing system that can be tuned to selectively detect the presence of one or more analytes. The assay relies on the change in affinity of anionic macrocyclic receptors **A–C** for Au NP **5**•Zn^{2+}

upon complexation of the respective analytes. At difference with related nanoparticle based sensing systems, the assay is analyte-selective which implies that the output signal directly informs on the presence or not of the analyte without the need to perform statistical data treatment such as LDA or PCA. The modularity of the system implies that the assay selectivity can be tuned simply by changing the recognition module, leaving all other components unvaried. Considering the availability of a large number of macrocyclic receptors similar to **A–C** (for example, α-, β-, and γ-cyclodextrins and calix[*n*]arenes with *n* = 4-8) each with their own substrate selectivity, we are convinced that this system can be easily extended to the detection of other analytes. The multivalent nature of the interactions with the monolayer surface of Au NP **5**•Zn^{2+} make the assay tolerant for the presence of salts and small molecules. It has been shown that different recognition modules can be integrated in the same system, yielding a single assay that can detect multiple analytes in a controlled manner. A study of the orthogonality of the different receptor-analyte couples led to the demonstration of the possible exploitation of this kind of arrays within the context of molecular computing. The integration of the current system (3 bit) with additional recognition modules should in principle permit the development of a molecular byte.

3.4. EXPERIMENTAL SECTION

3.4.1. Materials and methods

The synthesis and characterization of Au NP **5**•Zn^2 has been described elsewhere.[11] The stock solutions of Au NP **5**•Zn^2were stored at 4°C in mQ water. The concentration of TACN-head groups in Au NP **5**•$Zn^2$was determined from kinetic titrations using $Zn(NO_3)_2$ as reported previously.[16] $Zn(NO_3)_2$ was an analytical grade product. 2'-Deoxy-3'-O-(N'-methylanthraniloyl)adenosine-5'-O-triphosphate (**$dATP_{MANT}$**) was purchased from Biolog Life Science Institute and used as received. The buffer 4-(2-hydroxyethyl)-1-piperazineethanesulfonic acid (HEPES), heptakis(6-O-sulfo)-β-cyclodextrin heptasodium salt (**C**), acetylcholine chloride, choline chloride, betaine, glycine, sarcosine, sarcosine ethyl ester hydrochloride and 1-adamantanemethylamine were purchased from Sigma Aldrich and used without further purification. p-Sulfonatocalix[4]arene (**B**) was supplied by Tokyo Chemical Industry. SURINE™ was supplied by Dyna-Tek Industries. The concentration of **dATP$_{\mathbf{MANT}}$** was determined both by weight and UV-Vis spectroscopy using ε355 (MANT) = 5800 M^{-1} cm^{-1} at pH 7 as the extinction coefficient. The concentration of **B** was determined both by weight and ^{1}H-NMR, using pyrazine as internal standard. Both concentrations of **A** and **C** were determined by weight. All the compounds were dissolved in mQ water and freshly prepared except for **A** and 1-adamantanemethylamine that were respectively dissolved in a 5:2 mixture of H_2O:MeOH and a 5:1 mixture of H_2O:MeOH.

UV-Vis spectra were recorded on a Varian Cary50 spectrophotometer equipped with thermostatted multiple cell holders. Fluorescence measurements were recorded on a Varian Cary Eclipse Fluorescence spectrophotometer equipped with a thermostatted cell holder.

3.4.2. Surface saturation concentration (SSC)

The SSC of **dATP$_{\mathbf{MANT}}$** on Au NP **5**•Zn^{2+} was determined as described previously[11] (λ_{ex} = 355 nm, λ_{em} = 448 nm, slit: 10/5 nm). After each addition, the fluorescence intensities were recorded after stabilization of the signal (typically 5 minutes). The value obtained was determined via extrapolation of the linear part of the curve (5 points). The SSC of **dATP$_{\mathbf{MANT}}$** on Au NP **5**•Zn^{2+} (20 µM) was estimated to be around 5 µM.

3.4.3. Displacement experiments

The displacement experiments were performed by measuring the fluorescent intensities after adding consecutive amounts of a stock solution of the three receptors **A**, **B** and **C** to a 3 mL buffered solution (HEPES 10 mM, pH = 7.0) containing Au NP **5**•Zn^{2+} (20 µM) covered with the fluorophore **dATP$_{\mathbf{MANT}}$** (5 µM) (λ_{ex} = 355 nm, λ_{em} = 448 nm, slit: 10/10 nm). The fluorescent intensities generated by the addition of small additional amounts of **A**, **B** and **C** to the above-described solution, were registered after the stabilization of the signal. The curves reached a plateau that does not correspond to the maximum FIs expected for a full release of the probe. In Figure 9, the curves FI/[HOST] are shown, allowing the evaluation of the optimal concentration of the host to give the highest displacement of the probe.

3.4.4. Selectivity studies in buffered solution

The concentrations of the solutions of the guests were prepared by weight. The selectivity of the three separate systems was carried out following the changes of FI with respect to time. The experiments were performed in buffered solution (HEPES 10 mM pH = 7). At the beginning, $\mathbf{dATP_{MANT}}$ (5 µM) was added to a solution containing Au NP **5**•Zn^{2+} (20 µM). The system was left to equilibrate for 10 minutes (Signal OFF). Then, one of the three hosts **A** (5.8 µM), **B** (6.5 µM) or **C** (6.2 µM) was added to the solution and the mixture was equilibrated until stabilization of the fluorescent signal (10 minutes) (Signal ON). Finally, 100 µM of each guest of the library was added, monitoring the fluorescent signal for 20 minutes. A control experiment was carried out by adding analytes **II**, **IV** or **VII** to the system in the absence of the receptor.

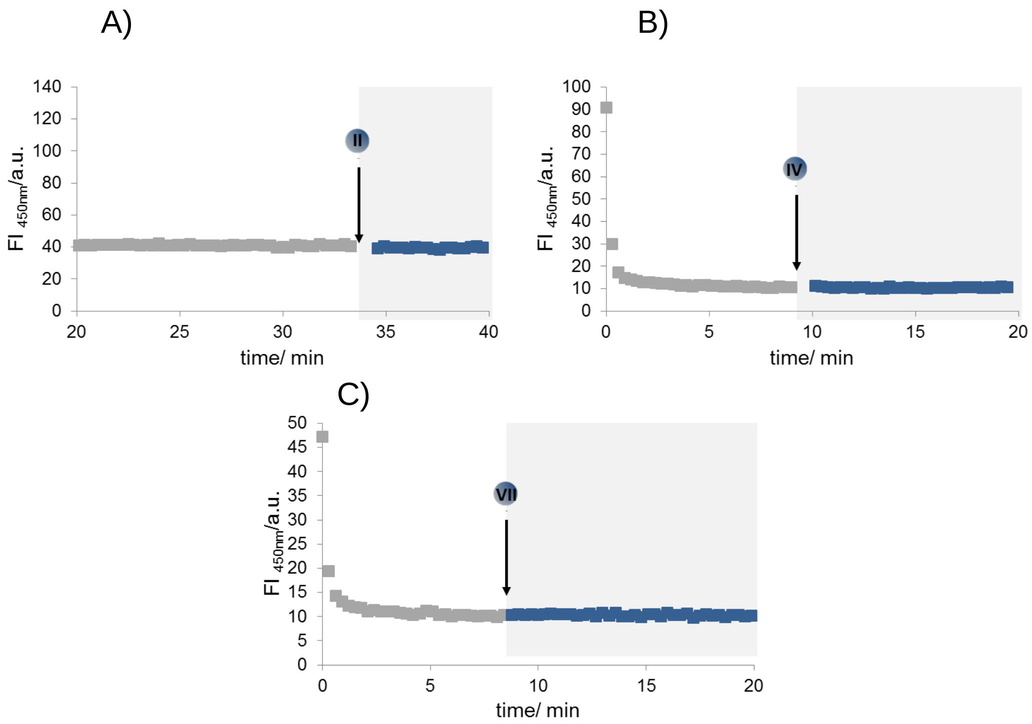

Figure S1. Fluorescence kinetics of control experiments. The addition of 100 μM of guest A) **II**, B) **IV**, c) **VII** to Au NP **5**•Zn^{2+}, saturated with the fluorescent probe dATPMANT, does not cause any change in florescent intensity. [AuNP **5**•Zn^{2+}] = 20 μM and [**dATP$_{\mathbf{MANT}}$**] = 5 μM, [HEPES] = 10 mM, pH 7.0, 37 °C. The instrument settings were those 5.2

3.4.5. Selectivity studies in Surine ®

The selectivity experiments were carried out in synthetic urine following the changes of FI with respect to time. To a solution of SURINE^{TM}, Au NP **5**•Zn^{2+} (20 μM) and **dATP$_{\mathbf{MANT}}$** (5 μM) were added. The signal was left to stabilize (for around 10 minutes) and host **A** (5.8 μM) was added. Subsequently, a screening of the guests (**I**-**VII**) was carried out following the change in fluorescence intensity after the addition of 200 μM of each guest. Following the same procedure, the screening of guest **II**, **IV**, **VII**, in presence of host **B** (6.5 μM), was performed.

3.4.6. Response curves

Following the protocol reported in 5.4, the kinetic curves of ΔFI/[Guests] were recorded at increasing concentration of guest in order to obtain the limit of detection of the assay and the linearity range of the systems.

Since the system with **B** as host is selective for three different guests (choline, acetylcholine and 1-adamantanemethylamine), three different response curves were obtained. The presence of host **A** selectively detects sarcosine ethyl ester and, in the same way, host **C** allows the detection of 1-adamantanemethylamine only.

3.4.7. Assay with multiple receptors

The assay was tested in the presence of different combinations of hosts on the surface following instrument settings reported in 5.2.

For systems presenting just one of the three hosts (100, 010, 001)

To a 3 mL buffered solution (HEPES pH = 7, 37 °C) containing Au NP **5**•Zn^{2+} (20 µM), **dATP$_{MANT}$** (5 µM) was added. The system was left to equilibrate for 10 minutes. Then, the corresponding host was added (**A**: 5.8 µM, **B**: 6.5 µM or **C**: 6.2 µM). After the stabilization of the signal (about 20 minutes), choline (**II**, 200 µM) was added and the FI was measured for 10 minutes. Then, sarcosine ethyl ester was added to the solution (**IV**, 200 µM) and the signal was followed for 10 minutes. Finally, 1-adamantanemethylamine (**VII**, 100 µM) was added and the FI was recorded.

For systems presenting two of the three hosts (110, 011, 101)

To a 3 mL buffered solution (HEPES pH = 7, 37°C), Au NP **5**•Zn^{2+} (40 µM) and **dATP$_{MANT}$** (10 µM) were added. Then, a combination of two of the three following hosts was added (**A**: 5.8 µM, **B**: 6.5 µM, **C**: 6.2 µM). Subsequently, the consecutive additions of the three guests were performed with choline (**II**, 200 µM), sarcosine ethyl ester (**IV**, 200 µM) and 1-adamantane-methylamine (**VII**, 100 µM). The timing of the additions was the same as above.

For the system presenting the three hosts at the same time (111)

To a 3 mL buffered solution (HEPES pH = 7, 37°C), Au NP **5**•Zn^{2+} (60 µM) and **dATP$_{MANT}$** (15 µM) were added. Then, all three hosts were added (**A**: 5.8 µM,

B: 6.5 µM and **C**: 6.2 µM). Subsequently, consecutive additions of the three guests were performed, with choline (**II**, 200 µM), sarcosine ethyl ester (**IV**, 200 µM) and 1-adamantanemethylamine (**VII**, 100 µM). The timing of the additions was the same as before.

For the system without any host (000)

To a 3 mL buffered solution (HEPES pH = 7, 37°C), Au NP **5**·Zn^{2+} (20 µM) and **dATP$_{\mathbf{MANT}}$** (5 µM) were added. Then, the subsequent additions of the three guests were carried out as explained before.

3.4.8. Catalytic signal amplification

The catalytic acivity of Au NP **5**•Zn^{2+} was measured by monitoring the release rate of PNP or TFM in different buffered solutions ([HEPES] = 10 mM, pH 8) containing Au NP **5**•Zn^{2+} (20 µM).

3.4.8.1. Inhibition studies

The inhibition of Au NP **5**•Zn^{2+} catalytic activity induced by **B** was studied measuring by UV-Vis the release of PNP at 405 nm. The kinetic was carried out at fixed amount of substrate [HPNPP] = 1mM and at increasing amount of **B** ([**B**] = from 0 to 8 µM), at 37°C. Then, the A/t was plotted as a function of [**B**], obtaining a complete inhibition of the system at 5,5 µM.

3.4.8.2. Sensing trough signal amplification

The catalytic activity of the system Au NP **5**•Zn^{2+} inhibited bin the presence of 5.5 µM of **B** was studied upon the addition of 100µM of guest **I, II** and **III.**

To a buffered solution ([HEPES] = 10 mM pH=8, 37°C) containing Au NP **5**•Zn^{2+}, [**B**] = 5.5µM, [**Guest**] (**I** or **II** or **III)**, a fixed amount of substrate was added [HPNPP] (or **CF3**) = 1mM was added and the UV-Vis signal at 405 nm (PNP) or 392 nm (TFM) was followed.

3.5. BIBLIOGRAPHY

1. Silva, A. Molecular Fluorescent Signalling with ’Fluor-Spacer-Receptor‘ Systems: Approaches to Sensing and Switching Devices via Photophysics. *Chem. Soc. Rev.* **21,** 187–195 (1992).
2. Wiskur, S. L., Ait-Haddou, H., Lavigne, J. J. & Anslyn, E. V. Teaching old indicators new tricks. *Acc. Chem. Res.* **34,** 963–972 (2001).
3. Bell, T. W. & Hext, N. M. Supramolecular optical chemosensors for organic analytes. *Chem. Soc. Rev.* **33,** 589–598 (2004).
4. Anslyn, E. V. Supramolecular Analytical Chemistry. *JOC*. **72,** 687–699 (2007).
5. Nguyen, B. T. & Anslyn, E. V. Indicator-displacement assays. *Coord. Chem. Rev.* **250,** 3118–3127 (2006).
6. Saha, K., Agasti, S. S., Kim, C., Li, X. & Rotello, V. M. Gold nanoparticles in chemical and biological sensing. *Chem. Rev.* **112,** 2739–2779 (2012).
7. Das, J., Cederquist, K. B., Zaragoza, A., Lee, P. E., Sargent, E. H.,Kelley, S. O. An ultrasensitive universal detector based on neutralizer displacement. *Nat. Chem.* **4,** 642–648 (2012).
8. Xia, F., Zuo, X., Yang, R., Xiao, Y., Kang, D., Vallée-Bélisle, A., Gong, X., Yuen, J., Hsu, B. B. Y., Heeger, A. J., Plaxco, K. W. Colorimetric detection of DNA, small molecules, proteins, and ions using unmodified gold nanoparticles and conjugated polyelectrolytes. *Proc. Natl. Acad. Sci. U. S. A.* **107,** 10837–10841 (2010).
9. Ikeda, M., Tanida, T., Yoshii, T., Kurotani, K., Onogi, S., Urayama, K., Hamachi, I. Installing logic-gate responses to a variety of biological substances in supramolecular hydrogel-enzyme hybrids. *Nat. Chem.* **6,** 511–8 (2014).
10. Pieters, G., Pezzato, C. & Prins, L. J. Reversible control over the valency of a nanoparticle-based supramolecular system. *J. Am. Chem. Soc.* **134,** 15289–92 (2012).
11. Pieters, G., Cazzolaro, A., Bonomi, R. & Prins, L. J. Self-assembly and selective exchange of oligoanions on the surface of monolayer protected Au nanoparticles in water. *Chem. Commun.* **48,** 1916–8 (2012).
12. Sreekumar, A. Poisson, L. M., Rajendiran, T. M., Khan, A. P., Cao, Q., Yu, J., Laxman, B., Mehra, R., Lonigro, R.,J. Li, Y., Nyati, M., K. Ahsan, A., Kalyana-Sundaram, S., Han, B., Cao, X., Byun, J., Omenn, G., S. Ghosh, D., Pennathur, S., Alexander, D. C., Berger, A., Shuster, J. R., Wei, J. T., Varambally, S., Beecher, C., Chinnaiyan, A. M. Metabolomic profiles delineate potential role for sarcosine in prostate cancer progression. *Nature* **457,** 910–914 (2009).
13. Taylor, P. Lehn, J., Meric, R., Vigneron, J., Cesario, M., Pascard, C., Asfari, Z., Vicens, J. Binding of acetylcholine and other quaternary ammonium cations by sulfonated calixarenes . *Crystal structure*. **5**, 97–103 (2006).
14. Arena, G., Cali, R., Lombardo, G. G., Rizzarelli, E., Sciotto, D., Ungaro,

R., Casnati, A. Water soluble calix[4]arenes. A thermodynamic investigation of proton complex formation. *Supramol. Chem.* **1,** 19–24 (1992).

15. Pinalli, R. & Dalcanale, E. Supramolecular sensing with phosphonate cavitands. *Acc. Chem. Res.* **46,** 399–411 (2013).
16. Bonomi, R., Cazzolaro, A., Sansone, A., Scrimin, P. & Prins, L. J. Detection of enzyme activity through catalytic signal amplification with functionalized gold nanoparticles. *Angew. Chem. Int. Ed.* **50,** 2307–12 (2011).
17. Sreejith, S. & Ajayaghosh, A. Molecular logic gates: Recent advances and perspectives. *Indian J. Chem. - Sect. A Inorganic, Phys. Theor. Anal. Chem.* **51,** 47–56 (2012).
18. Scrimin, P. & Prins, L. J. Sensing through signal amplification. *Chem. Soc. Rev.* **40,** 4488–505 (2011).
19. Diez-Castellnou, M., Mancin, F. & Scrimin, P. Efficient Phosphodiester Cleaving Nanozymes Resulting from Multivalency and Local Medium Polarity Control. *J. Am. Chem. Soc.* **136**, 1158−1161 (2014).
20. Guo, D.-S., Uzunova, V. D., Su, X., Liu, Y. & Nau, W. M. Operational calixarene-based fluorescent sensing systems for choline and acetylcholine and their application to enzymatic reactions. *Chem. Sci.* **2,** 1722 (2011).

CHAPTER 4: LIGHT INDUCED MODULATION OF THE CHEMICAL FUNCTIONS OF Au NP

4.1. INTRODUCTION

One of the most beautiful natural processes is probably the retinoid cycle, in which light initiates the process that leads to our vision.[1] Morphologically, there are two distinct photo-receptors in vertebrate retinas: rods and cones. Both rods and cones exploit the unique properties of 11-cis retinal, a photosensitive derivative of vitamin A. This derivative is covalently bound to an opsin signaling protein to form a visual pigment molecule. In the presence of light, 11-cis retinal is isomerized to all-trans retinal, and the straightening of the polyene chain activates the opsin to generate a cellular response to light. Opsins are not photosensitive, and it is only when coupled with 11-cis retinal that the protein absorbs visible light. This isomerization activates a cascade of catalytic events which causes a hyperpolarization of the photoreceptor cell (Figure 4.1).[2]

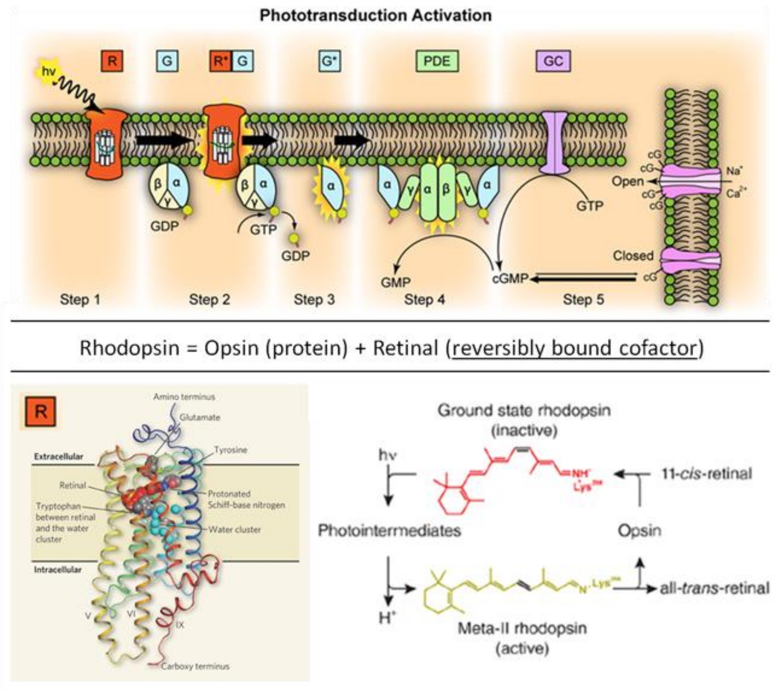

Figure 4.1. Schematic representation of the phototransduction activation on the basis of our vision (top): the light-induced isomerization of cis-retinal promotes a change in conformation of Rhodopsin, which activates a cascade of catalytic events.

Inspired by the mechanism of rhodopsin, chemists have pointed their attention towards molecular switches addressed by light. A reversible switch, as mentioned in Chapter 1, is defined as a molecular, supramolecular, or mechanically interlocked entity capable of changing its shape in response to an external stimulus.[3] In the present context, a photoswitchable molecule can be converted from one form to another with light of one wavelength and can either revert thermally to the original state or can be reverted by irradiation with light of a different wavelength. There are a number of requirements that such chemical systems must meet. The first one is that the system should absorb light at a wavelength compatible with biological systems. Second, the system must undergo some photochemistry with high efficiency so that the light dosage required to trigger an event is not too high. Third, the photoswitch must alter the biomolecule in a manner that leads to substantial change in biomolecule activity. Fourth, the system should be stable to biological conditions and inert (non-toxic) both before and after irradiation.[4] Examples of some of the most-studied classes of photoswitchable organic systems are shown below (Figure 4.2).[5]

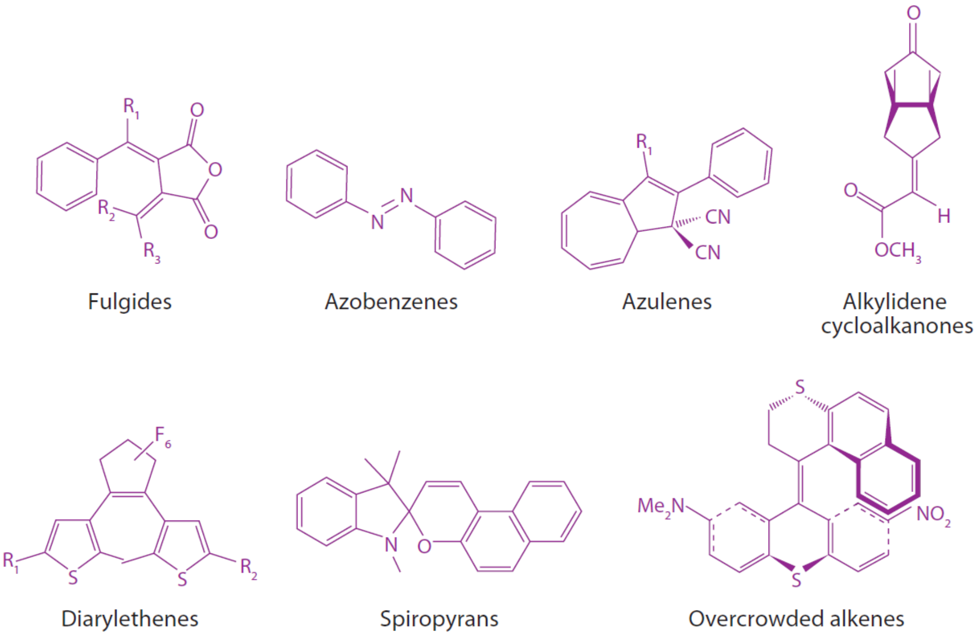

Figure 4.2. Examples of the more commonly employed classes of photoswitchable molecular systems[5]

In the recent past all of the above types of molecules have been immobilized, both through covalent and non-covalent interactions, onto a range of nanoparticles. Indeed, the combination of molecular switches and nanoparticles possesses many advantages to engineer new nanomaterials and endow them with unprecedented performances. The presence of the switches on the surface can affect various characteristic of the nanoparticles such as optical, fluorescent, electrical and magnetic properties and has been shown to lead to smart materials *e.g.* valves in which is possible to control the storage and release of molecular cargo[6], systems that can direct binding of small molecules[7] and molecular inks created by the aggregation of nanoparticle induced by light.[8,3]

The most widely used class of photoswitches for the photo-control of biomolecules are azobenzenes since they meet most of the criteria outlined above. Various characteristics that change after the isomerization can be exploited for characterization, to create a modular system by light and to create systems that mimic the visual response in vertebrate. The two isomers *trans*- and *cis*-azobenzenes present different UV-Vis spectra, in particular *trans*-azobenzene shows a weak n–Π* band near 440 nm and a strong Π–Π* transition near 320 nm and *cis*-azobenzene has a stronger n–Π* band also near 440 nm and shorter wavelength bands at 280 nm and 250 nm. Thermodynamically the *trans* conformation of azobenzene is 10–12 kcal mol^{-1} more stable than the *cis* isomer so that, in the dark at equilibrium, *trans* is the dominant isomer (99.99%),[9,10] and the *cis* isomer can be produced by irradiation with 340 nm light. The photoisomerization events occur with high quantum yields and minimal photo-bleaching. The *trans* conformation is near planar and has a dipole moment near zero.[11] Instead, the *cis* isomer adopts a bent conformation with its phenyl rings twisted ~55° out of the plane from the azo-group and has a dipole moment of 3 Debye. The *trans*-isomer can be regenerated either in the dark leading the solution to re-establish the equilibrium or by irradiation at 450 nm. In addition to the shape and dipole moment changes, the end-to-end distance of each isomer is also substantially different; the distance between the carbons at the *para* positions of the rings changes by 3.5 Å (Figure 4.3).

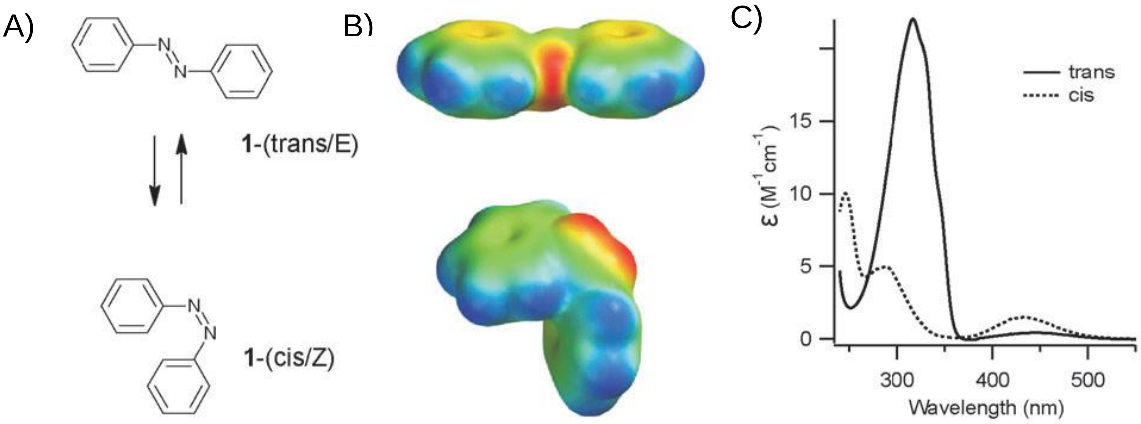

Figure 4.3. A) and B) Structures of trans and cis isomers of azobenzene. Spacefilling models are coloured by electrostatic potential (red—negative to blue—positive). C) Absorption spectra of the trans and cis isomers of azobenzene dissolved in ethanol[4].

4.1.1. Azobenzenes as modules to regulate catalysis by light

A next step forward to a synthetic system that mimics the retinoid cycle is the insertion of a light-addressable module in a catalyst. Rebek at al.[12] reported a photoswitchable catalyst for the coupling reaction reported in Chart 1.

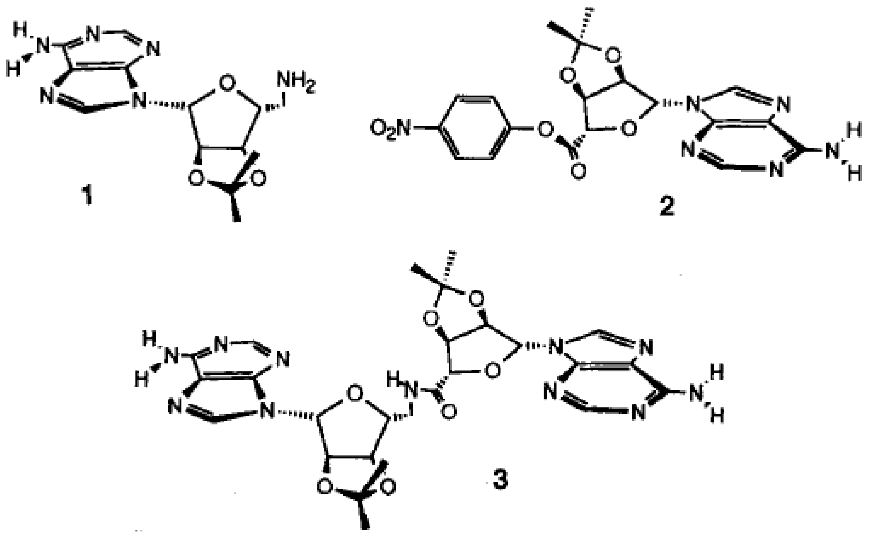

Chart 1.

Template molecules, such as **3**, containing two adenine receptors in a specific position activate the reaction between **1** and **2**. The molecule proposed as catalyst is reported in chart 2.

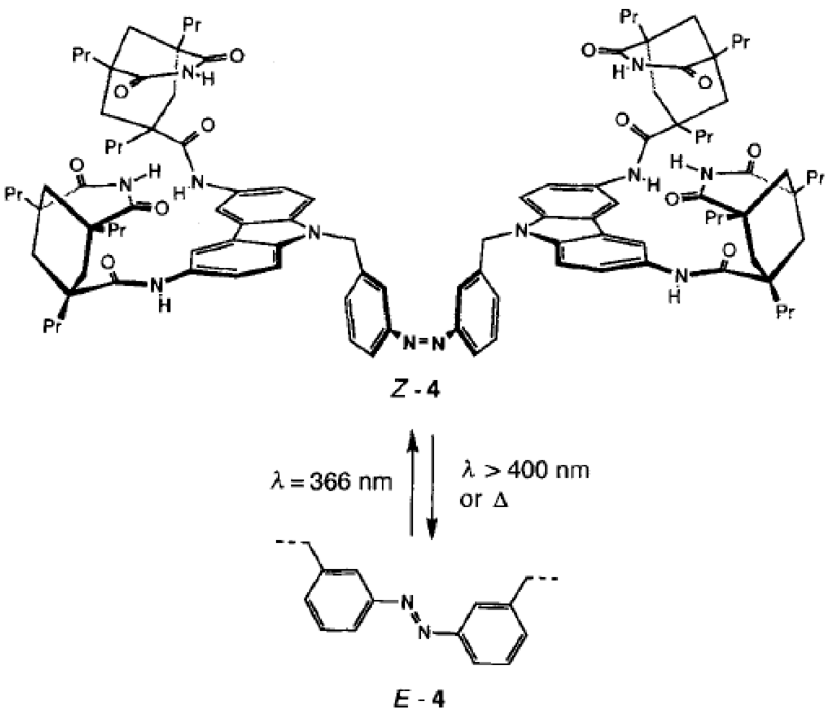

Chart 2.

The effect of receptor **4** on the rate of reaction is shown in Figure 4.4. The E isomer of **4** had a negligible effect on the reaction rate, but the *Z* isomer (in a 1/1 mixture with the *E* isomer) was shown to be an efficient catalyst thanks to its ideal geometry to form a productive ternary complex with **1** and **2**. Irradiation of **4** with light (366 nm) caused nearly a tenfold enhancement in the coupling rate.

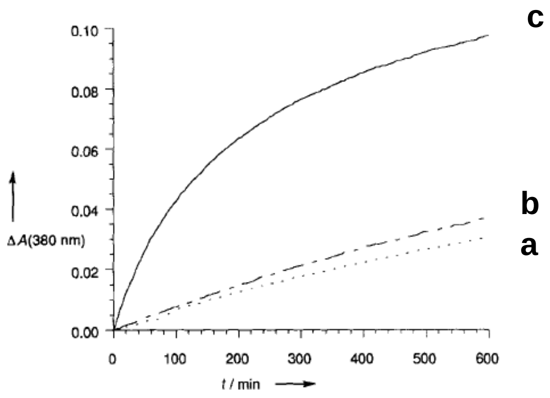

Figure 4.4. Changes in absorption A during the reaction of **1** and **2** in the absence of **4** (a) and in the presence of one equivalent of *E*-**4** (b) and *E/Z*-**4** in its photostationary equilibrium at 366 nm (c)

4.1.2. Azobenzenes as switchable surface ligands

Thanks to the characteristics discussed in Chapter 1, Au NP have been used, in the last decade, in conjuction with molecular or supramolecular switches. The matching of these two fields gave rise to systems in which switching on the surfaces of NPs can be used to modulate reversibly a range of NP properties—optical, fluorescent, electrical, magnetic—as well as the controlled release of small molecules. It has been reported that the immobilization of switches on AuNPs does not, in general, hamper their switching ability, although it can impart new properties on the supporting particles.[13]

One key example of the combination of Au NP and azobenzenes was reported in 2009 by Grzybowski.[14] It aimed at the creation of self-erasing inks based on the ability to prepare metastable materials that remain assembled only as long as energy (light) is delivered to them. The system was based on gold nanoparticles covered with a mixed monolayer of *trans*-4-(11-mercaptoundecanoxy) azobenzene (MUA) and dodecylamine (DDA). As shown in Figure 4.5 B the irradiation by UV light provoked the isomerization of the azobenzene moieties. The *cis* isomer reverted to the trans form either spontaneously (slowly), upon irradiation with visible light, or by heating (both rapidly) that means that that the immobilization was not affecting the intrinsic characteristics of the switch.

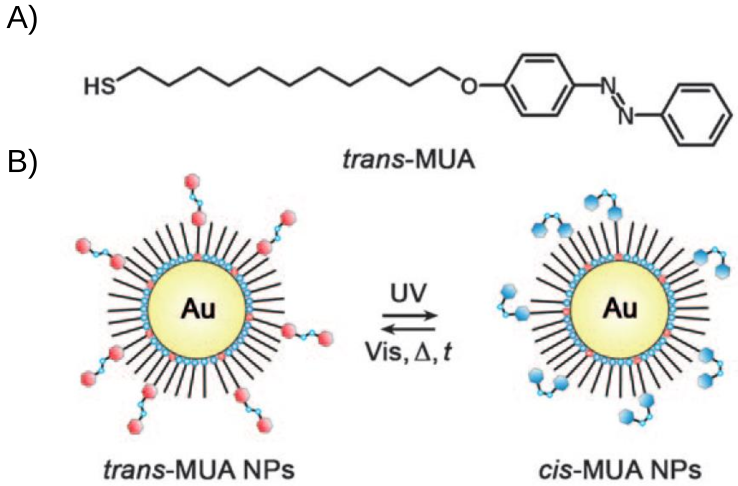

Figure 4.5. A) Structural formula of trans-4-(11-mercaptoundecanoxy)azobenzene (trans- MUA). B) UV irradiation of nanoparticles covered with a mixed monolayer of MUA and DDA causes photo-isomerization of *trans*-MUA to *cis*-MUA. The *cis* isomer reverts to the *trans* form either spontaneously (slowly), upon irradiation with visible light, or by heating (both rapidly)

When exposed to UV light, *trans*-azobenzene groups coating the NPs isomerized to *cis*-azobenzene with a large dipole moment.[8] As a result, the NPs aggregated into assemblies[15,16,17] whose color depended on the duration of UV irradiation (Figures 4.6 A). Initially, the Au NP were dispersed in semi-permeable syndiotactic PMMA ‘‘paper’’ and the colour of the films was red. However, after the film was irradiated with UV through a transparency mask, the Au NP in the irradiated aggregated and it resulted into pronounced colour changes (Figure 4.6 B). Remarkably, by adjusting the number of azobenzenes switches per NP, it was possible to control the erasure times—from seconds for smaller values of n (≈105), to hours when n was large (≈145).

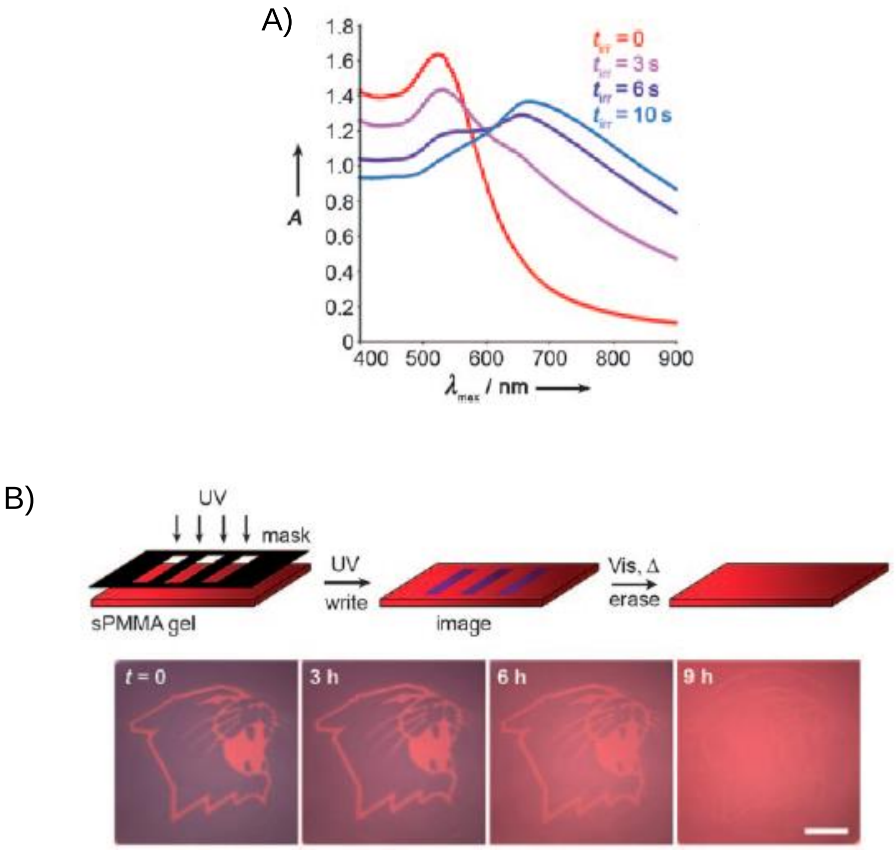

Figure 4.6. A) UV/Vis spectra of Au NP (left) and films exposed to 365 nm UV light (10 mWcm^{-2}) for times t_{IRR} varying from 0 to 10 s. In both cases, the red shift of the surface plasmon resonance (SPR) band is due to the aggregation of particles into aggregates of mean diameter d=150 nm. Colors of the curves correspond to those observed in experiments. Writing into self-erasable NP films. B) Images created in Au NP (fractional surface coverage of MUA χ=0.3, upper rowby t_{IRR} ≅0.8 s exposure through a transparency photomask. The image in the Au NP film self-erases in daylight within 9 h

4.2. RESULTS AND DISCUSSION

4.2.1. Modulation of surface binding induced by light

The first challenge of this project was to understand the behavior of a photoswitchable molecule self-assembled on the surface of Au NP. For that purpose we studied the electrostatically driven self-assembly of a negatively charged azobenzene (i.e. 4-(phenylazo)benzoic acid (**1**)) on the surface of Au NP **5**•$Zn^{2+.}$ As demonstrated in Chapter 3, the cationic surface of Au NP **5**•$Zn^{2+.}$ can bind quantitatively oligoanions even at low µM concentrations in water.[18] We wondered whether the isomerization of **1**, could promote a change in the affinity for the surface of the nanoparticles. This possibility could be, then, exploited to control by light the release of another reporter molecule from the surface.

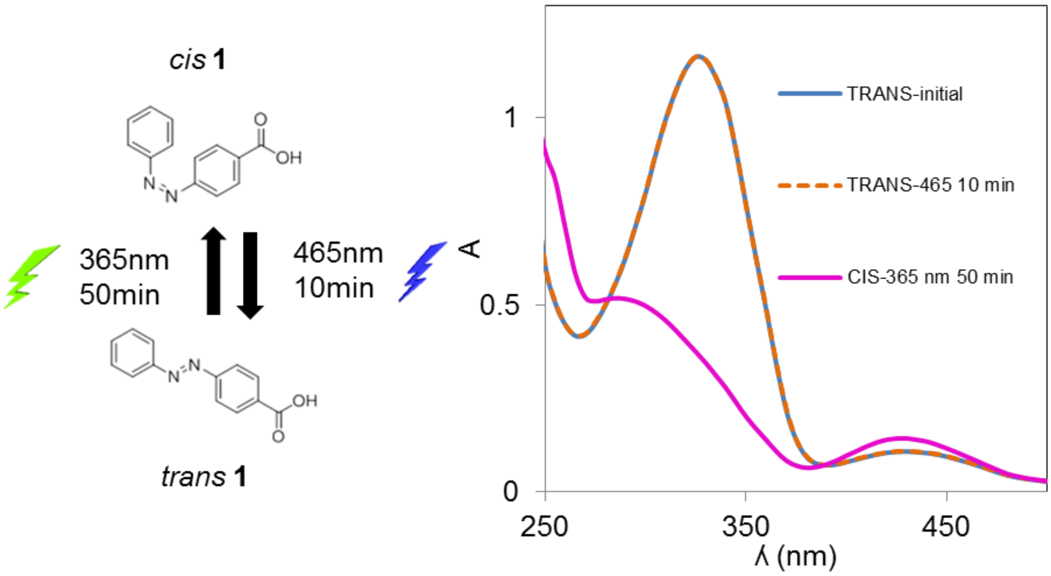

Figure 4.7. Chemical structures of the two isomers *cis*/*trans* **1** and their absorption spectra (60µM) (*trans* **1** (blue) switching to *cis* **1** (pink), and reversed relaxation to *trans* **1** (dotted yellow)).

The commercially available derivative **1** presented absorption spectra and light induced isomerization similar to azobenzene (Figure 4.7). The ratio of the initial state of **1** was measured by UHPLC at the isosbestic point (390 nm), where the absorption of *trans*/*cis* **1** is independent on the isomeric form. It revealed that isomer **1** in its initial form was 98% *trans* (Figure 4.8 A).

Assuming this percentage as the initial ratio of *trans*/*cis,* we followed the change in concentration of the *trans*-isomer (peak at 1.9 min) (at $\lambda_{max\text{-}trans}$= 326 nm) (Figure 4.8 B). Azobenzene **1** isomerized from *trans* to *cis* upon irradiating at 365 nm for 50 minutes reaching a photostationary state of 37% of the *trans*-isomer (and consequently *cis* **1** = 63%, Figure 4.8 B). The photochemical return took place upon irradiation for 10 min at 465 nm (*trans* **1** 98%, see Figure 4.7 dotted orange line). The thermal *cis*-*trans* isomerization in the dark occurred after 2 days reaching the same percentage of *trans*. The areas of the peaks of the chromatograms were used for the quantification of the different photostationary states.

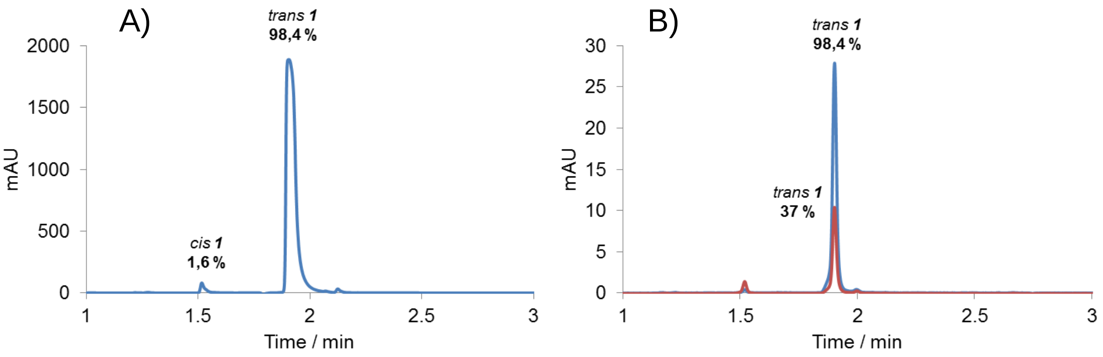

Figure 4.8. Chromatograms of the system containing A) 7 mM of **1** measured at 390nm (isosbestic point) B) 20 µM of **1** before (blue) and after (pink) irradiation (365 nm for 1h at 326 nm). The concentration used in Figure 8A was increased in order to obtain a reasonable absorption at 390 nm. Conditions: 5-95 %B in 3 min, 0.8 mL/min; A: H_2O+0.1% HCOOH, B: ACN+0.1% HCOOH.

4.2.2. Identification of a fluorescent probe for light-induced displacement

The azobenzene-compound under investigation, 4-(phenylazo)benzoic acid **1**, did not present any fluorescent properties, thus permitting the use of competition experiments with fluorophores to assess the binding affinity of the cis- and trans-isomers of **1** for Au NP **5**•Zn^{2+}.

Four different negatively charged fluorophores were chosen: **ATP$_F$** (**2**), **dATP$_{MANT}$** (**3**), 343Coumarin-GDDD (**4**), and 6,8-dihydroxy-1,3-pyrenedisulfonic acid (**5**). As a first target we wanted to understand to which extent the absorption of the cis- and trans-isomers of azobenzene **1** would affect the fluorescent properties of the fluorophores **2-5**. The titration of compound **1** to solutions containing either one of the fluorophores **2-5** showed that the fluorescence of both **2** and **3** dropped drastically (Figure 4.9). In the case of **2** this was caused by overlapping absorption spectra of **1** and **2** (λ= 355 nm) (Figure 4.9 E). In the same way the absorption spectrum of **3** presents a maximum that at 300 nm that overlaps with the absorption spectrum of **1** (Figure 4.9 F).

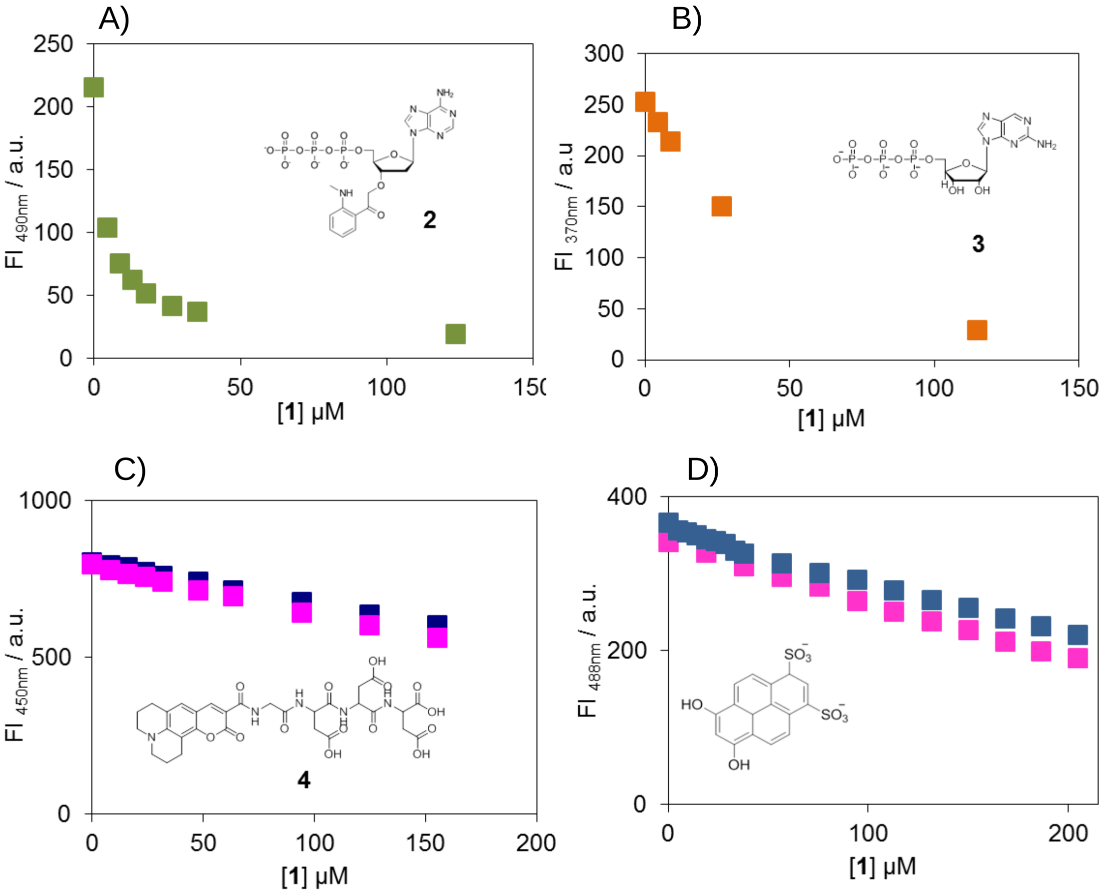

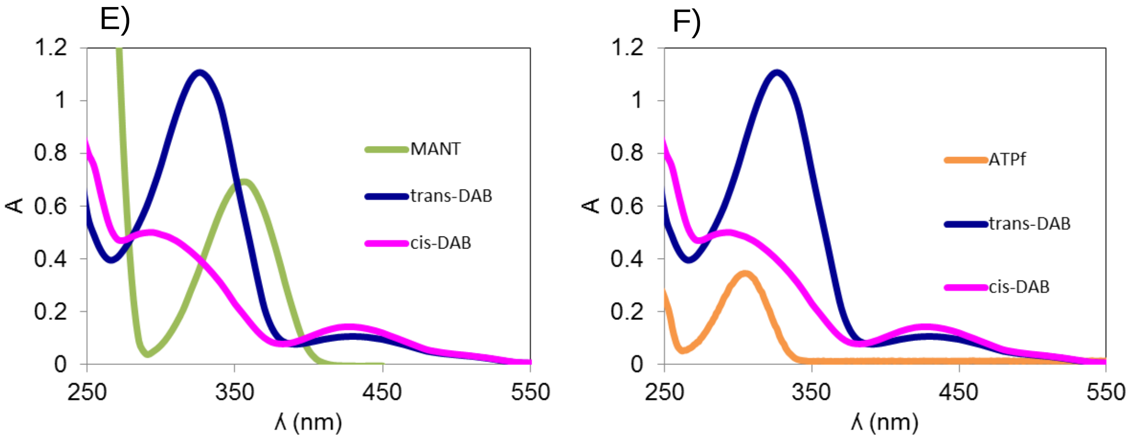

Figure 4.9. Fluorescence spectra of the titration of A) *trans* **1** on probe **2** B) *trans* **1** on probe **3** C) *trans* and *cis* **1** on probe **4** (1.2 µM) D) *trans* and *cis* form of probe **5** (1.6 µM) E) Absorption spectra of *cis*/*trans* **1** (respectively pink and blue line) and **2** (green line) F) Absorption spectra of *cis*/*trans* **1** (respectively pink and blue line) and **3** (orange line).

For the fluorophores **4** and **5**, the decrease in FI was much less pronounced. It was found, furthermore, that the *cis*- and *trans*- isomers of **1** influence the fluorescence quantum yield of **4** and **5** slightly differently Figure 4.9 (C and D). However, this difference was very small and certainly not large enough to prevent the use of **4** and **5** for the displacement experiments.

4.2.3. Displacement experiments

In order to test whether the two isomers of **1** have different affinities for the monolayer surface of Au NP **5**•Zn^{2+}, competition experiments between the *cis/trans* forms of **1** and the fluorophores **4** and **5** were performed. The first step was a determination of the SSC of **4** and **5** on Au NP **5**•Zn^{2+}. The binding curves revealed that both **4** and **5** bind Au NP **5**•Zn^{2+} under saturation conditions. A surface saturation concentration (SSC) of respectively 4.7 µM and 8.0 µM was determined (for 20 µM of head groups).

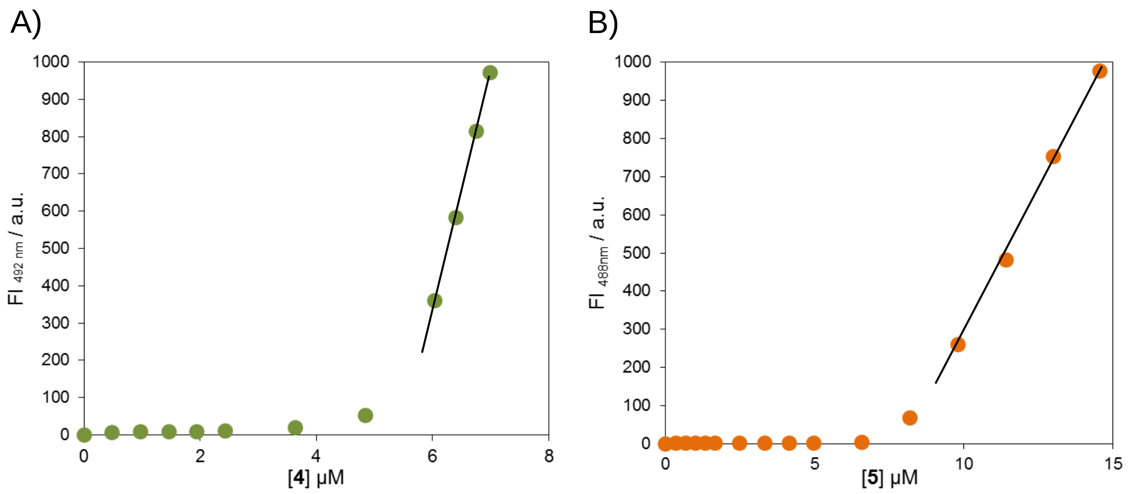

Figure 4.10. Fluorescence intensity as a function of the amount of A) concentration of **4** (ʎex = 450 nm, ʎem = 492 nm, slit 2.5/5 nm B)concentration of **5** (ʎex = 407 nm, ʎem = 488 nm, slit 5/5 nm)**,** added to a solution of Au NP **5**•Zn^{2+}. Conditions: [Au NP **5**•Zn^{2+}]= 20 µM, [HEPES] **=** 10 mM. pH = 7.0.

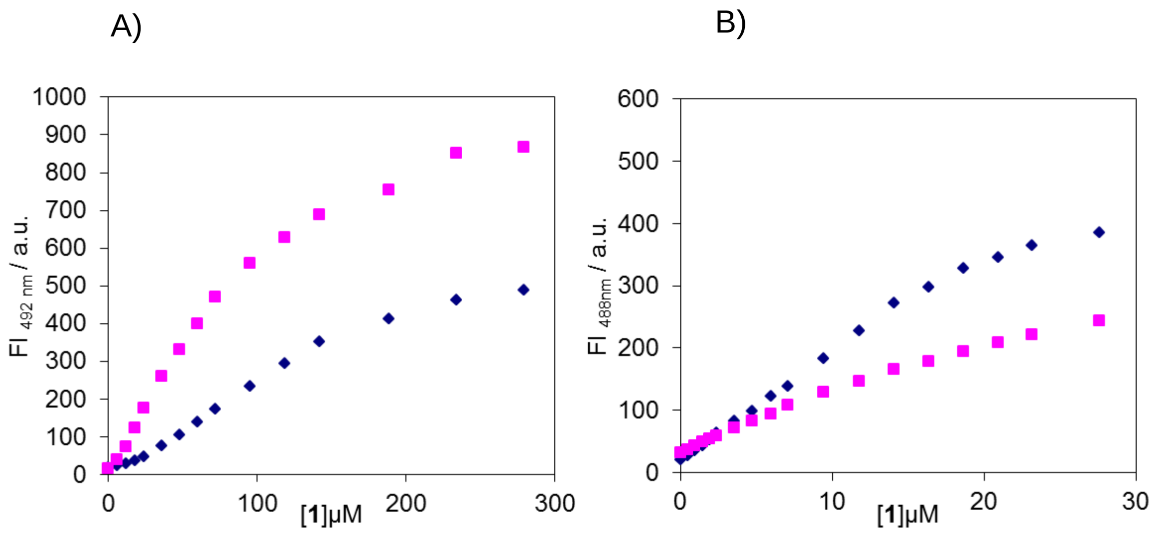

Figure 4.11. Fluorescence emission provided by competition experiments between *trans* (blue) *and cis* (pink) **1** and A) **4** B) **5**. Conditions: [Au NP **5**•Zn^{2+}]= 20 µM, [HEPES] = 10 mM. pH = 7.0 [**4**] = 4.7 µM, [**5**] = 8 µM.

The competition assay relies on the displacement of the fluorescent probe from the surface of Au NP **5**•Zn^{2+} surface upon the addition of increasing amount of *cis*/*trans* **1.** This allowed the determination of the relative affinities of both isomers. Interestingly, at pH = 7 a considerable difference in affinity between cis/*trans* **1** was observed when either fluorophore **4** or **5** was used, indicating that binding to the surface was sensitive to the geometry of **1**. Indeed, *trans* **1** can promote a maximum displacement of 30% of **4** compared to 15% displaced by the *cis*-isomer indicating that *trans* **1** has higher affinity for the surface. The percentages remained similar in the case of probe **5** (28% for *trans* **1** and 16% for *cis*).

None of the curves reached a plateau that coincided with the maximum that would be expected for a complete displacement of the fluorophores. This meant that neither of the two isomers is able to displace completely probe **4** or **5** from the surface. This could indicate that the probe molecules have different binding modes to the surface and that **1** displaces only those with a lower affinity. Knowing the relation ΔFI/Δ[probe (**4** or **5**)] (plotted line in Figure 4.10 A and B) , and correcting it for the FI lost due to the absorption of either *cis* or *trans* form (Figure 4.9 C and D), a rough quantification of the amount of probe displaced was calculated (for details see 4.4.5). It indicated that the amounts of **4** displaced by *cis* and *trans* **1** were respectively 0.5 µM and 1 µM. The same analysis performed for fluorophore **5** provided values of 1.1 µM and 2.3 µM, respectively.

In order to confirm the amount of probe displaced by **1** a methodology based on the use of membranes with defined molecular weight (MW) cut-off was developed. Such ultracentrifugal filters are commonly used for concentrating proteins, relying on the fact that large molecules cannot pass through the membrane whereas small ones can. In the same way, molecules that are free in solution are able to pass through the membrane whereas molecules bound to the monolayer surface of Au NP **5**•Zn^{2+} are unable to do so. The analysis of the filtrate (containing free displaced molecules) by LC/MS would then provide the quantification of the fluorescent probe displaced from the surface. The type of membrane used was VIVASPIN PES (10 KDa).

The chromatograms of the solutions after filtration of the system under investigation and the control experiment (in absence of nanoparticles) are shown in Figure 4.12. From the control experiment it can be observed that, in the absence of nanoparticles, the presence of either *cis or trans* **1** did not affect the amount of fluorophore in the filtrate. On the other hand, in the presence of Au NP **5**•Zn^{2+} the amount of the probe in the filtrate was significantly reduced, caused by the interaction of the probe with the monolayer. Importantly, the separate addition of *cis* and *trans* **1** to the saturated system provoked different displacements of the fluorescent probe. As shown in Figure 10 the affinity of *trans* **1** was higher compared to *cis* **1** causing a lofty displacement of **4**. From the calibration curve it was possible to quantify the concentration of **4** displaced: 0,7 µM for *trans* **1** and 0,38 µM *cis* **1.** The results were consistent with the displacement experiments obtained by fluorescence and indicated that the displacement was driven by the relative affinity of the isomers for Au NP **5**•Zn^{2+}.

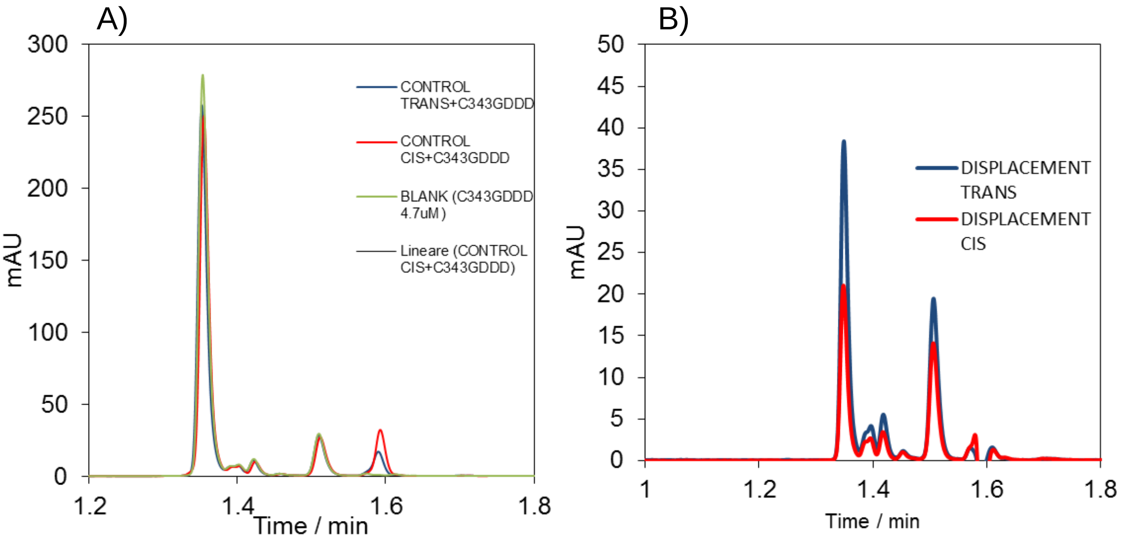

Figure 4.12. Chromatograms after filtering of the system containing 100µM of *cis* and *trans* **1**, **4** (4,8 µM): A) in absence of Au NP **5**•Zn^{2+}B) in the presence of 20 µM of Au NP **5**•Zn^{2+}

4.2.4. Isomerization properties of 1 on Au NP surface

Molecules that switch effectively in solution might not necessarily retain these characteristics after binding to a surface. The behavior of azobenzene as head group of thiols assembled on Au NP has been studied in more detail demonstrating that, when densely packed on a planar surface, the switching may be completely hampered.[13]

In order to confirm the switching abilities of **1** when it is self-assembled on the surface of Au NP **5**•Zn^{2+}, the efficiency of isomerization was quantified as mentioned in 4.2.1. The study of the system was carried out in the presence Au

NP **5•**Zn^{2+}(20 µM), and **1** (20µM) considering the experiments shown in section 4.1.2.2.

The quantification was performed by UHPLC measuring the relative concentrations of both isomers *cis*/*trans* **1** after every irradiation (4 cycles). As demonstrated in 4.2.1.1, the initial ratio of *trans*/*cis* **1**, measured at 390nm (isosbestic pont) is 98/2. Starting from this ratio the percentage of decrease of the *trans*-isomer was studied and the value of *cis* **1** assigned consequentely.

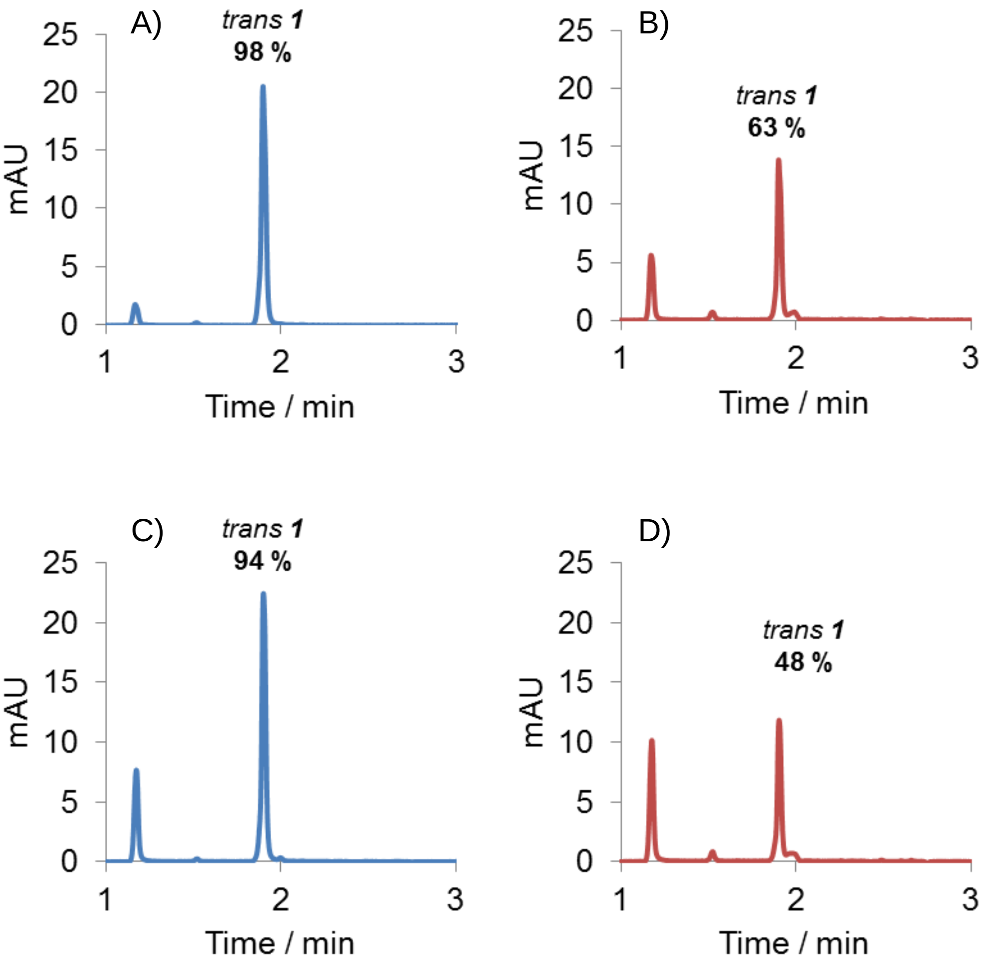

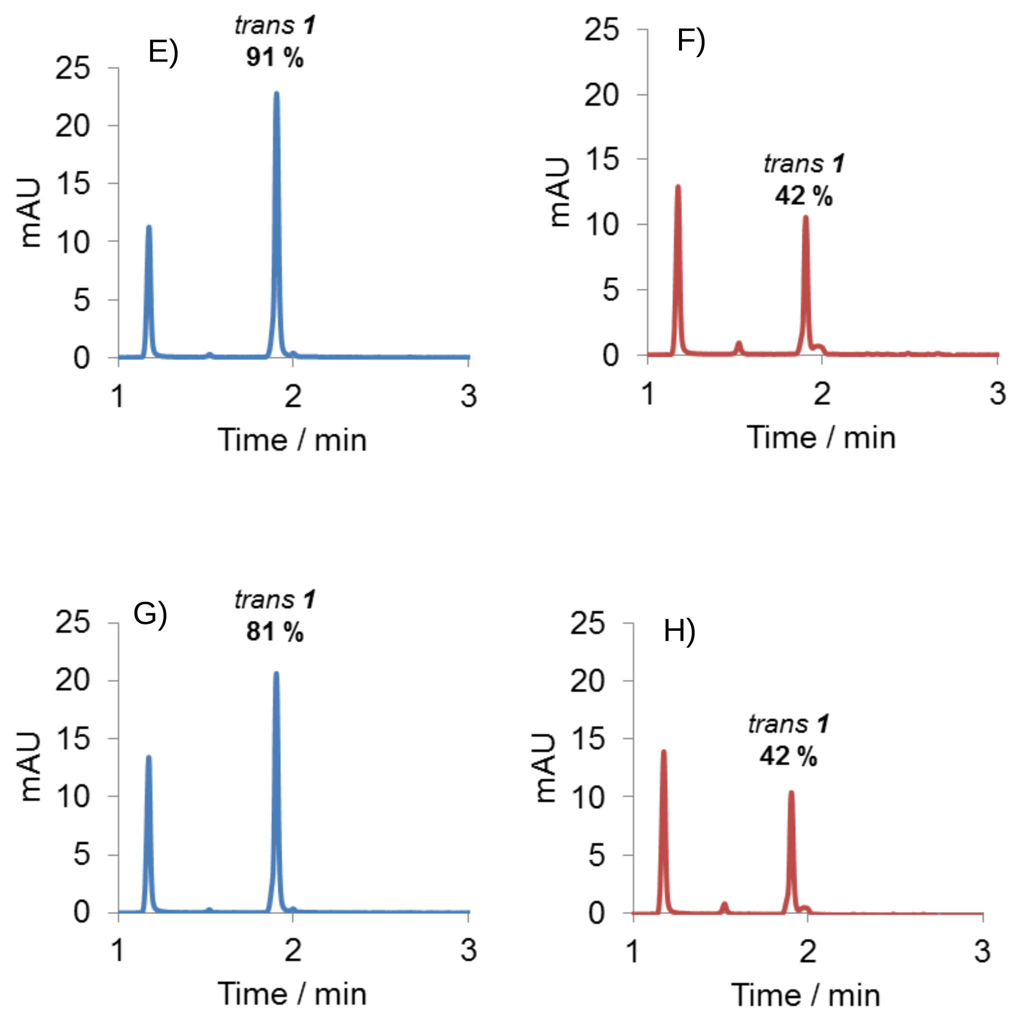

Figure 4.13. Chromatograms indicating the *cis/trans* **1** ratio of the system containing Au NP **5**·Zn^{2+} (20 µM) and 20 µM of **1** A) in its initial form, B) after the first irradiation at 365 nm for 1h, C) after first irradiation at 465 nm for 10 min, D) after second irradiation at 365 nm for 1h, E) after second irradiation at 465 nm for 10 min, F) after third irradiation at 365 nm for 1 h, G) after final irradiation at 465nm for 10 min. Conditions: 5-95 %B in 3 min, 0.8 mL/min; A: H_2O+0.1% HCOOH, B: ACN+0.1% HCOOH measured at 326 nm, [Au NP **5**•Zn^{2+}]= 20 µM, [HEPES] = 10 mM. pH = 7.0.

The results showed that the amount *trans* **1** is reduced by 10% after 3 switching cycles (1 cycle= irradiation for 1h at 365 nm to achieve *cis* **1** and at 465 nm for 10 min to obtain *trans* **1**), whereas the concentration *cis* **1** on the surface increased of 50% after 4 cycles.

This experiment demonstrated that the ability of **1** to isomerize is maintained, although it results progressively less effective. The interesting point is that the surface seems to stabilize, during time, the *cis*-isomer. The reasons are not still clear, but it could be hypothesized the *cis*–isomer may interact with the monolayer, or, alternatively, that Π-stacking interactions between *cis*-**1** could enhance its stability preventing its photoisomerization to the *trans*-isomer during the cycles.

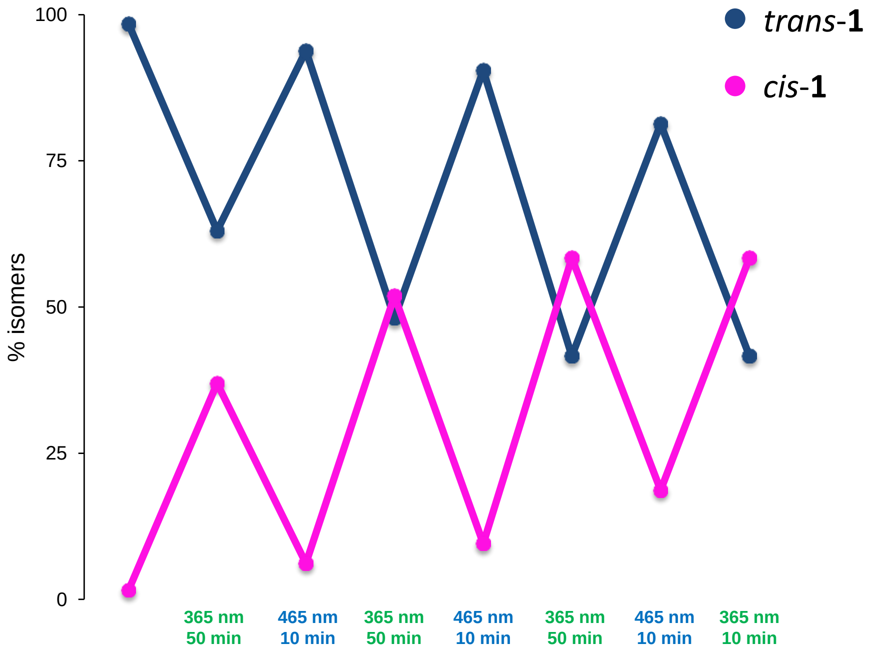

Figure 4.14. Percentage of isomerization of **1** *cis* (pink) *trans* (blue) in the presence of Au NP **5**•Zn^{2+}.

4.2.5. Cycles

The previous experiments demonstrate that the geometry of *cis*/*trans* **1** affects the affinity for the surface of the Au NP **5**•Zn^{2+}, which in principle means that the light-induced conversion from cis to trans can promote the release of a reporter molecule from the surface.

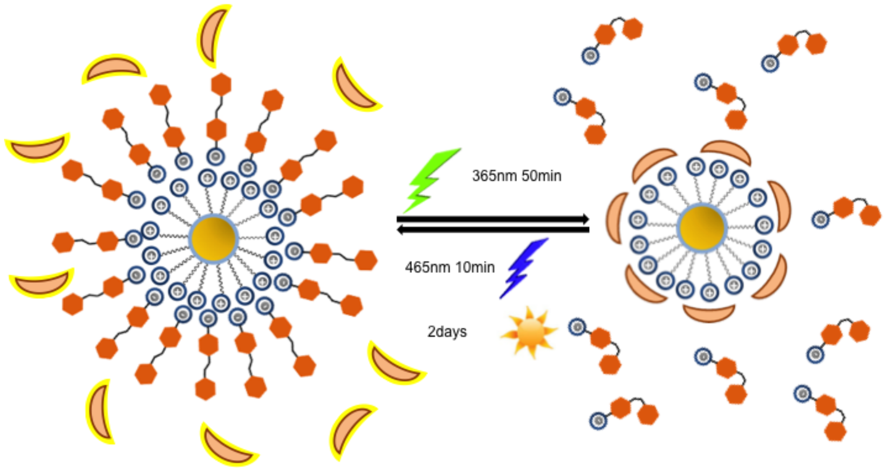

Figure 4.15. Schematic representation of the cycles induced by light

Firstly, we decided to follow cycles of displacement using fluorescent measurements. Unfortunately, the control experiment revealed that, after irradiation at 465, **4** suffered significantly from photobleaching. To reduce this problem, the cycles were carried out in six separated cuvettes containing the same solution of Au NP **5**•Zn^{2+} and fluorescent probe **4**. The compound *trans* **1** was added (100 μM) to one cuvette (**A**) (Figure 4.16, and the fluorescence was measured. Then, the *trans* **1** solution was separately irradiated from *trans* to *cis* (365nm, 50 min), and from *cis* to *trans* (465nm, 10 min) and added to the other five cuvettes (**B-F**) after each switching. The fluorescence response after each addition is shown in Figure 13.

Consistently with the data reported before, the *trans* form promotes a higher displacement of **4** from the surface of Au NP **5**•Zn^{2+}compared to the *cis* isomer. This confirmed the indication that the *cis* form has a lower affinity for the surface of the nanoparticles. The results demonstrated that it was possible to obtain a cyclic system in which the release of the fluorophore from the surface was modulated by light.

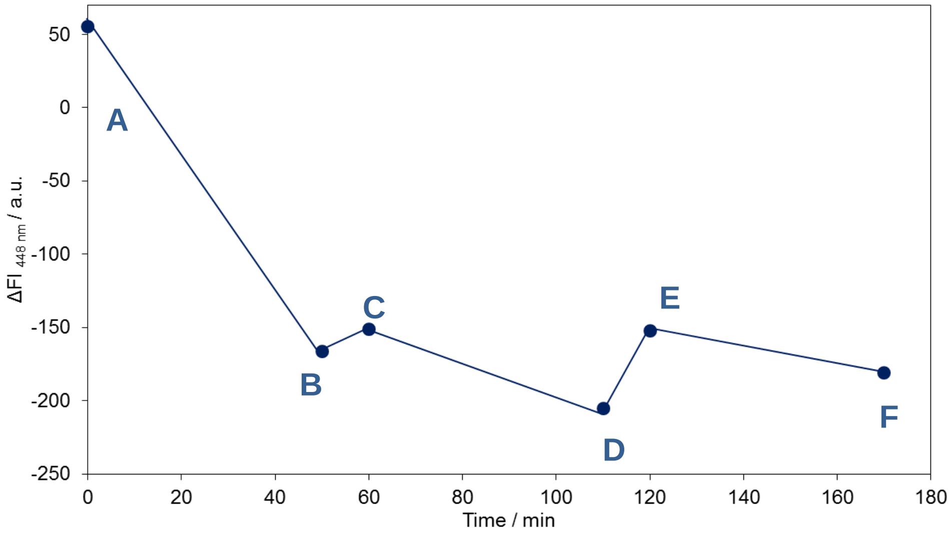

Figure 4.16. Fluorescent signal corresponding to displacement of probe **4.** The cycles are obtained thanks to the formation of *cis* and *trans* isomers formed by light. Conditions: [Au NP **5**•Zn^{2+}]= 20 µM, [**1**] = 100 µM, [**4**] = 4.8 µM, [HEPES] = 10 mM, pH = 7. Wavelenghts: $\lambda_{trans\text{-}cis}$ = 365 nm (60 min), $\lambda_{cis\text{-}trans}$ = 465 nm (10 min) λ_{ex}(**4**) 450 nm), λ_{em}(**4**) 492 nm.

To overcome the drawback of photobleaching given by **4,** we decided to perform the cycling using probe **5**, which did not photobleach upon irradiation. In this experiment 20 µM of **1** in its *trans* form was added to a buffered solution of Au NP **5**•Zn^{2+} saturated with **5** and the fluorescence was measured. After the stabilization of the signal the cuvette was irradiated for 50 min at 365 nm in order to isomerize **1.** This resulted in a significant decrease in fluorescence intensity (about 150 a.u.). This is explained by the lower affinity of the cis-isomer for the surface leading to a recomplexation of the fluorogenic probe 5. Next, the fluorescent signal was measured after irradiation of the cuvette by Vis light (465 nm for 10 min) causing an increase in the fluorescent intensity due to the isomerization to the *trans* form. The cycle was repeated 4 times (Figure 4.17).

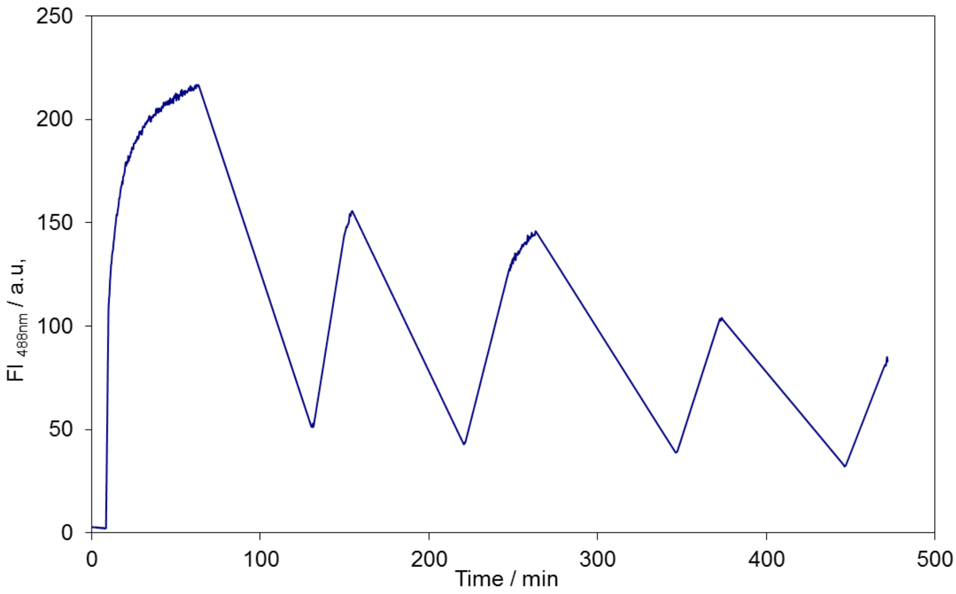

Figure 4.17. Fluorescent signal corresponding to displacement of probe **5.** The cycles are obtained thanks to the formation of *cis* and *trans* isomers formed by light. Conditions: [Au NP **5**•Zn^{2+}]= 20 μM, [**1**] = 100 μM, [**4**] = 4.8 μM, [HEPES] = 10 mM. Wavelenghts: $\lambda_{trans\text{-}cis}$ = 365 nm (60 min), $\lambda_{cis\text{-}trans}$ = 465 nm (10 min) Λ_{ex}(**4**) 450 nm), Λ_{em}(**4**) 492 nm

From Figure 4.17 it is possible to observe that, after the isomerization from *cis* to *trans* form, the fluorescent signal did not reach the same value and it decreased every cycle. As shown in Figure 4.14, this can be justified considering the isomeration efficiency loss observed in every cycle. We hypothesize that the *cis* form, interacting with the surface, can penetrate in the apolar part of the monolayer and becomes kinetically trapped. This hypothesis was studied by UV.

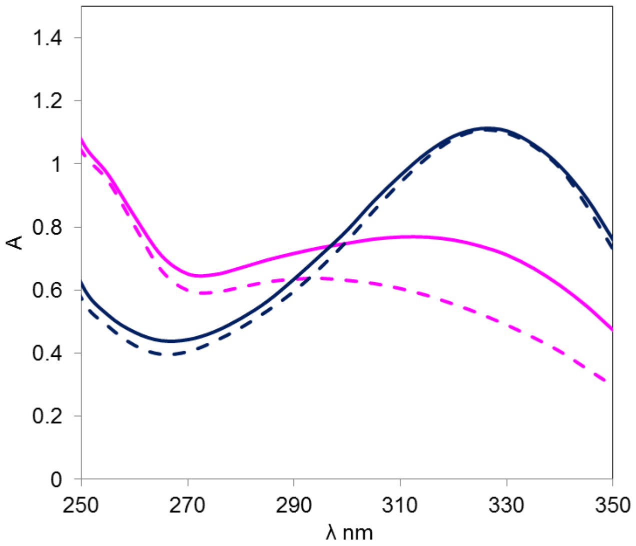

Figure 4.18. Absorption spectra of *cis* **1** (80 μM, pink) and *trans* **1** (60 μM, blue) in absence of nanoparticles (dotted line) and in the presence of 20 μM Au NP **5**•Zn^{2+}. (normal line)

The separate titration of the two isomers in the presence and in absence of AuNP **5**•Zn^{2+} was carried out and the UV-Vis signal registered. As shown in Figure 14 the presence of nanoparticles promoted a bathochromic shift when *cis* isomer was added, which could be an indication of the formation of interactions with the monolayer or the formation of aggregates between **1** induced by the surface.

4.2.6. Catalysis

Considering that Au NP **5**•Zn^{2+} are also catalytically active, we then wondered whether photo-switchable molecule **1** could act as cofactors for catalyst regulation, leading to a system similar to the retinoid cycle. It has been shown in Chapter 3 that Au NP **5**•Zn^{2+} can catalyze the transphosphorylation of the substrate HPNPP.[19] Prior studies had shown that oligoanions, competing with the substrate for the surface of Au NP **5**•Zn^{2+}, can completely inhibit the catalytic activity. Considering the different degree of affinity of *cis* and *trans* isomers we wondered whether they would compete with HPNPP to different extents.

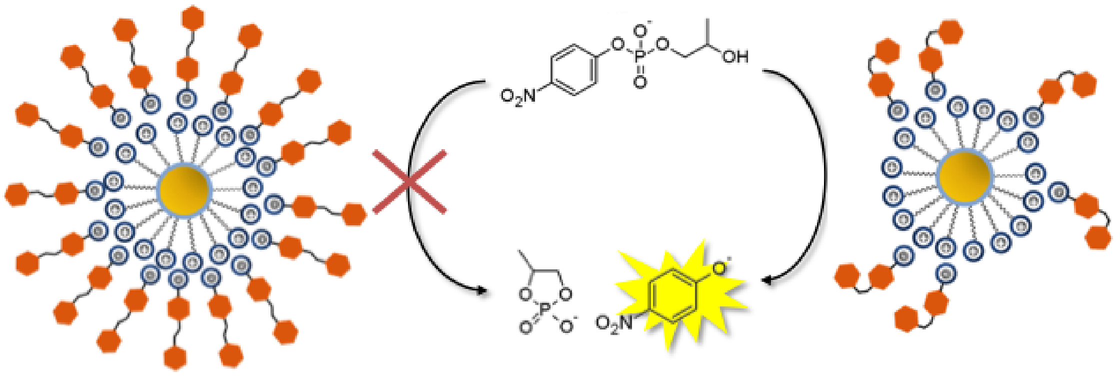

Figure 4.19. Schematic representation of the concept

In the first experiment the catalytic activity of Au NP **5**•Zn^{2+} in the presence of increasing amounts of *cis* and *trans* **1** was tested. The results (Figure 4.20) indicated no difference between the inhibitory activity of the two isomers. This may be caused by the excess of substrate used (1mM) creating a condition in which it is not possible to observe a difference between cis and trans. This is why it was decided to carry out the same experiment lowering the concentration of substrate.

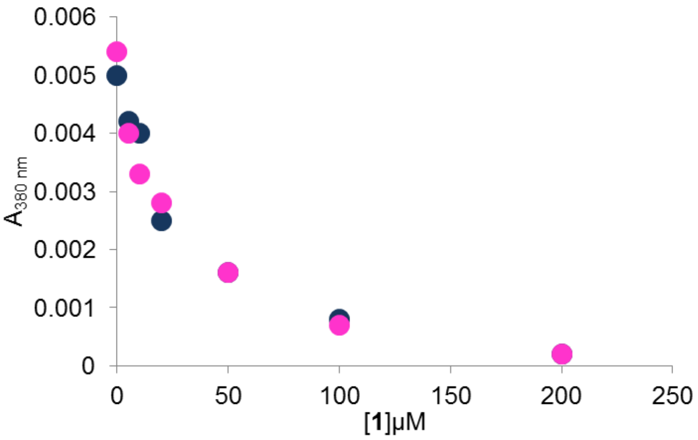

Figure 4.20. Inhibition studies of the catalytic activity of Au NP **5**•Zn^{2+}. The absorbance value related to the formation of p-nitro phenol against increasing concentration of *cis* (pink) and *trans* (blue).

In order to determine how both isomers (*cis/trans*) affected the HPNPP catalysis a series of kinetics at different azobenzene concentrations were done. The optimal concentration of HPNPP was decreased to 100 µM considering that lower concentrations would significantly reduce the reaction rate. The *p-*

nitrophenol (PNP) produced in the transphosphorylation reaction was monitored by UHPLC at 318 nm.

At 10 µM of azobenzene, no difference between the isomers was observed, but at 20 µM a higher inhibitory effect was detected for the *trans*-isomer compared to the *cis* **1** (Figure 4.21 A and B), which is in line with the fluorescence experiments. The slope was three times lower for *trans*-**1**, indicating a higher inhibitory effect (Figure 4.21 B). The fact that no difference was observed at 10 µM of azobenzene could indicate that at these concentrations the amount of azobenzene is not high enough to shield large parts of the monolayer surface. Further studies were carried out at higher concentrations of azobenzenes (50 µM), however, even though a difference between *cis/trans* isomer was found it was lower compared to that at 20 µM. I would mention that the overall rates also become very low at this concentration.

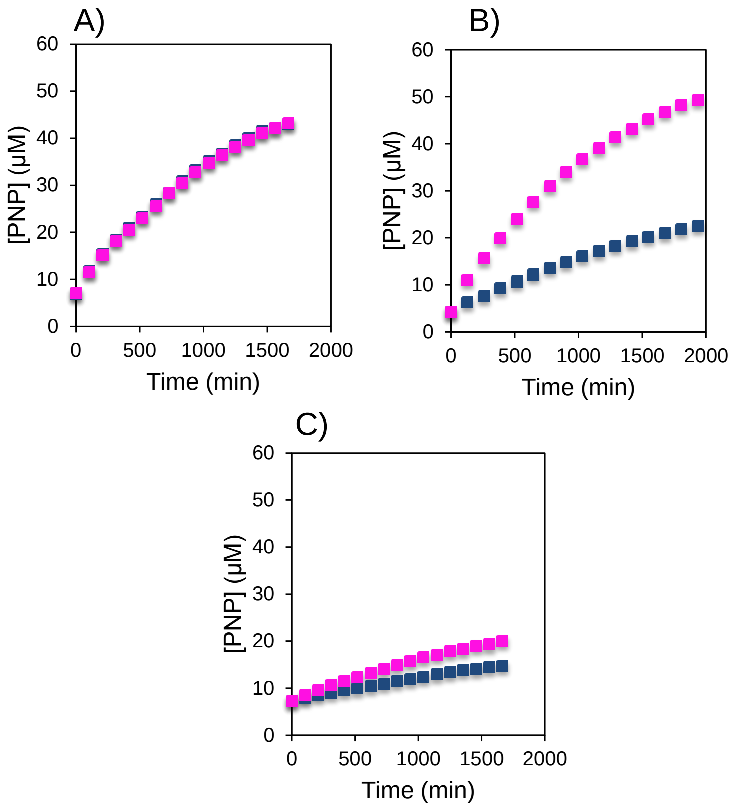

Figure 4.21. Kinetic profiles of the transphosphorylation reaction, [PNP] against time. Conditions: [Au NP **5**•Zn^{2+}]= 20 µM, [HPNPP] = 100 µM, [HEPES] = 10 mM, pH = 7 in the presence of A) 10 µM, B) 20 µM C) 50 µM of azobenzene (*cis* **1** in pink, *trans* **1** in blue). Conditions: 5-95 %B in 3 min, 0.8 mL/min; A: H_2O+0.1% HCOOH, B: ACN+0.1% HCOOH measured at 318 nm.

These results demonstrated that the *cis*- and *trans*- isomer have different inhibitory effects on the catalytic activity of Au NP **5**•Zn^{2+}, but only when present at the optimal concentration.

However, the real challenge was to switch on/off the catalysis by light. For that purpose, we started by adding 20 μM of the *trans*-isomer to a solution containing Au NP **5**•Zn^{2+}, HPNPP and HEPES at pH = 7 (same conditions above mentioned). The sample was switched from *trans* to *cis* (365 nm for 1h) and from *cis* to *trans* (465 nm for 10 min) and the liberation of PNP was measured for 30 min (every 6 min) by UPLC after each irradiation (Figure 4.22 A). The cycle was repeated four times (Figure 4.22 B and C). Figure 4.22 B indicates the trend of the rates during the cycle experiment. The obtained rates were normalized by dividing them by the rates of the *trans*/*cis* blanks (Figure 4.22 C). The two blanks consisted of performing the same HPNPP kinetics but without the switching steps, in the presence of either *trans* or *cis* isomer (experimental section). In order to maintain the same timing of irradiation, during the *trans* blank the solution was irradiated at 465 nm for 10 min every 125 min and during the *cis* blank the irradiation (365 nm for 50 min) was performed every 70 minutes.

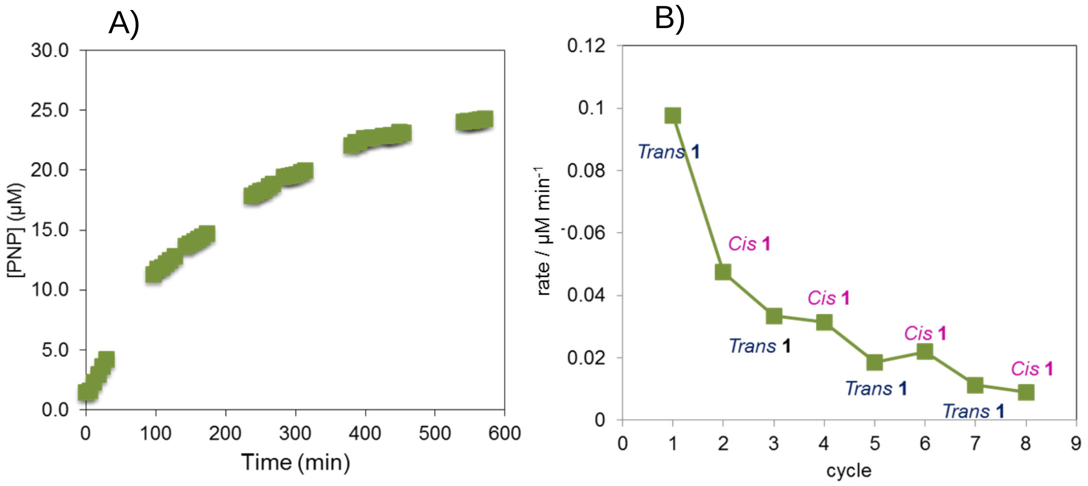

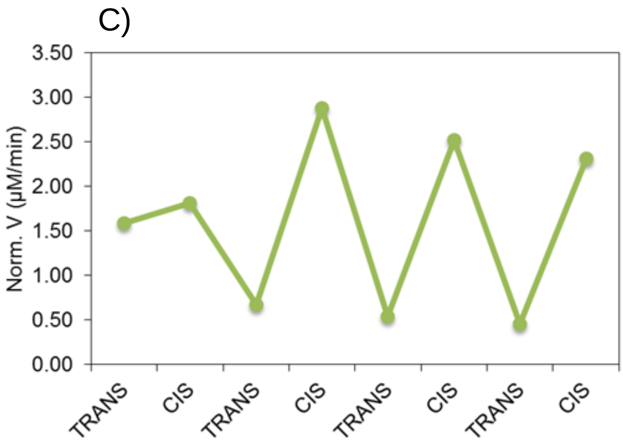

D)

	V (µM/min)			
	Switch	BLANK		Norm
		TRANS	CIS	
TRANS	0.0976	0.0617		1.58
CIS	0.0474		0.0261	1.82
TRANS	0.0334	0.0499		0.67
CIS	0.0314		0.0109	2.88
TRANS	0.0185	0.0342		0.54
CIS	0.0219		0.0087	2.52
TRANS	0.0112	0.0247		0.45
CIS	0.009		0.0039	2.31

Figure 4.22. A) Kinetic profile of HPNPP catalysis in the presence of the switching experiment B) Trend of the plotted rates of the switching experiments over cycles. C) Switching kinetic (Slopes values normalized over the blanks). D) Slope values. Conditions: [Au NP **5**•Zn^2]= 20 µM, [**1**] = 20 µM, [HPNPP] = 100 µM, [HEPES] = 10 mM, gradient: 5-95 %B in 3 min, 0.8 mL/min; A: H_2O+0.1% HCOOH, B: ACN+0.1% HCOOH measured at 318 nm.

As can be observed from Figure 4.22 the *trans* rates were consistently slower than the *cis* rates, which is in agreement with the results observed during the fluorescence measurements. The first cycle (first and second point of the graph 4.22 C) showed less influence on the catalysis of HPNPP. In the first point this is probably due to the slow stabilization of the system. The second one can be a result of the low isomerization (*cis* % = 37%) as shown in section 4.2.1.3.

4.3. CONCLUSIONS

The possibility to self-assemble light-sensitive molecular switches on the surface of Au NP **5**•Zn^{2+} was demonstrated.

The displacement studies of both probes **4** and **5** by *cis*/*trans* **1** revealed that the two isomers have different affinities for the surface Au NP **5**•Zn^{2+}. This key point could then be exploited to modulate by light the release of small molecules and the catalytic activity of Au NP in a reversible manner.

This is an important contribution to the field of supramolecular responsive systems and opens to the possibility to mimic the cascade of transformation that is present in nature for example in light induced retinoid cycle. Furthermore, the light-induced control of the local concentration of small molecules (probes) from the surface offers intriguing possibilities to signal generation and drug delivery.

4.4. EXPERIMENTAL SECTION

4.4.1. Materials and methods

For the synthesis and characterization and quantification of Au NP **5** see Chapter 3. The stock solutions of Au NP **5** were stored at 4°C in mQ water. 2'-deoxy-3'-O-(N'-methylanthraniloyl)adenosine-5'-O-triphosphate (**dATP$_{\mathbf{MANT}}$**), 2-aminopurine riboside-5'-O-triphosphate (ATP$_F$) were purchased from Biolog Life Science Institute and used as received. The buffer 4-(2-hydroxyethyl)-1-piperazineethanesulfonic acid (HEPES), 4-(phenylazo)benzoic acid and 6,8-dihydroxy-1,3-pyrenedisulfonic acid (**5**) were purchased from Sigma Aldrich and used without further purification. The concentration of **1** was determined both by weight and UV-Vis spectroscopy using ε_{355} = 5800 M^{-1} cm^{-1} at pH 7 as the molar extinction coefficient. The concentration of **2** was determined both by weight and UV-Vis spectroscopy using ε_{243} = 8000 M^{-1} cm^{-1} at pH 7 as the molar extinction coefficient. The concentration of **4** was determined both by weight and UV-Vis spectroscopy using ε_{450} = 45000 M^{-1} cm^{-1} at pH 7 as the molar extinction coefficient. The concentration of **5** was determined by weight. All the compounds were dissolved in mQ water and freshly prepared except for **1** and **4** which were respectively dissolved in a 5:2 mixture of DMSO:H_2O and EtOH.

UV-Vis spectra were recorded on a Varian Cary50 spectrophotometer equipped with thermostatted multiple cell holders. Fluorescence measurements were recorded on a Varian Cary Eclipse Fluorescence spectrophotometer equipped with a thermostatted cell holder. For the HPNPP kinetics and the switch on/off kinetics an Agilent Technologies 1290 Infinity LC equipped with a quadrupole MS was used. The UV lamp used for the irradiation was Spectroline, MODEL ENF-240C/FE 230V, 50Hz, 0.17 AMPS. The irradiation at 465 nm was performed with LED lights, RoHS Compliance Guirlade Electrique 80 Lampes 230V, 50Hz, 20mA

4.4.2. Screening of the fluorescent probe

To a 3 mL buffered solution ([HEPES]=10mM pH=7) a fixed concentration of fluorophore was added ([**2**] = 0.66 µM [**3**] =1.7 [**4**] =1.2 µM [**5**] = 1.6 µM). Then, in separate experiments either *trans*-**1** or *cis*-**1** were titrated and the fluorescent signal measured at the corresponding wavelength (ʎ$_{ex}$ **2** = 355 nm ʎ$_{em}$ **2** = 492 nm, ʎ$_{ex}$ **3** = 305 nm ʎ$_{em}$ **3** = 370 nm, ʎ$_{ex}$ **4** = 450 nm λ_{em} **4**= 492 nm, λ_{ex} **5** = 407 nm ʎ$_{em}$ **5** = 488 nm).

4.4.3. Surface saturation concentration

The SSC of **4** and **5** on Au NP **5**•Zn^{2+} were determined as described previously[18] (**4** = λ_{ex} = 450 nm, λ_{em} = 492 nm, slit: 5/5 nm, **5** = λ_{ex} = 407 nm, λ_{em} = 488 nm, slit: 5/5 nm). After each addition, the fluorescence intensities were recorded after stabilization of the signal (typically 5 minutes). The value obtained was determined via extrapolation of the linear part of the curve (5 points). The SSC of **4** and **5** on AuNp **5**•Zn^{2+} (20 µM) were determined at respectively 4.7 µM and 8.1 µM.

4.4.4. Displacement experiments

The displacement experiments were performed by measuring the fluorescent intensities after adding consecutive amounts of a stock solution of *cis* and *trans* **1** to a 3 mL buffered solution (HEPES 10 mM, pH = 7.0) containing Au NP **5**•Zn^{2+} (20 µM) covered with the fluorophore **4** (4.7 µM) (λ_{ex} = 450 nm, λ_{em} = 492 nm, slit: 5/5 nm) or **5** (8.1 µM) (λ_{ex} = 407 nm, λ_{em} = 488 nm, slit: 5/5 nm). The fluorescent intensities generated by the addition of small additional amounts of *cis* and *trans* **1** to the above-described solution, were registered after the stabilization of the signal (about 10 minutes).

4.4.5. Quantification of the amount of displace probe

In the presence of AuNP **5•**Zn^{2+}, the binding curve indicated the relation ΔFI/[**4**] is 638.65. After the addition of *trans* **1** or *cis* **1** (100 µM) the signal reaches 560 a.u. (*trans* **1**) and 234 a.u. (*cis* **1**). Knowing that at this concentration the *cis* and the *trans* **1** reduced the FI of **4** of 14,7% (*trans* **1**) 19,3% respectively (*cis* **1**) it has been possible to calculate the amount of probe displaced (Figure S1). The same quantification has been done for probe **5** (Figure S2)**.**

$$\left(\frac{\mathbf{234.71}}{\mathbf{638.35}}\right)+\frac{\mathbf{234.71}}{\mathbf{638.35}}\cdot\frac{\mathbf{19.3}}{\mathbf{100}}=\mathbf{0.5}\ \mu\mathrm{M}$$

$$\left(\frac{\mathbf{560.708}}{\mathbf{638.35}}\right)+\frac{\mathbf{234.71}}{\mathbf{638.35}}\cdot\frac{\mathbf{14.7}}{\mathbf{100}}=\mathbf{1}\ \mu\mathrm{M}$$

Figure S1. Formulas used to calculate the amount of displaced **4**.

Here, the relation ΔFI/[**4**] is 152.54 and the fluorescent values are 307.369 a.u. after the addition of *trans* **1** (20 µM) and 1622.599 after the addition of *cis* **1** (20 µM). At this concentration the *cis* and the *trans* **1** reduced the FI of **4** of 11.3 % (*trans* **1**) 4.1% respectively (*cis* **1**).

$$\left(\frac{\mathbf{307.369}}{\mathbf{152.54}}\right)+\frac{\mathbf{307.369}}{\mathbf{152.54}}\cdot\frac{\mathbf{11.3}}{\mathbf{100}}=\mathbf{2.3}\ \mu\mathrm{M}$$

$$\left(\frac{\mathbf{162.599}}{\mathbf{152.54}}\right)+\frac{\mathbf{162.599}}{\mathbf{152.54}}\cdot\frac{\mathbf{4.1}}{\mathbf{100}}=\mathbf{1.1}\ \mu\mathrm{M}$$

Figure S2. Formulas used to calculate the amount of displaced **5**.

These values were validated through a series of ultracentrifugation experiments followed by -UHPLC-MS analysis.

The blank experiments were performed by preparing 3 samples: One containing just [HEPES] = 10 mM at pH = 7 and 25 °C, [**4**] = 4.7 µM and the others adding either *cis* or *trans* **1** (100 µM).

The ultracentrifugation experiments were performed also in the presence of [Au NP **5**•Zn^{2+}] = 20 µM

Next, all the solution were equilibrated for 15 min before centrifugation was started with a duration of 15 sec and 12.000 r.p.m.. The total volume was reduced by around 20 %.

A 20 µl (using glass insertor, Sigma Aldrich code: 24707) sample was injected in the UPLC equipped with a Zorbax RRHD SB-C8 column with a length of 50 mm and an internal diameter of 2.1 mm and 1.8-mm fused silica particles at a flow rate of 0.8 mL/min. A solvent gradient from 5% (v/v) ACN+0.1% HCOOH in H_2O+0.1% HCOOH to 95% (v/v) ACN+0.1% HCOOH in H_2O+0.1% HCOOH (3 min) was used. This concentration was kept constant for 1 min after which a gradient to 5% (v/v) ACN+0.1% HCOOH in H_2O+0.1% HCOOH was imposed. The column temperature was set at 40 °C. The compound was monitored at 450 nm. Then the areas of the peaks were integrated and the concentrations of displaced **4** calculated.

4.4.6. Cycles monitored by fluorescence

4.4.6.1. Cyclization in the same cuvette

To a 3 mL buffered solution ([HEPES] = 10 mM at pH = 7 and 25 °C) containing Au NP **5**•Zn^{2+}(20 µM) saturated with **4** (4.7 µM) (Figure S1 light blue), 100 µM of *trans* **1** was added (green). The signal was left to equilibrate until a stable intensity was obtained, after which the cuvette was irradiated at 465 nm. During this irradiation we could observe that the fluorescent intensity drastically decreased (red part). After 200 min the cuvette was irradiated at 365 nm for 50 min to isomerize **1** to its *cis* form and the fluorescent signal recorded. We could observe a decrease of 89 a.u.. Subsequently the cuvette was irradiated for 10 min at 465 nm to switch back to the *trans* isomer and the fluorescence measured indicating an increase of 67 a.u. This procedure was repeated 4 times giving raise to the cycles observed in Figure S3 (blue).

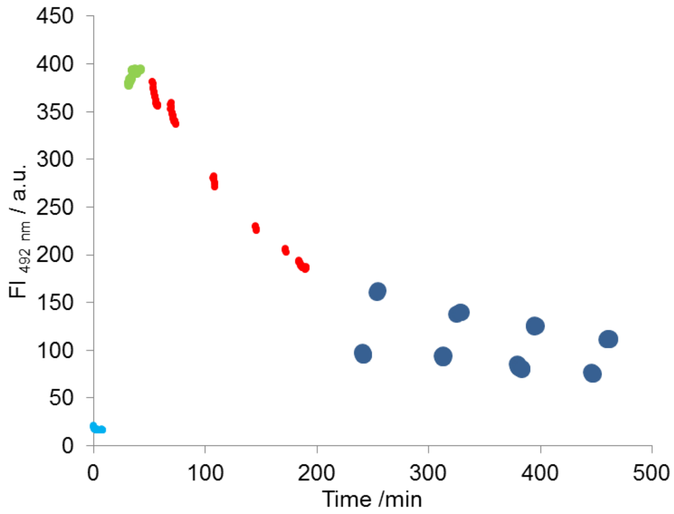

Figure S3. Fluorescent signal corresponding to displacement of probe **4.** The cycles are obtained thanks to the formation of *cis* and *trans* isomers formed by light Conditions: [Au NP **5**•Zn^{2+}]= 20 μM, [**1**] = 100 μM, [**4**] = 4.8 μM, [HEPES] = 10 mM. Wavelenghts: $\lambda_{trans\text{-}cis}$ = 365 nm (60 min), $\lambda_{cis\text{-}trans}$ = 465 nm (10 min) λ_{ex}(**4**) 450 nm), λ_{em}(**4**) 492 nm

The same procedure was performed on the system saturated with probe **5** (8.1 μM). After addition of **5** (20 μM) the signal was recorded. Then, the cuvette was irradiated for 50 min at 365 nm and the fluorescence measured. Subsequently the irradiation of the cuvette at 465 for 10 min provoked the isomerization from *cis* to *trans.* After that, the fluorescent value was taken. The cycle was repeated 4 times (Figure 4.17).

To confirm the phenomena of photobleaching of probe **4,** the same experiment was performed irradiating at 465 nm during time.

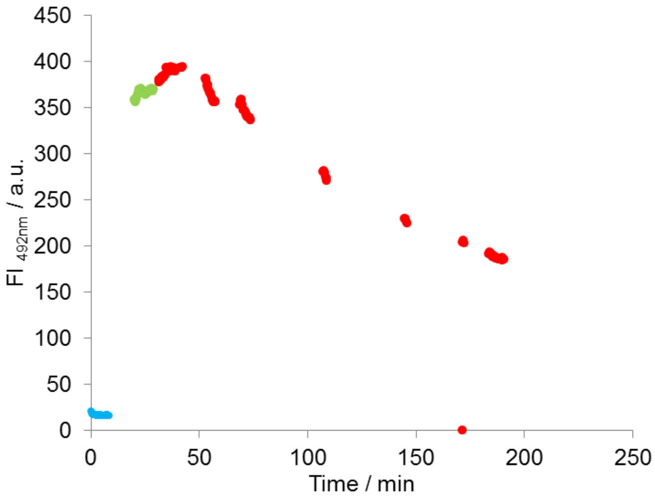

Figure S4. Fluorescent signal corresponding to displacement of probe **4.** The cycles are obtained thanks to the formation of *cis* and *trans* isomers formed by light Conditions: [Au NP **5**•Zn^{2+}]= 20 µM, [**4**] = 4.8 µM, [**1**] = 100 µM [HEPES] = 10 mM. Wavelenghts: $\lambda_{trans\text{-}cis}$ = 365 nm (60 min), $\lambda_{cis\text{-}trans}$ = 465 nm (10 min) λ_{ex}(**4**) 450 nm), λ_{em}(**4**) 492 nm

As we can observe from the graph reported in figure S4 the irradiation at 465nm provokes a drastic decrease in the fluorescent yield of prove **4**.

4.4.6.2. Cyclization in different cuvettes

A 20 mL buffered stock solution ([HEPES] = 10 mM at pH = 7 and 25 °C) solution containing Au NP **5**•Zn^{2+}(20 µM) saturated with **4** (4.7 µM) was divided in 6 different cuvettes. Then **1** (in its *trans* form, 100 µM) was added to the first cuvette and the fluorescent signal measured. The same stock solution of **1**, was irradiated for 50 min at 365 nm and then 100 µM of *cis* **1** in situ formed was added to the second cuvette and the signal recorded. Afterward, the stock solution of **1** was irradiated at 465 nm for 10 minutes to achieve the *trans* isomer. 100 µM of **1** were added to the third cuvette and the fluorescence measured. The same procedure was repeated for the remaining cuvettes.

4.4.7. UV titrations

To 1 mL buffered solution ([HEPES] = 10 mM at pH = 7 and 25 °C) containing Au NP **5**•Zn^{2+}(20 µM) additional amount of *cis* and *trans* **1** were added and the UV-Vis spectrum measured.

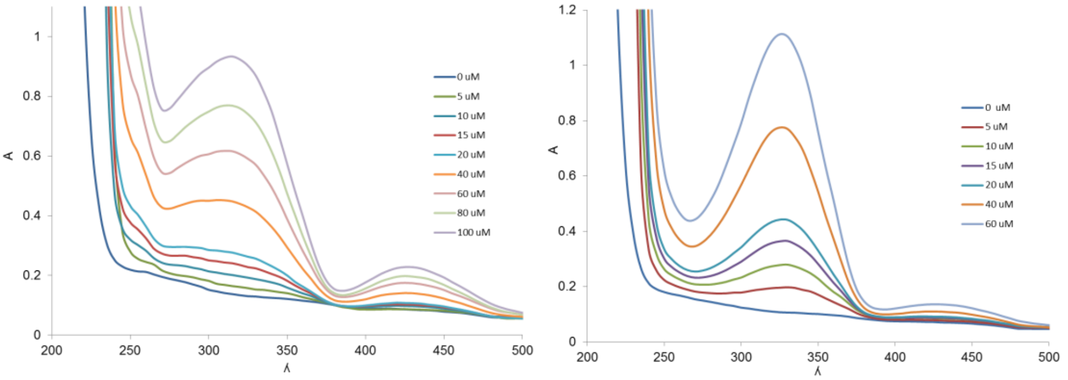

Figure S5. UV spectra of increasing amount of A) *cis* **1** B) *trans* **1**, [Au NP **5**•Zn^{2+}]= 20 Mm

4.4.8. Catalysis

The inhibition of Au NP **5**•Zn^{2+} catalytic activity induced by *cis* and *trans* **1** was studied measuring by UV-Vis the release of PNP at 405 nm. The kinetic was carried out at fixed amount of substrate [HPNPP] = 1mM and at increasing amount of **1** ([**1**] = from 0 to 200 µM), at 37°C. Then, the A/t was plotted as a function of [**1**], obtaining a complete inhibition of the system at 100 µM.

The catalysis at lower concentration of HPNPP (100 µM) were monitored by UHPLC at 318 nm. A stock solution of 3.5 mL solution containing [Au NP **5**•Zn^{2+}] = 20 µM and [HEPES] = 10 mM at pH = 7 was prepared. Then, this solution was divided in two aliquots of 962 µL each and added to a two different UPLC vials. Next, *cis* and *trans* isomers (28 µL from a 718 µM stock solution [**1**] = 20 µM) were added respectively to each of the two vials. 10 µL of HPNPP (10 mM stock solution, [HPNPP] = 100 µM) were added to each vial immediately before injecting in the UPLC.

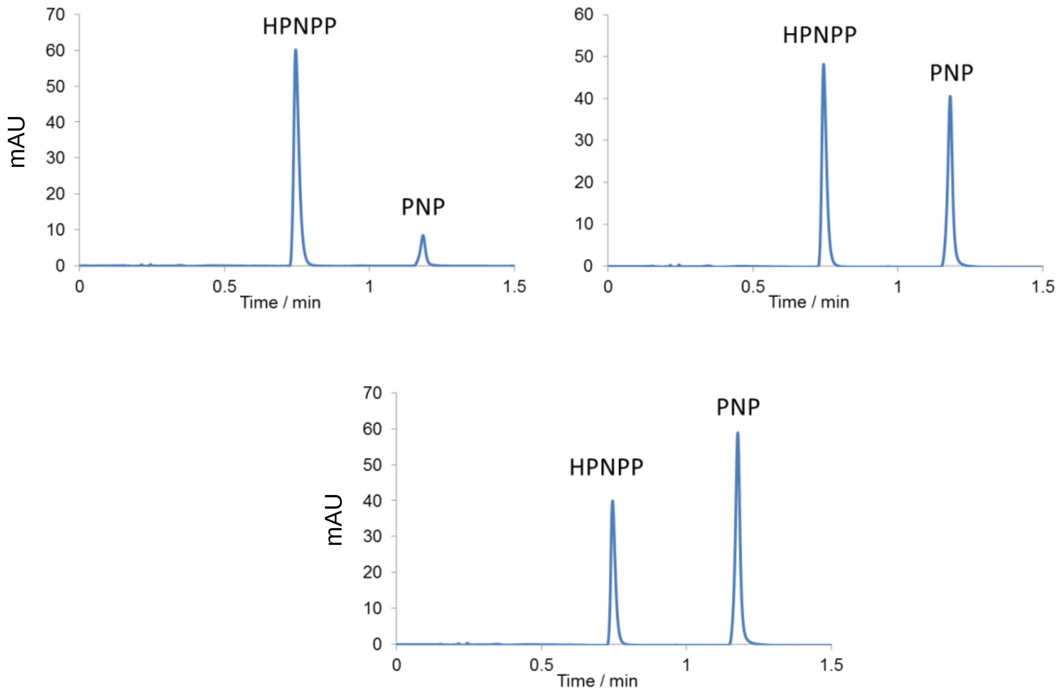

Figure S5. Representative chromatograms of the catalysis of HPNPP in the presence of *trans* **1** (20µM) A) at 0 min, B) at 833, C) at 1665 min [Au NP **5**•Zn^{2+}]= 20 µM Conditions: 5-95 %B in 3 min, 0.8 mL/min; A: H_2O+0.1% HCOOH, B: ACN+0.1% HCOOH measured at 318 nm

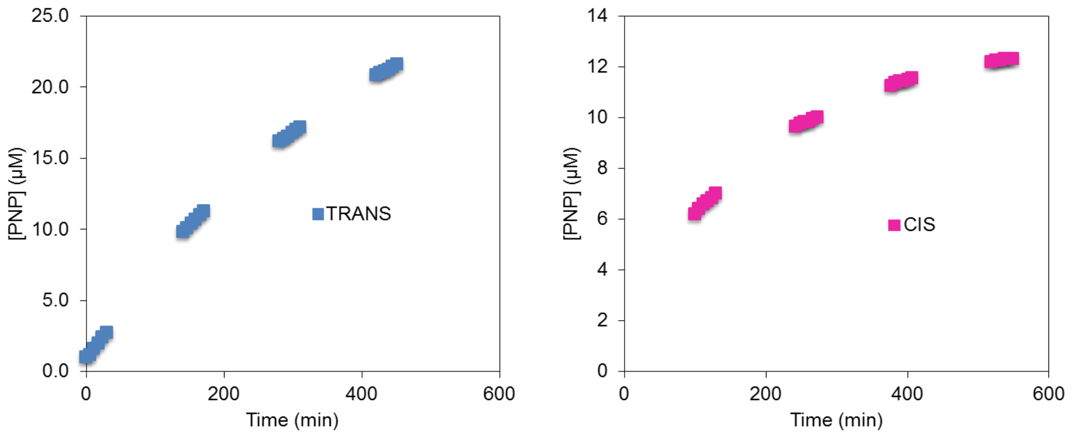

Figure S5. Kinetic profiles of two blanks [Au NP **5**•Zn^{2+}]= 20 µM Conditions: 5-95 %B in 3 min, 0.8 mL/min; A: H_2O+0.1% HCOOH, B: ACN+0.1% HCOOH measured at 318 nm

4.4.9. ON/OFF catalysis induced by light

A stock solution of 3.5 mL solution containing [Au NP **5**•Zn^{2+}] = 20 µM and [HEPES] = 10 mM at pH = 7 was prepared. Then, this solution was divided in three aliquots of 962 µL each and added to a three different UPLC vials. The first vial was used for the switching experiment (switching kinetic) and the other two as controls of *trans* and *cis* isomers. Thus, *trans* isomer (28 µL from a 718 µM stock solution) was added to the first vial and was left to stabilize for 15 min. Then, 10 µL of HPNPP (10 mM stock solution) was added immediately before injecting in the UPLC. The PNP release was measured for 30 min at 318 nm (sample measured every 6 minutes). Afterwards, the sample was irradiated at 365 nm for 60 min to achieve the *cis* isomer and measured for 30 min. Next, it was irradiated at 465 nm to switch to *trans* and measured for other 30 min. The cycle was repeated one more time. The samples were sonicated after each switching in the attempt to favor the release of possibly entrapped azobenzenes in the monolayer.

The two blanks consisted of performing the same HPNPP kinetics but without the switching step, starting with either *trans* or *cis* isomer. Thus, *trans* isomer (28 µL from a 718 µM stock solution) was added to the second vial and it was waited for 15 min until stabilization. Afterwards, the PNP release was measured for 30 min at 318 nm. Then, the solution was irradiated (465 nm, 10 min) and measured (30 min) again. This was repeated 3 times, following the timings of the experiment. The same was done for *cis* isomer but irradiating at 365 nm for 50 min every 70 min to guarantee the presence of *cis* **1**. Notice that at this experiments the irradiation step did not promote any switch; it was done with the unique scope to precisely reproduce the timing of irradiation of the switching kinetic. Finally, the slopes obtained from the switching experiments were normalized dividing the slope for the slopes resulting from corresponding blanks curves. The two blanks consisted of performing the same HPNPP kinetics but without the switching steps, starting with either *trans* or *cis* isomer. The values are reported in Figure 4.22.

4.5. BIBLIOGRAPHY

1. Kiser, P. D., Golczak, M. & Palczewski, K. Chemistry of the Retinoid (Visual) Cycle. *Chem. Rev.* **114,** 194–232 (2014).
2. Schertler, G. F. X. The rhodopsin story continued. *Nature* **453,** 292–293 (2008).
3. Klajn, R., Stoddart, J. F. & Grzybowski, B. A. Nanoparticles functionalised with reversible molecular and supramolecular switches. *Chem. Soc. Rev.* **39,** 2203 (2010).
4. Beharry, A. a & Woolley, G. A. Azobenzene photoswitches for biomolecules. *Chem. Soc. Rev.* **40,** 4422–4437 (2011).
5. Browne, W. R. & Feringa, B. L. Light Switching of Molecules on Surfaces. *Annu. Rev. Phys. Chem.* **60,** 407–428 (2009).
6. Hernandez, R., Tseng, H. R., Wong, J. W., Stoddart, J. F. & Zink, J. I. An Operational Supramolecular Nanovalve. *J. Am. Chem. Soc.* **126,** 3370–3371 (2004).
7. Ipe, B. I., Mahima, S. & Thomas, K. G. Light-induced modulation of self-assembly on spiropyran-capped gold nanoparticles: A potential system for the controlled release of amino acid derivatives. *J. Am. Chem. Soc.* **125,** 7174–7175 (2003).
8. Klajn, R., Bishop, K. J. M. & Grzybowski, B. a. Light-controlled self-assembly of reversible and irreversible nanoparticle suprastructures. *Proc. Natl. Acad. Sci. U. S. A.* **104,** 10305–10309 (2007).
9. Rau, H. Spectroscopic Properties of Organic Azo Compounds. *Angew. Chem. Int. Ed.* **12,** 224–235 (1973).
10. Dias, A. R. *et al.* Enthalpies of formation of cis-azobenzene and trans-azobenzene. *J. Chem. Thermodyn.* **24,** 439–447 (1992).
11. Fliegl, H., Köhn, A., Hättig, C. & Ahlrichs, R. Ab initio calculation of the vibrational and electronic spectra of trans- and cis-azobenzene. *J. Am. Chem. Soc.* **125,** 9821–9827 (2003).
12. Wurthner F., Rebek J. *et al.* Light-Switchable Catalysis in Synthetic Receptors. *Angew. Chem. Int. Ed.* **34,** 446–448 (1995).
13. Hu, J. *et al.* Competitive Photochemical Reactivity in a Self-Assembled Monolayer on a Colloidal Gold Cluster. *J. Am. Chem. Soc.* **123,** 1464–1470 (2001).
14. Klajn, R., Wesson, P. J., Bishop, K. J. M. & Grzybowski, B. A. Writing Self-Erasing Images using Metastable Nanoparticle 'Inks'. *Angew. Chem. Int. Ed.* **48,** 7035–7039 (2009).
15. Klajn, R. *et al.* Bulk synthesis and surface patterning of nanoporous metals and alloys from supraspherical nanoparticle aggregates. *Adv. Funct. Mater.* **18,** 2763–2769 (2008).
16. Klajn, R., Pinchuk, A. O., Schatz, G. C. & Grzybowski, B. A. Synthesis of Heterodimeric Sphere – Prism Nanostructures via. *Angew. Chem.* **46**, 8363–8367 (2007).
17. Kaiser, J. Chemists Mold Metal Objects From Plastic ' Nanoputty '. *Science.* **316,** 187-187 (2007).
18. Pieters, G., Cazzolaro, A., Bonomi, R. & Prins, L. J. Self-assembly and selective exchange of oligoanions on the surface of monolayer protected

Au nanoparticles in water. *Chem. Commun.* **48,** 1916–8 (2012).
19. Manea, F., Houillon, F. B., Pasquato, L. & Scrimin, P. Nanozymes: Gold-nanoparticle-based transphosphorylation catalysts. *Angew. Chem. Int. Ed.* **43,** 6165–6169 (2004).

ABSTRACT

Au NP have emerged as versatile scaffolds for applications in sensing and catalysis due to their unique features such as high stability, biocompatibility, ease of preparation, size- and shape-dependent optical and electronic properties and high surface area to volume ratio. The surface of Au NP can be readily modified with ligands containing functional groups such as thiols, phosphines and amines, which exhibit strong affinity for gold surfaces. The cooperative and collective effects achieved by the organization of organic components on the particle provide all the characteristics of a multivalent surface. Multivalent interactions on the monolayer surface can, hence, be applied to strengthen an interaction between the surface and small molecules. In particular, the self-assembly of small molecules on the multivalent surface of Au NP permits the realization of dynamic complex chemical systems that can be applied in the fields of catalysis, sensing and for the creation of tunable materials.

In the first part of this Thesis, the catalytic abilities of mixed monolayer gold nanoparticles composed of 8-trimethylammonium-octanethiol and different length thiols bearing the 4'-methyl-2,2'-bipyridine•Cu^{2+} complex has been studied. In particular, the influence of the geometry of the mixed monolayer gold nanoparticles on the efficiency and selectivity of the Diels-Alder reaction between cinnamoyl-1-methyl-1*H*-imidazole and cyclopentadiene has been studied. At the same time, the effect of the chiral environment obtained through the self-assembly of chiral peptide (Ac-(LLLL)-Leu-Leu-Gly-Trp-Ser(PO_3H_2)) on the enantioselection was evaluated. The results indicated in one case the formation of additional products. This can be justified considering the steric interactions between the alkyl chains and the catalysts when the catalytic headgroup is level with the monolayer surface. Furthermore, it was demonstrated that the self-assembly of a chiral enviroment on the surface of the Au NP can induce enantioselectivity, although only modestly.

In the second part of the thesis, a modular indicator-displacement-assay is presented. Small molecules with biological relevance are selectively recognized under competitive conditions by using Au NP functionalized with thiols terminating with 1,4,7-triazacyclononane (TACN)•Zn^{2+}. The assay relies on the change in affinity of macrocyclic receptors, such as cavitands, cyclodextrins or calixarenes, for monolayer protected gold nanoparticles upon complexation of the respective target analyte. This change affects the equilibrium between the nanoparticles and a fluorescent reporter molecule leading towards a change in intensity of the fluorescent output signal. The recognition modules can be changed in order to tune the selectivity of the assay without affecting the nature of the output signal. The combined use of recognition modules results in an assay able to detect multiple analytes simultaneously and with high selectivity. A study of the orthogonality of the different receptor-analyte couples led to the demonstration of the possible exploitation of these kinds of arrays within the context of molecular computing.

In the third part, the possibility to self-assemble the molecular switch 4-(phenylazo)benzoic acid on the surface of Au NP functionalized with thiols terminating with 1,4,7-triazacyclononane (TACN)•Zn^{2+} was studied in order to reversibly modulate by light, the affinity of small molecules for the surface. The displacement studies of both probes 343Coumarin-GDDD and 6,8-dihydroxy-1,3-pyrenedisulfonic acid by *cis*/*trans* 4-(phenylazo)benzoic acid revealed that the two isomers have different affinities for the surface.This key point was then exploited to use light for the reversible up- and downregulation of the catalytic activity of the nanoparticle under investigation.

RIASSUNTO

L' importanza delle Au NP come supporto versatile per applicazioni nell'ambito della catalisi e dei sensori nasce dalle loro esclusive caratteristiche come, ad esempio, alta stabilità, biocompatibilità, facilità di preparazione, specifiche proprietà ottiche and elettroniche dipendenti dalla forma e dalle dimensioni e dal loro alto rapporto area/volume. Inoltre, la superficie delle Au NP può essere facilmente funzionalizzata mediante leganti contenenti vari gruppi funzionali, come tioli, fosfine e ammine che presentano alta affinità per la superficie d'oro.
Gli effetti collettivi e cooperativi ottenuti grazie all'organizzazione di componenti organici sulla particella, fornisce multivalenza alla superficie. Le interazioni multivalenti sul monostrato possono, quindi, essere applicate per rafforzare un'interazione tra la superficie funzionalizzata e piccole molecole. In particolare l'auto assemblaggio di piccole molecole su una superficie multivalente permette la realizzazione di sistemi chimici dinamici che possono essere applicati nel campo della catalisi, dei sensori e per la creazione di sistemi regolabili.

Nella prima parte della Tesi, viene studiata la capacità catalitica di nanoparticelle composte da un monostrato misto (in particolare composte da 8-trimetilammonio-octiltiolo e tioli di diversa lunghezza contenenti il complesso metallico 4'-metil-2,2'-bipiridina•Cu^{2+} . In particolare viene studiata l'influenza della geometria indotta dal monostrato misto sulla efficienza e selettività della reazione di Diels-Alder tra cinnamoil-1-metil-1*H*- imidazolo e il ciclopentadiene.
Allo stesso tempo, viene studiato l'effetto dell'ambiente chirale ottenuto grazie all'autoassemblaggio di un peptide chirale (Ac-(LLLL)-Leu-Leu-Gly-Trp-Ser(PO_3H_2)) sulla enantioselettività della reazione.
I risultati dimostrano che in alcuni casi la geometria può influenzare la formazione di prodotti addizionali. Questo può essere giustificato come il risultato di interazioni steriche tra catene alchiliche e catalizzatore, quando quest'ultimo si trova alla pari della superficie del monostrato. Inoltre, è stato dimostrato che, assemblando un peptide chirale sulla superficie delle Au NP, è possibile indurre enantioselettività, sebbene limitata.

Nella seconda parte della Tesi viene presentato un saggio modulare basato sullo spiazzamento di un indicatore. Piccole molecole con rilevanza biologica sono selettivamente riconosciute utilizzando Au NP funzionalizzate con tioli che presentano come gruppo terminale il 1,4,7-triazaciclononano (TACN)•Zn^{2+}. Il saggio si basa sul cambio di affinità di recettori macrociclici come, ad esempio cavitandi, ciclodestrine o calixareni, per le nanoparticelle, dopo avere formato il complesso con la loro rispettiva molecola bersaglio. Questo cambio influenza l'equilibrio tra nanoparticelle e una sonda fluorescente e provoca, di conseguenza, un cambio nel segnale di fluorescenza. I moduli di riconoscimento possono essere cambiati in modo da poter controllare la selettività del saggio senza influenzare la natura del segnale in uscita. L' utilizzo contemporaneo di tre moduli permette di creare un sistema capace di rivelare più analiti simultaneamente e con alta selettività. Lo studio dell'ortogonalità delle differenti coppie recettore/analita permette di dimostrare la possibilità di utilizzo di questo tipo di sistemi nel campo dei computer molecolari.

Nella terza parte viene studiata la possibilità di auto assemblare l'interruttore molecolare acido 4-(fenilazo)benzoico sulla superficie di Au NP funzionalizzate con tioli che presentano come gruppo terminale il 1,4,7-triazaciclononano (TACN)•Zn^{2+}, con lo scopo di modulare con la luce (in modo reversibile) l'affinità di piccole molecole per la superficie. Gli studi di spiazzamento di entrambi i probe cumarina$_{343}$-GDDD e l'acido 6,8-diidrossi-1,3-pirenedisulfonico promosso dal cis/trans acido 4-(fenilazo)benzoico rivelano che i due isomeri hanno diverse affinità per la superficie delle nanoparticelle. Questo punto chiave viene sfruttato per permettere la regolazione tramite luce dell'attività delle nanoparticelle in esame.

ACKNOWLEDGEMENTS

Firstly, I would like to thank my supervisor Prof. Leonard Prins who has provided infinite guidance and support during this PhD period. His constant advices and encouragements motivated me to have a professional attitude towards research.

I am also extremely grateful to my labmates: Davide and France for the musical support, Subo, Jack, Cristian, Flavio, Giovanni, Alvaro, Luca, Agata for the grateful experiences (dinners, parties, languages lessons, films, jokes…) and for a lot of patience. VVB guys!

Very special thanks to Silvia, Paola, Eleonora, Vera, Sara and Ester for being my friends and to make Padova a place that now I can call home.

Finally I want to thank my mother, my grandmother and my spanish family for their emotional support and my father that is my second star to right.

The greatest thank goes to Sergio (and Piero) for sharing the whole day and the whole life with me.